EXAMINING THE COUPLING OF THE MECHANICAL AND CHEMICAL FUNCTIONS OF MYOSIN FAMILY MEMBERS USING SINGLE MOLECULE AND BULK SOLUTION TECHNIQUES

John H. Lewis

A DISSERTATION

in

Cell and Molecular Biology

Presented to the Faculties of the University of Pennsylvania

in

Partial Fulfillment of the Requirements for the

Degree of Doctor of Philosophy

2011

Supervisor of Dissertation

_____

Yale E. Goldman

Professor of Physiology

Co-Supervisor

_____

E. Michael Ostap

Professor of Physiology

Graduate Group Chairperson

_____

Dan Kessler, Associate Professor of Cell and Developmental Biology

Dissertation Committee

Erika L. F. Holzbaur, Professor of Physiology
John W. Weisel, Professor of Cell and Developmental Biology
Paul A. Janmey, Professor of Physiology
Philip Nelson, Professor of Biophysics Theory

EXAMINING THE COUPLING OF THE MECHANICAL AND CHEMICAL FUNCTIONS OF MYOSIN FAMILY MEMBERS USING SINGLE MOLECULE AND BULK SOLUTION TECHNIQUES

John H. Lewis

Acknowledgements

My time as a graduate student at the University of Pennsylvania has far exceeded my expectations, and I am deeply grateful for the opportunity to study here. I particularly want to thank my advisors Drs. Yale E. Goldman and E. Michael Ostap for sharing their vast knowledge and experience so as to guide me to be a better scientist. Between them and their labs I've been exposed to a large number of scientific disciplines such as physics, chemistry, engineering, and of course cell biology. As a result, I am able to better understand the results of my experiments by putting them into a broad, multi-disciplinary context. The members of my thesis committee, Drs. Paul Janmey, Erika Holzbaur, Phil Nelson and John Weisel, have given me much good advice and encouragement over the years that helped me to better navigate the graduate process. I want to thank Dr. Henry Shuman for his inspiration and physical insight. In my first rotation, Dr. Steve Baylor gave me careful and patient instruction in kinetic modeling that has been the foundation for many of my analyses and has helped me a great deal. I also want to thank Dr. Zhe Lu, a professor in the Physiology department, for his unswerving support throughout my scientific career. Finally, I am beholden to Dr. Roderick MacKinnon of Rockefeller University for giving me my start in science as a technician; he was incredibly generous with his time and experience, and the lessons I learned from him and the members of his lab I carry with me to this day.

I have benefited greatly from the high quality and good humor of the members of Yale's and Mike's labs. Joe Laakso is a former graduate student of Mike's and a deft experimentalist, and I learned much from him through our joint interest in myosin Ib.

Talks on physical principles with John Beausang and Serapion Pyrpassopoulos have helped me immeasurably in understanding and analyzing often complicated single-molecule experiments. Yujie Sun, a former post-doc in Yale's lab, helped me with my initial experiments when I was starting in Yale's lab, and was a continual source of good insights.

Members of my family have been the source of a large amount of support and encouragement, in particular my parents Alice Muehlhof and Clifford Lewis as well as my step-parents Robert Muehlhof and Christine Lewis. I also want to thank my brothers, Tom Lewis, Rick Washburn and Jim Washburn and their families. Most of all, I want to thank my wife Hyeon-Gyu (Marianne) Shin for her inspiration and love that has given me strength throughout the graduate student process. I also want to thank Ben Price and Chris Larimore, whose years of friendship and support allowed me to reach this point.

ABSTRACT

EXAMINING THE COUPLING OF THE MECHANICAL AND CHEMICAL FUNCTIONS OF MYOSIN FAMILY MEMBERS USING SINGLE MOLECULE AND BULK SOLUTION TECHNIQUES

John H. Lewis

Supervisors: Dr. Yale E. Goldman and Dr. E. Michael Ostap

Myosins are actin-activated ATPases that convert the chemical energy stored in ATP into the mechanical swing of its lever-arm. The members of the myosin family exhibit a wide range of cellular functions. Myosin Ib (myo1b) is single-headed and may link the cell membrane to the actin network acting as a tension sensor; while myosin V (myoV) is double-headed and can act as a cargo transporter in cells. The very different functions of myo1b and myoV arise from differences in their chemical and mechanical activities. We examined the chemomechanical properties of myo1b using stopped flow and optical trap experiments, from which were determined mechanical step sizes and kinetic rates associated with the chemomechanical steps of the myo1b crossbridge cycle. Most importantly, we found that the rates are slow and the rate associated with ADP release during actin attachment is greatly decreased by force, which could allow it to act as a tension sensor. These kinetic rates and force sensitivity of myo1b are strongly regulated by the signaling molecule, calcium. MyoV steps along actin in a complex and

dense cellular environment; how this is done can be understood from its intrinsic stepping behavior as measured from the changes in lever-arm conformation as it steps along actin using single molecule techniques and a novel analytic tool I developed. From this we find that myoV mainly walks straight along actin, but can take steps around the long axis of actin. The frequency of these azimuthal steps depends on the length of the myoV lever-arm.

Table of Contents

List of Tables

List of Figures

List of Main Equations Used

1 Introduction

1.1 The Myosin Family

Members of the myosin superfamily characterized thus far have been found to be actin-dependent ATPases that utilize the energy of hydrolysis of one ATP molecule per catalytic cycle to generate or maintain force. This force causes the myosin to step unidirectionally along actin where all myosins that have been tested (except myosin VI; **1**) move towards the barbed-end of actin (**2**). Myosin II is the conventional myosin best known for the role it plays in muscle. There are, however, at least 30 other members of the myosin superfamily referred to as unconventional myosins, which are found in most cell types (**2**). These unconventional myosins differ in their structure and in the various roles they play, from cargo transport to mediation of tension (**2**). Elucidating further the mechanisms of the extraordinary variety of functions these myosins can perform is currently the subject of intense research.

Myosin I (myoI) and myosin V (myoV) are unconventional myosins that, in the different roles they are known to play, present themselves as paradigms for the functions of many of the other unconventional myosins. For example, myosin Ic, a type of myosin I, is believed to mediate tension during the adaptation response in the hair cells found in the inner ear (**3**,**4**,**5**,**6**). However, the same myosin has a very different role in the adipocyte, where it is thought to transport vesicles containing GLUT4 (a glucose transporter) to the plasma membrane (**7**). Myosin V has a similar transport role in melanocytes, where it is known to carry melanosomes along the actin network (**8**, **9**).

Understanding how the structures and the underlying kinetic and mechanical activities of different myosins, like myosin I and myosin V, are tuned to function in various cellular processes will inform us of the general principles that govern the functions of all myosin family members.

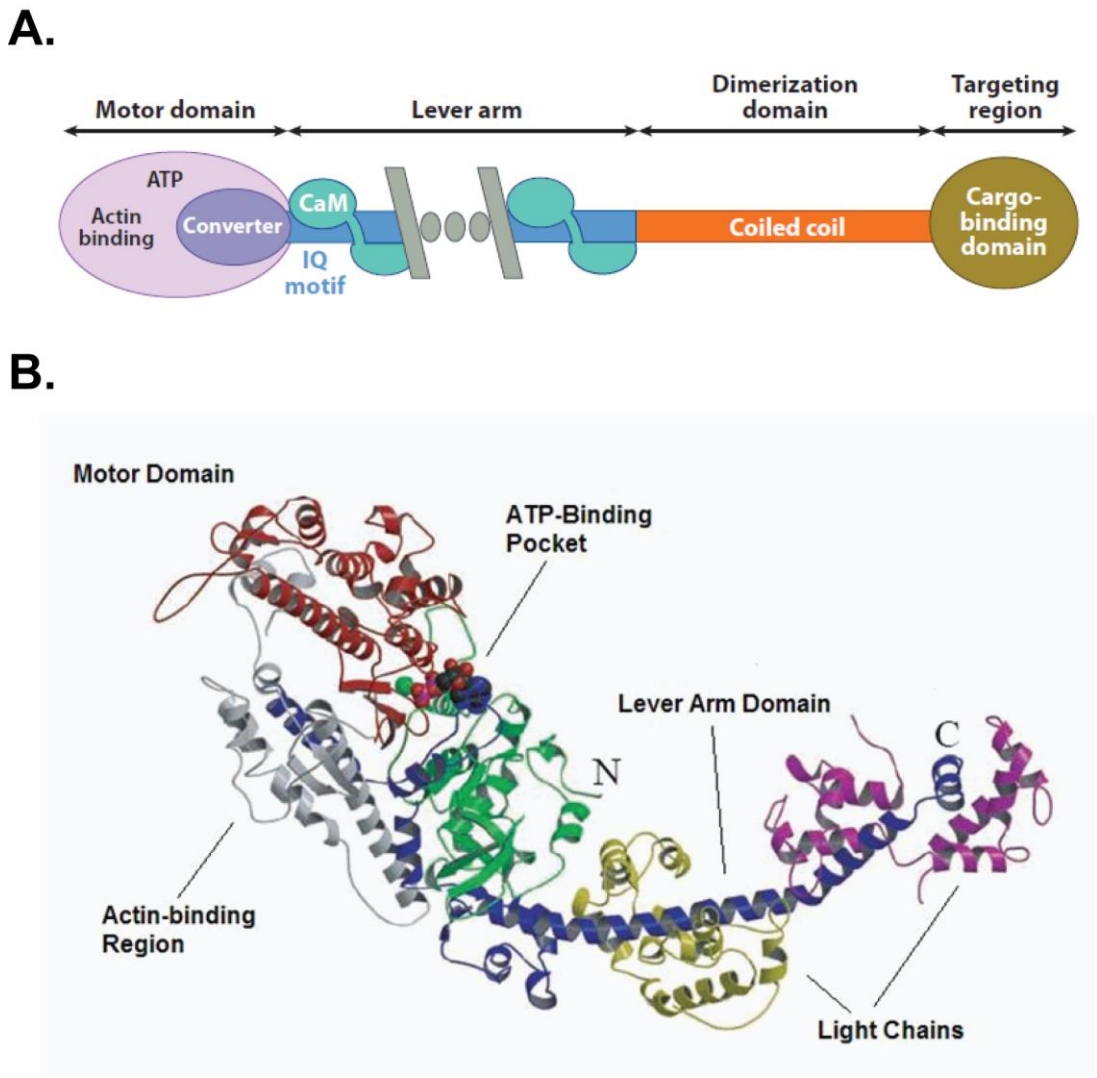

Figure 1.1 –*General myosin structure*

A. Generic domain map for myosin family members. Adapted from (**11**). **B.** Ribbon model of atomic resolution structure of myosin II S1 region, which contains the motor and lever domains with associated light chains. Adapted from (**10**).

1.2 The Crossbridge Cycle and the Structural Basis of Myosin Function

Given the functional diversity of myosin family members, it is remarkable how such a wide range of functions arise from a family that, structurally, is relatively homogenous. The sequences of every myosin family member have a well conserved motor domain to which is attached a lever arm domain, followed by a tail region that can vary greatly depending on the myosin (**Figure 1.1A**; **10**, **11**). The structures of myosin I and myosin V have both been confirmed to possess these general elements. The N-terminal motor domain is the catalytic domain of myosin, with an ATP binding region, where ATP hydrolysis occurs, as well as a region for binding actin. At the C-terminal end of this domain is the lever arm domain, which is a long alpha helix that varies in its length and in the nature of the light chains that bind to it, depending on the type of myosin. The practical length of the lever arm is usually defined by the number of light chain binding motifs, termed IQ motifs, it contains (**10**). After the lever arm is the C-

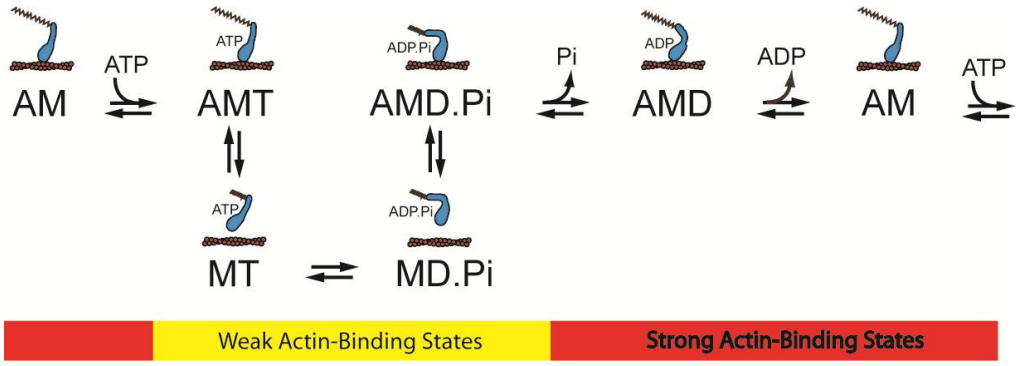

Figure 1.2 – *Myosin crossbridge cycle*

The crossbridge cycle gives a schematic of the global domain motions associated with the different chemical states of myosin.

terminal tail region of myosin, which can possess a variety of cargo binding, and sometimes dimerization, motifs (**10**). One function of this region in some myosin Is is to allow it to bind to negatively charged phospholipids such as PIP2 (**12**), in the plasma membrane (**6**).

The conformation of the structure of a myosin family member changes as it progresses through the steps of ATP hydrolysis in a process referred to as the crossbridge, or ATPase, cycle, as described by Lymn and Taylor (**Figure 1.2**) (**13**). The conformations of the motor and lever arm domains are most affected, where the lever arm changes by rotating about a fulcrum believed to be located in the motor domain (**14**, **15**). In its present form, the primary cycle begins with the myosin strongly attached to actin in a nucleotide free state called the rigor state (**Figure 1.2**). Upon binding ATP, the myosin enters a weakly bound state, where it is either unbound or loosely associated with the actin. Once dissociated, the lever arm undergoes a large swing relative to the motor domain (~60° in myosin II) and the ATP is hydrolyzed; myosin is now in its pre-power stroke conformation, with ADP and inorganic phosphate (P_i) bound. Myosin then weakly binds to actin, releases the inorganic phosphate (P_i) and undergoes its power stroke.

1.3 The Power Stroke of Myosin (The Swinging Lever-arm Hypothesis)

The power stroke has been found to occur in one or two phases, depending on the myosin family member, and leads to net movement. In myosins with a two phase power stroke, the first phase of displacement is thought to be coupled to the release of phosphate

(**Figure 1.2**). The second phase is believed to be coupled to ADP release. In this phase, myo1c is in the rigor state and is able to bind ATP again in order to repeat the cycle. The rate constants associated with each of these steps in the cycle can be very different depending on the myosin type and are important in determining the lifetimes for the weak and strong binding states (**16**).

The power stroke is believed to be caused by a conformational change of the lever-arm domain relative to the motor domain, a concept known as the swinging lever arm hypothesis (**17**). The degree to which the lever-arm swing and the length of the lever-arm itself are the major determinants for the amount of movement a myosin can undergo during the power stroke. In the cell, it is not unusual for the lever-arm to be under load during the power stroke (as caused by dimerization, cargo binding, being part of a filament, or any combination of these). It is therefore not surprising that the mechanics of the power stroke of various myosin types have been found to be load-sensitive, including myosin I and myosin V (**18**,**19**). It was recently shown through single molecule studies that load affects myosin I and myosin V by affecting their attachment lifetimes (**18**,**19**), where this lifetime is increased or decreased depending on the directionality and magnitude of the applied force.

1.4 Thesis Objective

Myosin Is are expressed in all cell types and have been implicated in a number of cellular processes including membrane retraction, macropinocytosis, phagocytosis, membrane trafficking, cell-cell adhesion, and mechanical signal transduction

(**20**,**21**,**4**,**22**,**23**,**24**,**25**). The proposed mechanism that could link these diverse functions together is that myosin Is act to cross-link actin with the cellular membrane. Biochemical studies have shown that some myosin Is have an exceptionally long strong actin binding lifetime (although it still makes up a small fraction of the very long ATPase cycle time, see **16**). This long strong actin-binding lifetime is consistent with myosin I acting as a tether between actin and the membrane. Load sensitivities as have been seen with myosin Ib from our group (**19**, **26**) and myosin Ic (**5**) suggest that myosin I acts a tension sensor in its linkage between the actin network and the cellular membrane.

Before a more detailed mechanism for its action in the cell can be determined, there are many basic questions about myosin I that need to be addressed: (1) Basic biochemical parameters of the myosin I ATPase cycle have never been measured at physiological temperatures (37 °C). Are these parameters significantly different from those measured at room temperature, and does the temperature dependence of these parameters somehow distinguish myosin I from other myosins? (2) There have been previous speculations about the force sensitivity of myosin I, but to what degree and to which step in the cross-bridge cycle does it correspond? (3) Do any of myosin I's structural elements, such as its lever arm, regulate this force sensitivity? (4) Do cellular environmental elements such as calcium regulate the chemomechanical activity of myosin I? How fast does calcium affect this regulation? What structural element on the is the target of calcium regulation? How does calcium affect the coupling of the chemical and mechanical activities of myosin I? These questions are addressed using single molecule and ensemble level techniques exploring the chemomechanical activity of myosin I.

Myosin V is a dimer whose best known cellular role is that of a cargo transporter that can take multiple steps along actin. In this role, it is required to travel through a cytoplasm that is densely packed (**27**). Understanding how myosin V can navigate such a complex environment first requires an understanding of the basic myosin V stepping mechanism in a simpler, cell-free environment. Numerous studies have been done examining basic myosin V stepping behavior, looking at characteristic parameters such as average step-size and run-lengths (**28**,**29**,**30**,**31**). A hand-over-hand stepping mechanism is now largely accepted based on sophisticated fluorescence studies done on processively stepping myosin V (**32**,**33**). More complicated behavior has been described for the overall stepping path, such as myosin V mediated actin twirling and myosin V stepping with a left-handed pitch on actin (**34**,**35**).

A more detailed mechanism for myosin V stepping requires a number of questions to be answered: (1) Many of the more sophisticated studies are reporting motion of the probe attached to the lever arm of myosin V, which leaves some ambiguity as to the nature of the myosin V stepping. How does the orientation of the probe relate to the orientation of the lever arm? (2) How does the orientation of the lever arm of myosin V change with each step it takes along actin? This will give detailed information of potential steps a myosin V can take and allow models to be created that describe possible paths along actin. These questions are addressed using single molecule techniques exploring the stepping behavior of myosin V.

1.5 Thesis Overview

In the research leading to this thesis, a number of experiments were performed at the ensemble and single molecule levels in order to probe the chemomechanical functions of two unconventional myosins, myosin I and myosin V. The goals of the myosin I studies, presented in Chapter 2, are to (1) characterize key rates in the ATPase cycle and determine their possible temperature dependence; (2) determine which of these chemical steps correspond to the mechanical power stroke, and which of these, if any, are sensitive to force and to what extent; (3) examine how the length of the lever-arm determines the step-size and magnitude of its force sensing ability; (4) examine how calcium regulation impacts the key steps in the ATPase cycle, the step-size and force sensitivity. The goals of the myosin V studies, presented in Chapter 3, were to (1) examine how lever-arm length might determine the three-dimensional path of myosin V on actin; (2) determine the local orientation of probes labeling myosin V's lever arm to allow for transformation of the probe orientation that was measured in experiments to the more functionally relevant lever-arm orientation. Chapters 2 and 3 are each organized with an Introduction, a Methods section, a Results section and a Discussion section. A global discussion of both projects is offered in Chapter 4.

Chapter 5 is the appendix, detailing principles and derivations of the numerous equations used in this thesis. Section 5.1 discusses the General Simplex Fit program I developed and used in Chapter 2. It also describes the basic principles behind the algorithms used in this program. Section 5.2 describes the kinetic modeling used in the force-dependence studies. Section 5.3 describes the kinetic modeling used for the calcium regulation studies. Section 5.4 gives the derivations of the equations used in Chapter 3 as

well as a full discussion of the analysis that uses these equations to transform the probe orientation to the lever orientation.

In chapter two, the sections detailing the mechanical activity of myosin Ib, were done in collaboration with Joseph Laakso, a former graduate student of Mike Ostap's. He performed the optical trap experiments and did the analysis involving event selection, while I performed the various analyses on the distributions of the selected events.

2 Characterization and Regulation of the Chemomechanical Activity of Myosin Ib

Author Contributions

The myo1b temperature dependence study appeared in reference (**36**). John Lewis and Michael Ostap designed research; John Lewis, David Hokanson and Michael Ostap performed research; John Lewis, David Hokanson, Henry Tianming Lin and Michael Ostap contributed new reagents/analytic tools; John Lewis, David Hokanson and Michael Ostap analyzed data; John Lewis, David Hokanson and Michael Ostap wrote the paper.

The myo1b force dependence study appeared in references (**19**, **26**). Joe Laakso, Henry Shuman and Michael Ostap designed research; Joe Laakso and Michael Ostap performed research; Joe Laakso, John Lewis, Henry Shuman and Michael Ostap contributed new reagents/analytic tools; Joe Laakso, John Lewis, Henry Shuman and Michael Ostap analyzed data; Joe Laakso, John Lewis, Henry Shuman and Michael Ostap wrote the paper.

The calcium regulation of the myosin Ib tension sensing section will be submitted to Nature Structural and Molecular Biology. John Lewis, Joe Laakso, Henry Shuman and Michael Ostap designed research; John Lewis, Joe Laakso and Michael Ostap performed research; John Lewis, Joe Laakso, Henry Shuman and Michael Ostap contributed new reagents/analytic tools; John Lewis, Joe Laakso, Henry Shuman and Michael Ostap analyzed data; John Lewis, Joe Laakso, Henry Shuman and Michael Ostap wrote the paper.

2.1 Introduction

2.1.1 Temperature dependence of nucleotide association and kinetic characterization of myo1b

Myosins are molecular motors that use the energy stored in ATP to perform mechanical work along actin filaments. Myosin-Is are the single-headed, low-molecular-weight members of the myosin superfamily that are proposed to link cellular membranes with the actin cytoskeleton. Myosin-I isoforms bind phosphoinositides directly (**12**) and function in several important cellular processes, including membrane retraction, macropinocytosis, phagocytosis, membrane trafficking, cell-cell adhesion, and mechanical signal transduction (**20**,**21**,**4**,**22**,**23**,**24**,**25**).

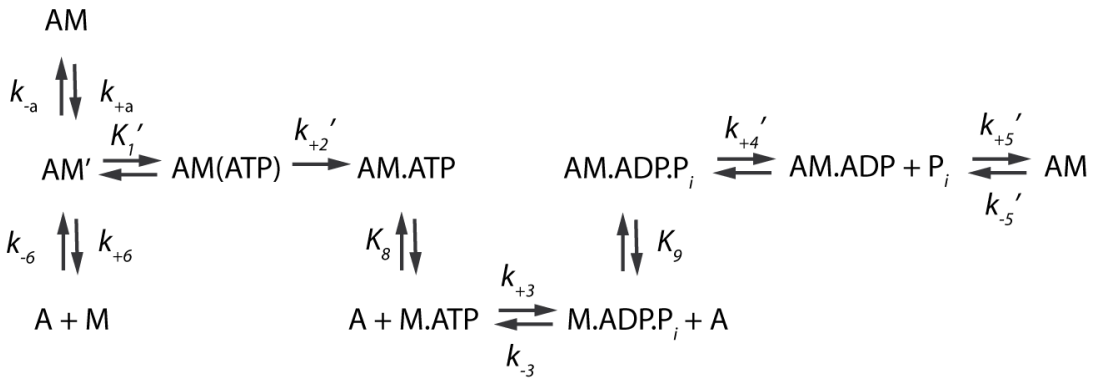

Scheme 1

The biochemical mechanisms of long-tail and short-tail myosin-I isoforms have been studied (**36**, **37**, **38**, **39**), with myo1b being the best characterized short-tail isoform (**40**, **41**, **42**). The myo1b ATPase mechanism (**Scheme 1**) is notable in that (a) the maximum rate of ATP binding and population of the myo1b^{IQ} weakly-bound states is >

30-fold slower than myosin-II, (b) nucleotide-free myo1b is in equilibrium between a state that binds nucleotide (AM') and a state that does not bind nucleotide (AM), (c) the rate of transition between AM and AM' ($k_{+\alpha}$) states is similar to the rate of ADP release (k_{+5}'), and (d) ADP release is slow and is accompanied by a rotation of the lever arm.

We proposed that the strikingly slow actomyo1b ATPase rate constants are a property of all short-tail myosin-I isoforms (**38**,**16**). However, it has been shown recently that short-tailed *Dictyostelium* myosin-IE (not to be confused with vertebrate long-tail myo1e (**38**)) has kinetic rate constants that are substantially faster than vertebrate short-tail isoforms (**39**). Because of experimental convenience, nearly all kinetic characterizations of myosin ATPase cycles have been performed at temperatures between 18 – 25 °C, which is the range in which *Dictyostelium* cells live. There is no complete kinetic characterization of any vertebrate unconventional myosin at physiological temperature (37 °C), and it is possible that myosin-I rate constants are highly temperature sensitive. Therefore, it is important to determine the kinetic lifetimes of the myo1b intermediates at physiological temperature. To that end, we performed experiments that determined the rate constants that define the rat myo1b ATPase cycle at 37 °C, and we provide the first measurement of the rates of ATP hydrolysis and phosphate release for myo1b. Our characterization has allowed us to calculate the myo1b duty ratio at physiological temperature and determine thermodynamic parameters of ATP binding and ADP release.

2.1.2 Myosin I can act as a molecular force sensor

ATP-dependent conformational changes in the myosin motor domain are amplified into a power-stroke by the light chain binding domain (LCBD) which acts as the motor's lever arm and is also referred to as the regulatory domain. The power stroke of myosin occurs during the strong actin-binding phase of its ATPase cycle, and has been shown to occur in two steps for some myosins, including myosin I (**43**). The rate of ADP release is the rate limiting step for exiting the strong actin-binding state, leading to the proposal that this step is sensitive to force (**44**). This was first shown to be the case for a myosin family member with myosin II and brush border myosin I, where it was found that the second step of the power stroke was associated with ADP release and was force sensitive (**43**). Moreover structural studies have shown that the second step of the myosin I power stroke is associated with a 32° rotation in its LCBD (**45**).

To test the proposal that myo1b is a tension sensor, a series of experiments were performed on myo1b to characterize its mechanical activity, including any potential force sensitivity. Optical trap experiments performed on individual myo1bs characterized the size of its overall power stroke and identified its component substeps with steps in the ATPase cycle. Experiments in the optical trap coupled with a force feedback system (**46**) were performed on myo1b in order to test the effect of isometrically applied force on the lifetime of actin attachment for myo1b. These studies clearly demonstrate that the second sub-step of myo1b is associated with ADP release and is highly force sensitive, causing lifetimes of actin attachment to increase to >75-fold in the presence of forces < 2 pN.

2.1.3 Dependence of effective lever-arm length on the mechanical activity of isoforms of myosin Ib

We show in this thesis that the lifetime of actin attachment of the motor domain of myo1b is increased by force applied along its LCBD (see Section 2.3.2; **19**). The LCBD of most myosins is composed of one or more IQ motifs, which are α-helical sequences of ~ 23 amino acids each with a core consensus sequence that binds calmodulin and calmodulin-like proteins at low calcium concentrations. Calmodulins bound to the LCBD are thought to increase its stiffness, thus allowing it to bear load and act as a mechanical lever arm (**47**). The amount of mechanical work performed by the LCBD is related to the step-size, which in other myosins has been shown to be linearly related to the length of their respective LCBDs (**48**,**49**).

Myosin Ib has three native splice isoforms myo1b^{a}, myo1b^{b}, and myo1b^{c} that result in different length LCBDs with 6, 5 and 4 IQ motifs, respectively (**Figure 2.1; 20**,**50**). Single molecule optical trap experiments were therefore performed on isoforms of myo1b to test the dependence of the lengths of their LCBDs on their respective step-sizes. Because of the importance of the LCBD length on the amount of mechanical work that myosin can perform, the dependence of the LCBD length on myo1b force sensing was tested as well in optical trap experiments coupled with force feedback.

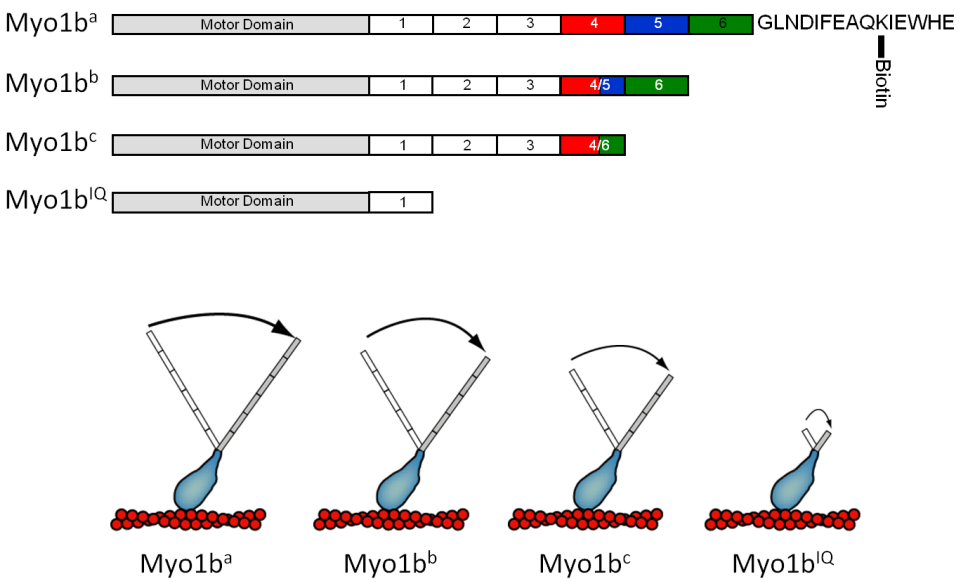

Figure 2.1 – *Myosin Ib (myo1b) isoforms used in this study*

Myo1b has three native splice isoforms, myo1b[a], myo1b[b] and myo1b[c] with 6, 5 and 4 calmodulin-binding IQ motifs in their light chain binding domains (LCBD)

2.1.4 Calcium regulation of the chemomechanical activity of myosin Ib

It has long been recognized that calcium binding to LCBD-associated calmodulins is a potential cellular mechanism for regulating motility (**51**, **52**, **53**), especially since it was realized that calmodulin binding likely provides mechanical stiffness to the LCBD (**47**). Indeed, it has been demonstrated *in vitro* that calcium binding weakens the affinity of calmodulin for the LCBD of some myosins resulting in the uncoupling of motile and ATPase activities (**53**). Additionally, it has been shown that processive stepping of myosin-V is decreased when the free calcium concentration is increased, presumably as a result of calcium-induced changes in LCBD mechanics (**54**).

We show in this thesis that the actin-attachment kinetics of the widely expressed myosin-I isoform, myo1b, to be highly force sensitive (see Section 2.3.2; **19**), with this force sensitivity depending on LCBD length (see Section 0; **26**). Isoforms with longer LCBDs are more force sensitive. The extraordinarily long attachment lifetime of myo1b under load poses a regulatory challenge. How are force-induced attachments that last ~100 s terminated? Calcium binding to LCBD-associated calmodulins is a likely candidate, since calcium binding to one or more of the calmodulins bound to the lever arm could directly lead to a reduction in its stiffness or effective lever arm length. This change in LCBD mechanics could reduce the ability of the lever arm to bear load, and potentially release the myo1b from a prolonged, force-induced actin binding event.

In this study, we examined the effect of calcium on the kinetic and mechanical function of myo1b through a series of ensemble-level and single molecule experiments. Experiments were performed with the "a" splice isoform of myo1b truncated after the sixth IQ motif (myo1b^{a}) or the IQ-motif closest to the motor domain (myo1b^{IQ}) (**Figure 2.1**). The results of these experiments establish that calcium decreases the unitary displacement if myo1b and substantially decreases its force sensitivity.

2.2 MATERIALS AND METHODS

2.2.1 Reagents, Proteins, and Buffers

2'-Deoxy-methyanthraniloyl-labeled ATP (mantATP) was synthesized as described (**55**). ADP and ATP concentrations were determined spectrophotometrically before each experiment by absorbance at 259 nm, ε_{259} = 15,400 $M^{-1}cm^{-1}$. MantATP concentrations were determined by absorbance at 255 nm, ε_{255} = 23,300 $M^{-1}cm^{-1}$ (**55**).

Rabbit skeletal muscle actin was prepared and gel filtered (**56**). Actin concentrations were determined by absorbance at 290 nm, ε_{290} = 26,600 $M^{-1}cm^{-1}$. Actin for transient kinetics experiments was labeled with pyrenyl iodoacetamide (pyrene-actin) and gel filtered (**57**). All actin was stabilized with a molar equivalent of phalloidin (Sigma). Calmodulin (CaM) was expressed in bacteria and purified as described (**58**).

Steady-state and transient experiments were performed in KMg25 buffer (10 mM Mops, 25 mM KCl, 1 mM $MgCl_2$, 1 mM EGTA, 1 mM DTT). The pH of the buffer was adjusted to pH 7.0 at 25 °C, and changed by less than 0.1 pH units when the temperature was increased to 37 °C. Free CaM (1 μM) was included in all solutions that contain myo1b^{IQ} (**50**). Free calcium concentrations used in the calcium binding experiments were estimated using the MaxChelator program.

2.2.2 Myosin-I Expression and Purification

Myo1b expression constructs were prepared as described (**50**). All myo1b splice isoform constructs were truncated after the final IQ motif in the light chain binding domain (**Figure 2.1**). An additional non-native construct (myo1b^{IQ}) consisting of the motor and first IQ motif was also prepared. The concentration of myo1b^{IQ} was determined using the Coomassie Plus reagent (Pierce) using bovine serum albumin (BSA) as a standard. Based on previous work that validates myosin active-site concentrations (**36**, **37**, **59**, **60**), BSA is an appropriate protein standard. Final stock concentrations were typically 5 – 10 mg/ml, and were stored at -20 °C in 50% glycerol. Preparations of four liter cultures yielded 4 – 15 mg of protein. A 15-amino acid AviTag sequence for site-specific biotinylation and a FLAG sequence for purification were inserted at the C-termini of the four constructs (**50**, **61**).

Myo1b constructs were expressed and purified from Sf9 cells that were co-infected with virus containing recombinant myo1b and calmodulin as described (**38**). Concentrated protein was site-specifically biotinylated with 20 µg/ml biotin ligase in the presence of 10 mM MgATP and 50 µM biotin at 30 °C for 1 h. Free biotin and ATP were removed by MonoQ column chromatography and dialysis. Protein integrity was assessed by a standard motility assay (**50**, **62**). The same protein preparations were used to acquire step sizes and distance parameters, thus the lower myo1b^{b} step size is not the results of inadvertent switching of isoforms.

2.2.3 Kinetic Measurements

Transient kinetic measurements were made with an Applied Photophysics (Surrey, U.K.) SX.18MV stopped-flow. A 400 nm long-pass filter (Oriel) was used to monitor pyrene (λ_{ex} = 365 nm) and mantATP (λ_{ex} = 295 nm) fluorescence. Tryptophan fluorescence was monitored using a 320 nm band pass filter with an excitation wavelength of 295 nm. The time courses in the figures show the average of 1 - 4 individual traces. Transients were fitted to exponential functions using the software supplied with the stopped-flow. Unless stated otherwise, all concentrations are given as final after mixing. Steady state actin activated ATPase and actin motility (gliding assays) rates were measured in experiments performed as described before (**50**).

Solutions of actomyo1b contained apyrase (0.01 U/mL) when loaded into the stopped flow to ensure the mixtures were free of contaminating ADP and ATP. This apyrase concentration was high enough to remove contaminating nucleotide, but not high enough to interfere with the kinetic measurements. Solutions used for determining the rate of association of myo1b^{IQ} with pyrene-actin included 0.3 U/mL apyrase.

Transient phosphate (P_i) release was measured by stopped-flow using the coupled assay system containing the fluorescently labeled mutant of the phosphate binding protein (P_iBP) using an excitation wavelength of 425 nm and a 440 nm long-pass filter (**63**,**64**). To remove contaminating phosphate, the instrument lines were incubated with 1 mM 7-methylguanosine and 0.2 U/mL nucleoside phosphorylase overnight. Stopped-flow solutions contained 100 µM 7-methylguanosine and 0.004 U/mL nucleoside phosphorylase. Measurements were made in sequential mixing mode at 37 °C. Myo1b^{IQ}

(10 μM) was mixed with 5 μM ATP in the first mix and aged for 7 s, resulting in concentrations of 5 μM myo1b^{IQ} and 2.5 μM ATP. Myo1b^{IQ} and ATP were then mixed with actin, resulting in final concentrations of 2.5 μM myo1b^{IQ}, 1.25 μM ATP, and 0 – 80 μM actin. P_iBP was included in all solutions, and was present at a final concentration of 5 μM after mixing. Errors reported are standard errors in the fits.

Kinetic modeling was performed using the reaction outlined in Scheme 1 where A is actin and M is myosin. The temperature dependence of the rates of ATP binding and ADP release were analyzed according to the Arrhenius relation:

$$\ln(k) = \ln(A) - \frac{E_a}{RT}$$

2.2.1 – Arrhenius Equation

where R is the gas constant (8.31451 J·mol^{-1}K^{-1}), T is the temperature in Kelvin, E_a is the activation energy, and A is the pre-exponential factor (see Section 5.4.1). The standard enthalpy change of the isomerization of the AM to AM' states (K_α) was determined from a van't Hoff plot:

$$\ln(K_\alpha) = \frac{-\Delta H^\circ}{RT} + \frac{\Delta S^\circ}{R}$$

2.2.2 - van't Hoff Equation

ΔH° is the enthalpy and ΔS° is the entropy.

2.2.4 Bead and Motility Chamber Preparation

NEM-myosin II was prepared according to the method of Veigel et al. (**65**) and stored in 50% glycerol for up to one month at -20°C. 2 μL of polystyrene beads (1.1 μm diameter, 10% by volume) were washed twice in 250 μL water to remove surfactant in storage solution. The beads were re-suspended in ~15 μL dH_2O by brief sonication in a bath sonicator and ~80 μL (2.5 mg/mL) of the NEM-myosin-II stock solution was added to the beads and incubated for two hours at 4°C. The coated beads were added to 1 mg/ml BSA in high salt buffer (500 mM KCl, 4 mM $MgCl_2$, 1 mM EGTA, 20 mM KH_2PO_4, pH 7.2) and mixed gently to depolymerize long myosin filaments on the beads. The beads were collected by low speed centrifugation (7 minutes @ 8000 rpm on a desktop centrifuge) and re-suspended in 1 mg/ml BSA in motility buffer. The beads were collected by another round of low speed centrifugation and re-suspended in ~200 μL motility buffer. Coated beads were stored at 4°C and used for up to 10 days.

Nitrocellulose-coated motility chambers containing 1.9 μm silica beads as pedestals (Bangs Laboratories, Fishers, IN) were prepared as described (**46**,**19**). Solutions were added sequentially to the chamber as follows: 0.1 mg/mL streptavidin in water (3 min); 1 mg/mL bovine serum albumin in KMg25 (10 mM Mops, 25 mM KCl, 1 mM $MgCl_2$, 1 mM EGTA, 1 mM DTT) (2 x 5 min); 1 – 5 nM biotinylated myo1b in KMg25 + 10 μM calmodulin (5 min); 1 nM rhodamine-phalloidin labeled F-actin in KMg25 with 10 mg/ml glucose, 1 - 50 μM ATP, 20 μM calmodulin, 192 U/ml glucose oxidase, and 48 μg/mL catalase (Roche). Beads coated with NEM-myosin-II were added to one side of the chamber to replace ~¼ the volume of the chamber. The chamber was sealed with silicon vacuum grease (Dow Corning, Midland, MI).

2.2.5 Single Molecule Measurements

Single-molecule interactions were recorded using the three-bead assay geometry in a dual-beam optical trap system as described (**19**,**46**). Trap stiffnesses were ~0.022 pN/nm. NEM-myosin-II beads were captured in separate optical traps, and bead-actin-bead dumbbells were assembled by contacting the trapped beads with single actin filaments. Bead-actin-bead assemblies were pre-tensioned to ~2.5 pN and lowered onto the surface of a pedestal using a piezoelectric stage controller to scan for actomyo1b interactions. Upon observation of interactions, data were digitized with a 2 kHz sampling rate for 6 - 10 minute intervals. All experiments were performed in KMg25 (10 mM Mops, 25 mM KCl, 1 mM $MgCl_2$, 1 mM EGTA, 1 mM DTT).

The force-dependence of actomyo1b attachment lifetimes was measured using a feedback system that applies a dynamic load to the actomyo1b to keep the actin filament near its isometric position during the myosin working stroke as described (**19**,**46**). Briefly, changes in the force on the bead attached to the pointed end of the actin filament (transducer bead) were fed through an analog integrating feedback amplifier to an acousto-optic deflector, which changed the position of the laser trap on the bead bound to the barbed end of the actin filament (motor trap) until the position of the transducer bead was restored to its original position. The response time of the feedback loop in the absence of interactions was adjusted to 50 ms for each bead-actin-bead assembly.

To control low-frequency stage position fluctuations, an additional infrared laser beam (λ = 830 nm, Point-Source) was installed on the same beam path as the trapping laser, with the exception that after being collected and collimated by the condenser

objective, the laser light was directed to a separate 4-quadrant photodiode. We monitored the position of the pedestal on which the myo1b is attached, and controlled the *x*-axis (i.e., the long axis of the actin filament) of the stage position using an analog integrating feedback amplifier. By incorporating this stage feedback system into our experiments, we can reduce fluctuations of the stage due to drift or mechanical vibration, thus reducing the noise in our force traces.

2.2.6 Event Selections

To determine the start and endpoints of actomyo1b attachments, we used the covariance threshold selection method #2, as described (**19**). The variance of the digitized forces on both the transducer and motor beads was calculated at each time point of the data files over an 85 ms sliding-window and the resulting signal was smoothed over a 50 ms sliding-window. The covariance was then calculated as described (**46**). In this method, the beginning of the attachment is defined as the point where the covariance decreased below a point in which the histogram of covariances over the data set was at a minimum. The ends of the attachments were defined as the point where the covariance went above that same threshold. To reduce false positive events due to transient decreases in covariance during unattached periods, we included only events longer than 100ms (twice the width of our smoothing window). Ensemble averages of interactions that were synchronized at the times the interactions started or ended were performed as described (**43**).

2.2.7 Distributions from Single Molecule Events Fit Using a Maximum Likelihood Routine

The best values for the parameters described in equations 2.3.3 - 2.3.5 were found using a Maximum Likelihood routine utilizing a modified exponential decay probability distribution function (see Section 5.1). The Log Likelihood was minimized with a Nelson-Mead Downhill Simplex routine (see Section 5.1; **66**). The function was sufficiently complex that the minimization had to be frequently restarted in order to find the true global minimum. The restart algorithm was based on a modified Annealing routine sometimes used for multiple parameter fits (see Section 5.1; **66**). The combination of these two algorithms allowed for a rapid convergence to the global minimum of the Log Likelihood function. Confidence intervals for each uniquely determined parameter were found by simulating the data with a Bootstrap routine (see Section 5.1; **66**). We generated a 1000 such data sets and independently fit them for all of the relevant parameters. In order to calculate the confidence interval of 90 % for a given parameter, the boundaries were determined in which 45% of the simulated data were contained on either side of the value of the parameter from the actual data. The maximum and minimum confidence intervals were then calculated from the upper and lower boundaries, respectively.

2.3 RESULTS

2.3.1 Temperature dependence of nucleotide association and kinetic characterization of myo1b

2.3.1.1 Myo1b^{IQ} Binding to Actin Filaments

A ~75% fluorescence quenching upon strong binding of myo1b^{IQ} to pyrene-actin allowed us to monitor the association of myo1b^{IQ} with actin (k_{-6} ; **Scheme 2**). Time courses of myo1b^{IQ} binding to actin at 37 °C follow single exponentials, and the observed rates depend linearly on the actin concentration (**Figure 2.2**). Data were modeled as:

$$A^* + M \underset{k_{-6}}{\overset{k_{+6}}{\rightleftharpoons}} AM'$$

Scheme 2

where A^* represents the unquenched fluorescent state of pyrene-actin. A linear fit to the data yields an apparent second-order rate constant of k_{-6} = 8.2 ± 0.32 $\mu M^{-1}s^{-1}$ (**Table 2.1**). The rate of dissociation of myo1b^{IQ} from pyrene-actin (k_{+6} ; **Scheme 2**) was measured by competition with 50-fold excess of unlabeled actin (**Figure 2.2**). The time course fit a single exponential function with a rate k_{+6} = 0.0044 ± 0.00010 s^{-1} (Table 2.1). The actomyo1b^{IQ} dissociation constant (K_6) calculated from the dissociation and association rates (k_{+6}/k_{-6}) is K_6 = 0.54 ± 0.024 nM (**Table 2.1**).

Actin Binding	
k_{+6} (s^{-1})	0.0044 ± 0.00010[b]
k_{-6} ($\mu M^{-1}s^{-1}$)	8.2 ± 0.32[b]
K_6 (nM)	0.54 ± 0.024[c]

ATP Binding	
$1/K_1$' (μM)	330 ± 25[b]
k_{+2}' (s^{-1})	500 ± 15[b]
K_1'k_{+2}' (μM^{-1} s^{-1})	1.5 ± 0.12[c]
K_1'k_{+2}' (μM^{-1} s^{-1})	1.2 ± 0.041[b,d]
K_1'k_{+2}' (μM^{-1} s^{-1})	0.64 ± 0.020[e]

ATP Hydrolysis	
k_3^{app} (s^{-1})	41 ± 4.9[f]

Phosphate Release	
k_{+4}' (s^{-1})	0.58 ± 0.056[g]
K_9 (μM)	53 ± 9.8[g]

ADP Release	
K_5' (μM)	0.84 ± 0.068[b]
k_{+5}' (s^{-1})	6.7 ± 0.064[b]
k_{-5}' (μM^{-1} s^{-1})	8.0 ± 0.65[c]

Nucleotide-Free Isomerization Step	
K_α	3.7 ± 0.65[b]
$k_{+\alpha}$ (s^{-1})	13 ± 1.0[b]
$k_{-\alpha}$ (s^{-1})	3.5 ± 0.67[c]

[a] KMg25 (10 mM MOPS (pH 7.0), 25 mM KCl, 1 mM EGTA, 1 mM DTT, 1 mM $MgCl_2$, 37 °C) + 1 μM CaM.

[b] Pyrene-actin fluorescence

[c] Calculated

[d] Determined from a linear fit of the data at low ATP concentrations

[e] Light scattering in the presence of mantATP

[f] MantATP

[g] Phosphate-binding protein.

Table 2.1- *Rate and Equilibrium Constants for the Myo1b ATPase Cycle at 37 °C.*

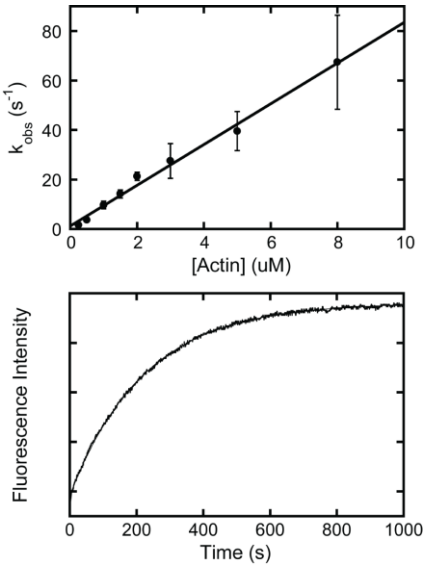

Figure 2.2 - *Kinetics of myo1b^{IQ} association with actin filaments.*

(Top) Actin concentration dependence of the observed rate (k_{obs}) of pyrene-actin binding to myo1b^{IQ} in KMg25 at 37 °C. A 5:1 actin to myo1b^{IQ} ratio was maintained for each actin concentration. The solid line is a linear fit to the data. (Bottom) Time course of pyrene-actin fluorescence increase after mixing 2.0 μM pyrene-actomyo1b^{IQ} with 100 μM unlabeled actin (final concentrations). The smooth line is the best fit of the data to a single exponential rate (k_{obs}= A(1-e$^{-k \cdot t}$)).

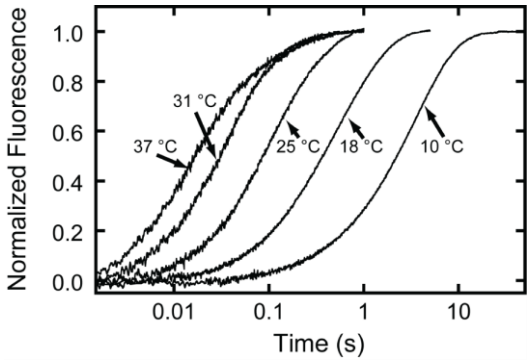

Figure 2.3 - *Temperature dependence of ATP binding to actomyo1b^{IQ}.*

Pyrene-fluorescence transients obtained by mixing 1.0 μM actomyo1b^{IQ} with 60 μM ATP at 10 – 37 °C.

2.3.1.2 ATP-Induced Population of the Weakly-Bound States

Pyrene-actin fluorescence was used to measure the rate of ATP binding and population of the weakly bound states at 10 – 37 °C. Mixing actomyo1b^{IQ} with ATP

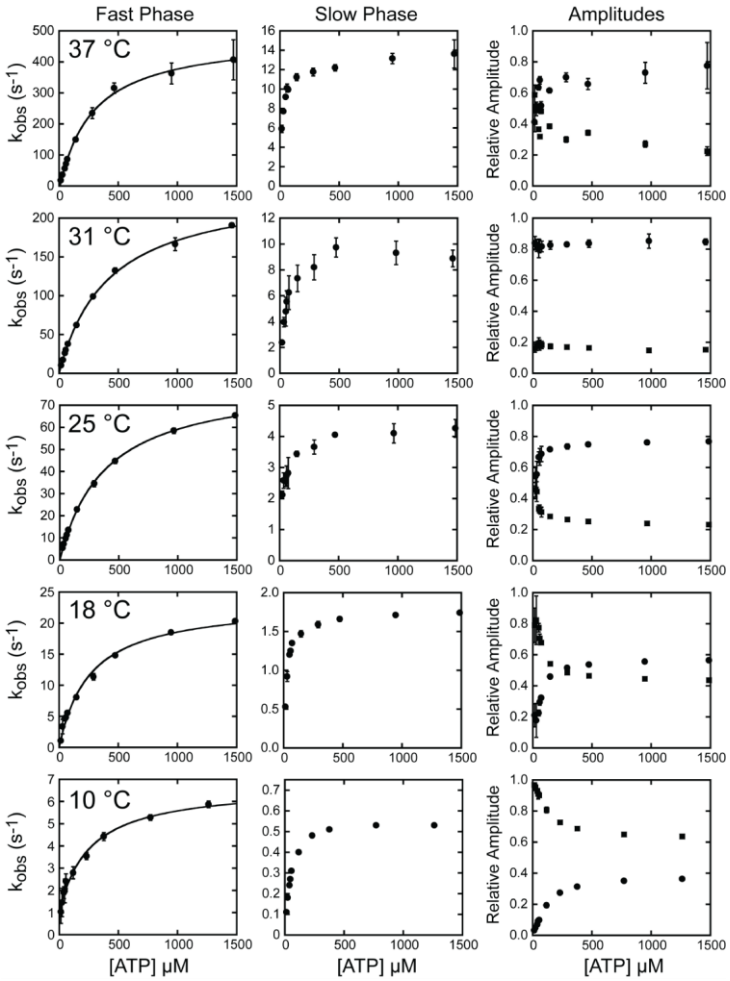

Figure 2.4 - *MgATP induced population of weakly bound actomyo1b^{IQ} states.*

Pyrene-fluorescence transients obtained by mixing 1.0 µM actomyo1b^{IQ} with various ATP concentrations at 10 – 37 °C were fitted to double exponential functions (k_{obs}= $A_{fast}(1\text{-}e^{-kfast \cdot t})$ + $A_{slow}(1\text{-}e^{-kslow \cdot t})$). The rates of the (left column) fast phases and (center column) slow phases are plotted as a function of ATP concentration. (Right column) Normalized amplitudes of the (●) fast and (■) slow phases are plotted as a function of ATP concentration. The solid lines through the data in the left column are the best fits of the rates of the fast phases to equation 2.3.1.

resulted in a transient increase in pyrene-actin fluorescence. No lag phase was present, and the transients were best fit to the sum of two exponential rates with positive amplitudes (**Figure 2.3**). The rates of the fast phases were hyperbolically related to the ATP concentration (**Figure 2.4**, left column), whereas the rates of the slow phases were independent of ATP concentrations greater than 500 μM (**Figure 2.4**, center column).

Geeves et al (**41**) modeled the fast phase of the increase in pyrene-actin fluorescence as ATP binding to the AM state and subsequent population of the AM.ATP state (K_1'k_{+2}'), and proposed that the slow phase reports the transition from a nucleotide-insensitive AM state to a AM' state that can bind ATP ($k_{+\alpha}$) as follows:

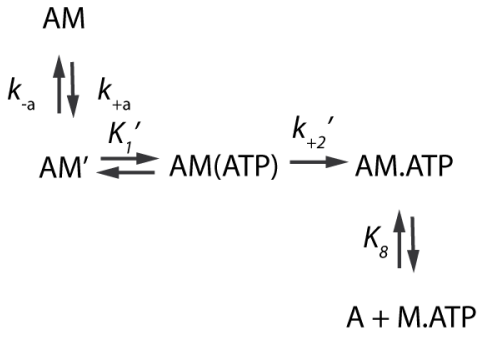

Scheme 3

where A^* represents the unquenched fluorescent state of pyrene-actin. We analyzed the ATP dependence of the fast phase as:

$$k_{obs} = \frac{k'_{+2}[\mathrm{ATP}]}{\frac{1}{K'_1} + [\mathrm{ATP}]}$$

2.3.1

where, K_1' is a rapid equilibrium and k_{+2}' is a rate-limiting isomerization to the high fluorescence AM.ATP state. Values for K_1' and k_{+2}' at 10 – 37 °C are given in Table 2.1. K_1' is relatively insensitive to temperature, while k_{+2}' varies > 80-fold between 10 – 37 °C. An Arrhenius plot of K_1'k_{+2}' is linear and yields an activation energy (E_a) of 111 kJ/mol (**Figure 2.5**; **Table 2.3**).

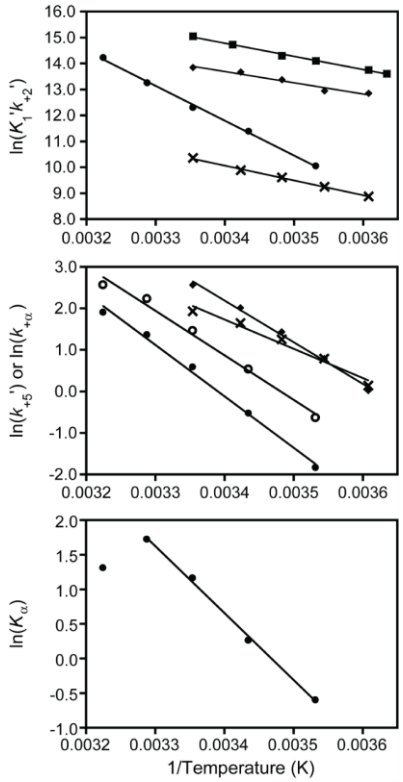

Figure 2.5 - *Temperature dependence of ATP binding and ADP release.*

Arrhenius plots of the natural log of the rates of (top) ATP binding (K_1'k_{+2}') and (center) ADP release (k_{+5}') *versus* inverse temperature (283 - 310 K) for (●) myo1b^{IQ}, (■) myosin-II (**73**), (♦) myosin-V (**75**), and (×) myosin-VI (*30*). The center plot also includes the temperature dependence of (○) $k_{+\alpha}$ for myo1b^{IQ}. Solid lines are linear fits of the data to the Arrhenius equation (equation 2.2.1) yielding E_a's given in **Table 3**. (Bottom) van't Hoff plot of K_α showing non-linearity at temperatures > 31 °C. The solid line is a linear fit of the 283 - 304 K data to the van't Hoff equation (equation 2.2.2), yielding $\Delta H° = 81$ kJ/mol.

	37 °C	31 °C	25 °C	18 °C	10 °C
$1/K_1$' (μM)	330 ± 25	420 ± 15	380 ± 10	260 ± 26	250 ± 53
k_{+2}' (s^{-1})	500 ± 15	240 ± 3.7	82 ± 0.86	23 ± 0.85	5.7 ± 0.28
K_1'k_{+2}' ($\mu M^{-1}s^{-1}$) [b]	1.5 ± 0.12	0.57 ± 0.022	0.22 ± 0.062	0.088 ± 0.0094	0.023 ± 0.0050
K_α	3.7 ± 0.65	5.6 ± 0.25	3.2 ± 0.077	1.3 ± .024	0.55 ± 0.092
$k_{+\alpha}$ (s^{-1})	13 ± 1.0	9.3 ± 1.0	4.3 ± 0.35	1.7 ± 0.023	0.53 ± 0.0071
$k_{-\alpha}$ (s^{-1}) [b]	3.5 ± 0.67	1.7 ± 0.19	1.3 ± 0.11	1.3 ± 0.030	0.96 ± 0.16
k_{+5}' (s^{-1})	6.7 ± 0.064	3.9 ± 0.036	1.8 ± 0.014	0.59 ± 0.0041	0.16 ± 0.0011

[a] KMg25 (10 mM MOPS (pH 7.0), 25 mM KCl, 1 mM EGTA, 1 mM DTT, 1 mM $MgCl_2$) plus 1 μM CaM.

[b] Calculated

Table 2.2 - *Temperature Dependence of ATP Binding and ADP Release.*[a]

Temperature Dependence of ATP Binding		
	E_a for K_1'k_{+2}' (kJ/mol)	E_a for k_{+2}' (kJ/mol)
[a]Myo1b^{IQ}	111	124
[b]Myosin-II	42.4	N.D.
[c]Myosin-V	35.8	74.9
[c]Myosin-VI	47.5	33.8

Temperature Dependence of k_{+5}' and $k_{+\alpha}$'	
	E_a (kJ/mol)
[a]Myo1b^{IQ} ($k_{+\alpha}$)	89.1
[a]Myo1b^{IQ} (k_{+5}')	103
[c]Myosin-V (k_{+5}')	83.3
[c]Myosin-VI (k_{+5}')	58.6

[a]This study.

[b]Data from Millar and Geeves (**73**).

[c]Data from Robblee et al (**75**).

Table 2.3 - *Thermodynamic Parameters for ATP Binding, ADP Release, and $k_{+\alpha}$.*

At high ATP concentrations (> 500 μM), the rate of the slow phase reports the isomerization of AM to AM' ($k_{+\alpha}$), and the ratio of the amplitudes (**Figure 2.4**, right column) of the fast phase to the slow phase reports the equilibrium constant between AM and AM' (**41**). Values for K_{α}, $k_{+\alpha}$, and $k_{-\alpha}$ at 10 – 37 °C were determined by averaging points acquired at ATP concentrations > 1 mM at each temperature (**Table 2.2**). K_{α} varies ~10-fold, while $k_{+\alpha}$ ranges from 0.53 s^{-1} at 10 °C to 13 s^{-1} at 37 °C (**Table 2.2**). An Arrhenius plot of $k_{+\alpha}$ is linear with an E_a of 89.1 kJ/mol (**Figure 2.5**; **Table 2.3**). At low ATP concentrations, the rate of the slow phase shows an apparent ATP concentration dependence. This dependence is due the fact that the slow rate of ATP binding at low ATP concentrations is $\leq k_{+\alpha}$.

2.3.1.3 ATP Hydrolysis

Binding of mantATP to myo1b^{IQ} does not result in a fluorescence change when the mant fluorophore is excited directly (**40**). However, we detect a fluorescence change when the mantATP is excited by energy transfer from the intrinsic tryptophans of myo1b^{IQ}. The rate of the fluorescence transient is mantATP dependent at concentrations < 50 μM, with a maximum rate of 41 ± 4.9 s-1 (**Figure 2.6**). We propose this maximum rate to be the rate of ATP hydrolysis ($k_3^{app} = k_{+3} + k_{-3}$):

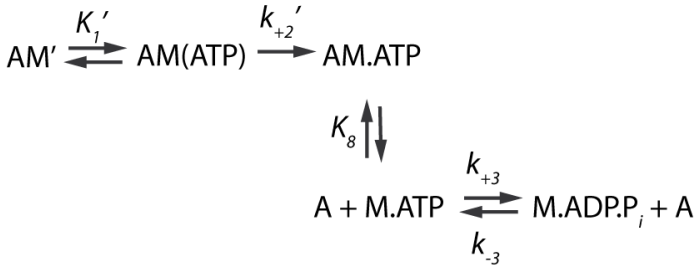

Scheme 4

where M.ADP.P_i^* is the high fluorescence state.

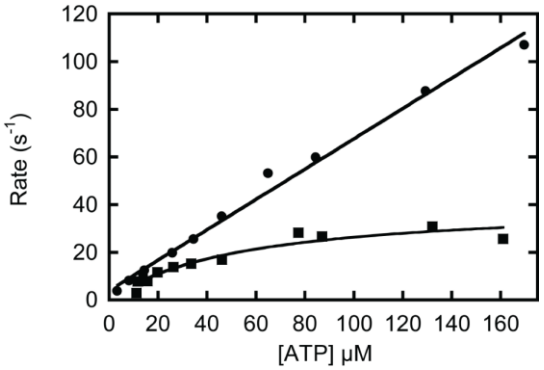

Figure 2.6 - *Rate of ATP hydrolysis by myo1b^{IQ} as measured by mantATP fluorescence.*

(■) MantATP concentration dependence of the rate of change in mant fluorescence upon binding and fluorescence energy transfer from the intrinsic tryptophans of myo1b^{IQ} at 37 °C. (●) Rate of actomyo1b^{IQ} dissociation as a function of mantATP as measured by light scattering at 37 °C.

The increase in mant fluorescence is not due to the ATP binding (K_1'k_{+2}') or actomyo1b^{IQ} dissociation (k_8) steps. We monitored the rate of mantATP-induced actomyo1b dissociation by light scattering and found the dissociation rate to be linearly related to all mantATP concentrations tested (**Figure 2.6**). A linear fit of the data yields a rate of mantATP binding (K_1'k_{+2}' = 0.64 ± 0.02 μM^{-1}s^{-1}; **Table 2.1**). This mantATP-

induced dissociation is ~ 2-fold slower than ATP-induced dissociation as measured by pyrene-actin fluorescence (1.5 ± 0.081 $\mu M^{-1}s^{-1}$; **Table 2.1**).

2.3.1.4 Phosphate Release

Fluorescently-labeled phosphate-binding protein (P_iBP) was used to measure directly the rate of phosphate release (k_{+4}') in sequential-mix, single-turnover, stopped-flow experiments (**38**,**59**,**63**,**67**). Myo1b^{IQ} was mixed with ATP, aged 7 s to allow for ATP binding and hydrolysis, and mixed with actin (**Figure 2.7**). After the 7 s ageing time, we expect all ATP to bound to myosin and hydrolyzed, with the M.ADP.P_i state as the predominant intermediate (**Scheme 1**). P_iBP was included with the myo1b^{IQ} and the actin to prevent transients due to phosphate released during the aging time or phosphate contamination in the actin. In the absence of actin, the rate of phosphate release was too slow to measure on the time-scale of the experiment (< 0.01 s^{-1}). However, the time courses of phosphate release were single exponentials at all actin concentrations tested and did not show lag or rapid-burst phases (**Figure 2.7**). The absence of a linear phase confirmed that the experiments report a single turnover. The actin concentration dependence of the observed rate (k_{obs}) was modeled as:

$$k_{obs} = \frac{k'_{+4}[\text{Actin}]}{K_9 + [\text{Actin}]} \qquad \textbf{2.3.2}$$

where K_9 is a rapid equilibrium step and k_{+4}' is irreversible in the absence of free phosphate (**Scheme 1**) (**68**). The actin-dependent rate of phosphate release is hyperbolic

with K_9 = 53 ± 9.8 µM and k_{+4}' = 0.58 ± 0.056 s^{-1}. The maximum rate of phosphate release (k_{+4}') is the same as the maximum steady-state rate of ATP turnover (V_{max} = 0.6 ± 0.1 s^{-1}), and the affinity of the M.ADP.P for actin (K_9) is the same as the K_{ATPase}

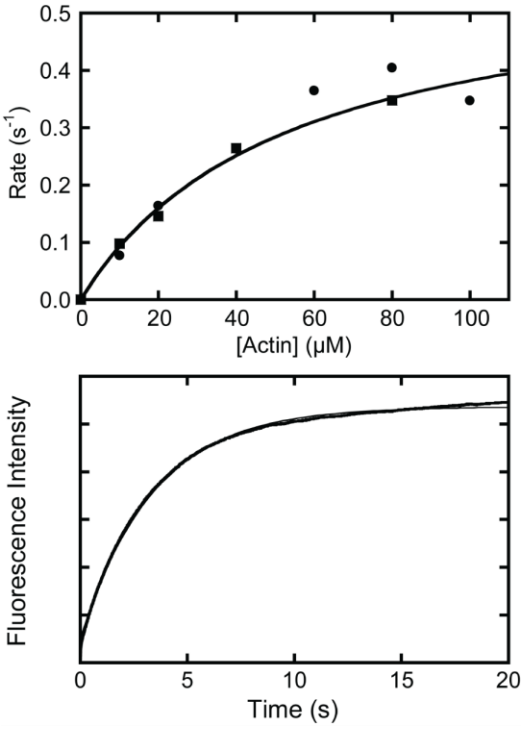

Figure 2.7 - *Steady-state ATPase rate and phosphate release from myo1b^{IQ}*

(Top, ●) Actin dependence of the steady-state ATPase rate of myo1b^{IQ} in KMg25 measured using the NADH-coupled assay at 37 °C. Data is from (**50**). (Top, ■) Actin dependence of the rate of phosphate release (k_4') from 2.5 µM myo1b^{IQ} in the presence of 0 – 80 µM actin, 1.25 µM ATP, and 5 µM P_iBP (concentrations after mixing). The solid line is a fit of the data to equation 2.3.2. Each point is the average of 1 – 3 transients. (Bottom) Time course of transient P_i release from 2.5 µM myo1b^{IQ} after mixing with 1.25 µM ATP, aging for 7 s, and mixing with 40 µM actin in a sequential mix, single turnover experiment in KMg25 at 37 °C. The smooth curve is a single exponential fit to the data (k_{obs}= A(1-$e^{-k \cdot t}$)).

determined in steady-state experiments (50 ± 20 μM; **Figure 2.7**) (**50**). Therefore, the P_i release step is the rate-limiting step in the steady-state ATPase cycle.

2.3.1.5 ADP Release

The rate of ADP release (k_{+5}') was determined by ATP-induced dissociation of myo1b^{IQ} from pyrene-actin at 10 – 37 °C:

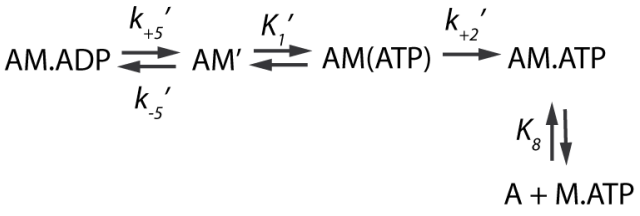

Scheme 5

When myo1b^{IQ} active-sites are saturated with ADP, ATP binding is rate-limited by the slow dissociation of ADP (**40**,**59**). ADP (30 μM final concentration) was incubated with 150 nM pyrene-actomyo1b^{IQ} (final concentration) and mixed to 1 mM ATP (**Figure 2.8**, top). Transients were acquired on a split time-scale to ensure a fast phase was not being overlooked. Transients at 30 μM ADP were best fit by single exponential functions and had rates that ranged from 0.16 s^{-1} at 10 °C to 6.7 s^{-1} at 37 °C (**Figure 2.8**; **Table 2.2**). An Arrhenius plot of the data is linear and yields an E_a of 103 kJ/mol (**Figure 2.5**; **Table 2.3**). The rates and temperature dependence of k_{+5}' are similar to those determined for $k_{+\alpha}$ (**Table 2.2** & **Table 2.3**).

The affinity of actomyo1b^{IQ} for ADP (K_5') was determined at 37 °C (**Figure 2.8**, bottom). In the presence of non-saturating concentrations of ADP, the transient is the sum

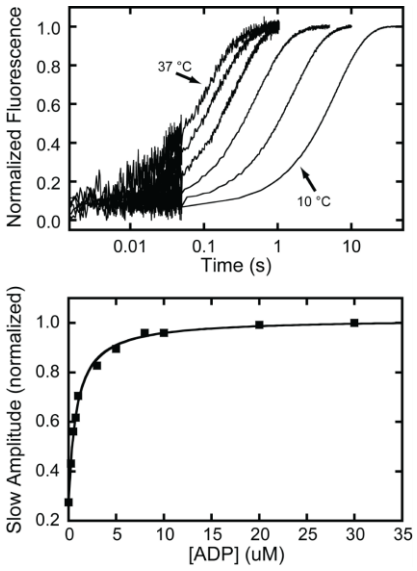

Figure 2.8 - *ADP release from actomyo1b^{IQ}.*

(Top) Temperature dependence of the rate of the pyrene-actin fluorescence increase after mixing 1 mM ATP with 0.15 µM actomyo1b^{IQ} equilibrated with 30 µM ADP. Transients were acquired at 10, 18, 25, 31, and 37 °C. The first 50 ms of the traces were acquired at a higher sampling rate, resulting in larger scatter of the points. Transient acquired in the presence of 30 µM ADP were best fit by single exponential functions. (Bottom) Normalized amplitude of the slow phase obtained by fitting pyrene transients to double exponential functions as a function of ADP concentration at 37 °C. The solid line is a fit of the data to a hyperbola.

of two exponential rates. The rate of the slow component reports the rate of ADP release (k_{+5}'), and the fast phase represents ATP binding to the nucleotide free sites ($K_1'k_{+2}'$). The affinity of the actomyo1bIQ for ADP was determined by monitoring the change in the relative amplitude of the slow phase (**Figure 2.8**, bottom; **42**). A hyperbolic fit to the data yields an affinity, $K_5' = 0.84 \pm 0.068$ µM (**Table 2.1**).

2.3.2 Myosin I can act as a molecular force sensor

2.3.2.1 Basic mechanical and kinetic properties of the myosin Ib working stroke

This study characterizes the basic mechanical properties of myosin Ib isoform "b" (myo1b^{b}), whose effective lever-arm length is determined by 5 CaM-binding IQ motifs in its light chain binding domain (LCBD) (**Figure 2.1**). The mechanical working stroke of myo1b^{b} was probed using a three-bead configuration, in which a filament of actin, strung between beads held in two optical traps, is lowered over a single myo1b^{b} tethered to a pedestal bead by a biotin-streptavidin linkage (see Section 2.2.5; **19**,**46**, **69**). This assay allows the measurement of the displacement of the bead-actin-bead assembly in the two traps that is caused when myo1b^{b} attaches to the actin and undergoes its working stroke. The working stroke of myo1b^{b} occurs in two sub-steps (**19**), as has been shown previously (**43**). The first and second sub-steps have displacements of 5.1 ± 0.43 nm and 3.3 ± 0.35 nm, giving a total displacement of 8.4 nm (**19**).

The rates associated with the transition from the first to second sub-step (k_{start}) and from the second sub-step to actin detachment (k_{end}) were calculated from fits to the ensemble averages of myo1b^{b} actin-attachment events measured in the presence of ATP concentrations ranging from 1 – 50 μM (**19**). The rate k_{start} was found to be relatively insensitive to ATP concentration with rates of k_{start} = 0.37 to 0.77 s^{-1} (**19**), which is similar to the ADP release rate of 1.0 s^{-1} at 22 °C (see Section 2.3.1.5 and **Table 2.2**). On the other hand, k_{end} was found to linearly increase with ATP concentration with a corresponding second order rate constant of k_{end} = 0.48 $\mu M^{-1}s^{-1}$ (**19**) that agrees well with the apparent rate of 0.22 $\mu M^{-1}s^{-1}$ measured for ATP binding at room temperature (see Section 2.3.1.5 and **Table 2.2**).

2.3.2.2 Myosin Ib actin attachment lifetimes are dramatically decreased in the presence of loads

The effect of stress on the actin detachment kinetics of myo1b[b] was determined using a feedback system that applies a dynamic load to actomyo1b to keep the actin near its isometric position (**19**). Thus, as myo1b undergoes its working stroke, the load applied to the actomyo1b depends on the size and direction of the displacement. The duration of actin attachment was observed to increase >75-fold at isometric forces of < 2pN (see **Figure 2.9; 19**). The detachment of myo1b[b] from actin was modeled with force dependent (k_g) and force-independent (k_i) rates of detachment:

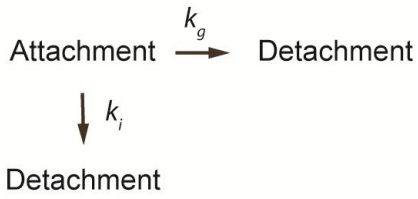

Scheme 6

and the force dependence of the detachment rate (k_{det}) was derived as

$$k_{det}(F) = k_{g0} e^{\frac{-F \cdot d_{det}}{k_b T}} + k_i$$

2.3.3 – Force Dependent Rate Equation

where k_{g0} is the rate of k_g in the absence of force (F), k is the Boltzmann constant, T is temperature, and d_{det} is the distance parameter that reports the distance to the transition state of the force-sensitive step (see Section 5.2 for derivation). Fits of the attachment durations (see **Figure 2.9; 19**) were performed by optimizing a maximum likelihood

(MLE) model (see Section 5.1) using a probability distribution function based on equation 2.3.3 (see Section 5.2). Best fit parameters from the MLE optimization are k_{g0} = 1.6 s^{-1} (+0.5/-0.35 s^{-1}) and d_{det} = 12 nm (+1.6/-3.0 nm) (see **Figure 2.9**; **19**). The level of force sensitivity represented by the distance parameter d_{det} = 12 nm is unprecedented in the myosin family (**70**,**71**).

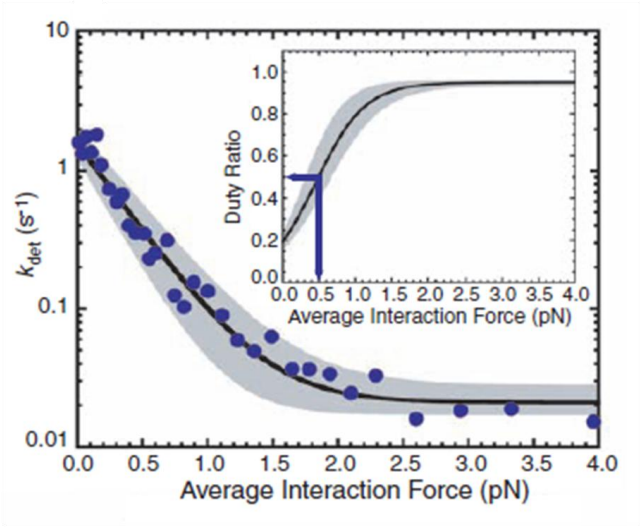

Figure 2.9 – *Low levels of force lead to drastic decrease in rate of actin detachment for myosin Ib.*

2.3.3 Dependence of effective lever-arm length on the mechanical activity of isoforms of myosin Ib

2.3.3.1 Lever-arm length dependence of the myosin Ib step-size

The mechanical working stroke of four constructs of myo1b (**Figure 2.1**) was probed using the three-bead configuration in an optical trap (see Sections 2.2.5 and 2.3.2;

26, **19**,**46**, **69**). These four constructs included recombinant versions of the three native splice isoforms (myo1b^{a}, myo1b^{b}, myo1b^{c}; and one artificial construct (myo1b^{IQ}) whose light chain binding domains (LCBD) contained 6, 5, 4, or 1 IQ motifs, respectively (**50**). Optical trap experiments were carried out at low ATP concentrations ([ATP] = 1 μM) to give long actin attachment times for more precise step-size determination (see Sections 2.3.1.2 and 2.3.2; **26**). Means from the normal distributions resulting from the binning of the displacements from the first 50 ms and the last 50 ms of individual attachment events gave the length of the first substep and the total step-size; the second sub-step size was calculated from the mean of the distribution resulting from taking the difference of these two measurements for each event (see Section 2.2.6; **26**). These distributions were obtained for each of the four constructs, from which the total step-sizes were calculated yielding values of 12, 8.1, 9.6 and 2.8 nm for myo1b^{a}, myo1b^{b}, myo1b^{c} and myo1b^{IQ}, respectively (see **Figure 2.10**; **26**). These step-sizes are plotted against the corresponding number of IQ motifs in the LCBD for each of the four constructs, in which the step-sizes vary with IQ number in a non-linear fashion (**Figure 2.10**; **26**).

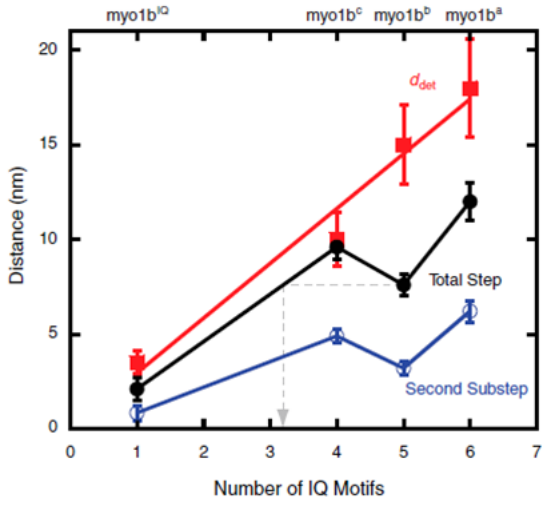

Figure 2.10 – *Force dependence as measured by distance parameter (d) is directly related to the length of the lever arm of myo1b*

Force vs. rate of detachment plot. *Inset:* Effect of force on the duty ratio of myo1b.

2.3.3.2 Lever-arm length dependence of the myo1b force sensing ability

The effect of stress on the actin detachment kinetics of the four myo1b constructs (myo1b^{a}, myo1b^{b}, myo1b^{c} and myo1b^{IQ}) was determined using the force feedback system described in Section 2.3.2.2 (**19**). The detachment of myo1b from actin was modeled with force dependent (k_g) and force-independent (k_i) rates of detachment according to Scheme 6 and equation 2.3.3 (see Section 2.3.2.2). Simultaneous fits of the attachment durations from the four constructs (see **Figure 2.11**) were performed by optimizing a maximum likelihood (MLE) model (see Section 5.1 for a full description) using a probability distribution function based on equation 2.3.3 (see Sections 5.2). The simultaneous fits led to a higher precision in the calculation of the parameters k_{g0}, k_i and d_{det}. The rates k_{g0} and k_i were assumed to be the same for the four constructs in the simultaneous fits, yielding values of k_{g0} = 0.51 ± 0.11 s^{-1} and k_i = 0.013 s^{-1} (+0.0025/-0.0017 s^{-1}) (see **Figure 2.11**; **26**). The rate of actin detachment in the presence of saturating levels of ADP was

measured in the stopped flow at k_{off} = 0.0036 ± 0.00036 s^{-1}, very similar to the force independent detachment rate (k_i). The distance parameters calculated from the simultaneous fit over events from myo1b[a], myo1b[b], myo1b[c] and myo1b[IQ] were d_{det} = 18 ± 2.6 nm, 15 ± 2.1 nm, 10 +1.5/-1.4 nm and 3.5 +0.67/-0.61 nm, respectively (**Figure 2.11**; **26**). Plotting these distance parameters against the corresponding IQ number of the myo1b construct (see **Figure 2.10**) shows the linear dependence of the distance parameter (d_{det}) to the effective lever arm length.

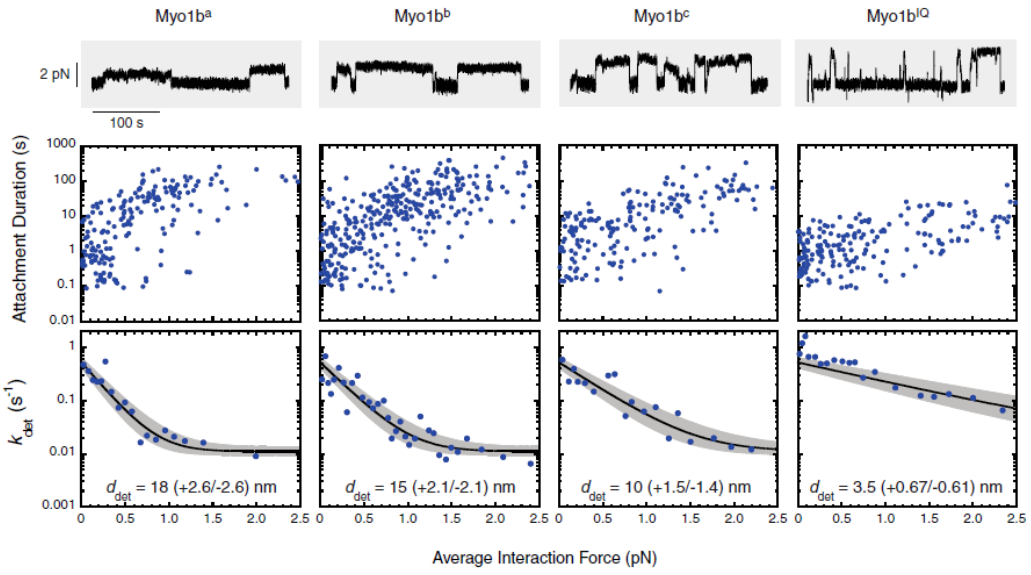

Figure 2.11 – *Isoform dependence of myo1b force sensing*

Above: Force (pN, x-axis) plotted against Attachment Durations (sec, y-axis) for each actin binding event measured for (left to right) Myo1b[a], Myo1b[b], Myo1b[c] and Myo1b[IQ]. *Below:* Force (pN, x-axis) plotted against rate of detachment (k_{det} (s^{-1}), y-axis) for actin binding events averaged every 10 data points.

2.3.4 Calcium Regulation of the Chemomechanical Activity of Myosin Ib

2.3.4.1 Calcium sensitivity of steady state ATPase rate of myosin Ib

Calcium binding to the calmodulin associated with the IQ motif closest to the motor domain modulates the ATPase kinetics of the protein (**50**), so we used myo1b^{IQ} to determine the effect of calcium on the actin-activated ATPase cycle at 37 °C. The steady-state ATPase rate in the presence of 20 μM actin increased ~10-fold from 0.16 ± 0.027 s^{-1} to 1.4 ± 0.016 s^{-1} at free calcium (Ca^{2+}_F) concentrations > 1 μM (**Figure 2.12**). The effective calcium binding affinity was determined by fitting the ATPase data to the Hill equation (**72**), yielding K_d = 0.10 ± 0.021 μM (**Table 2.6**).

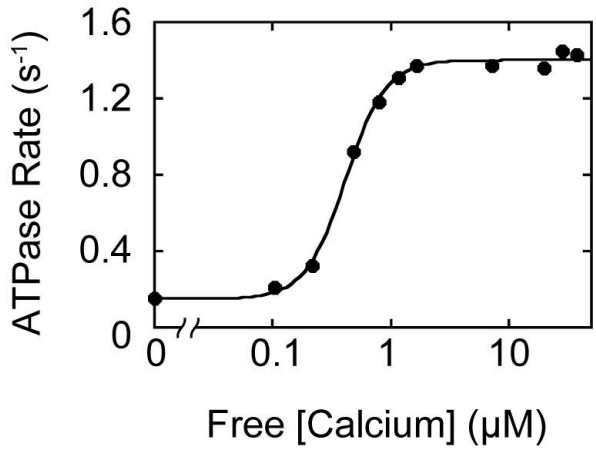

Figure 2.12 - *The Steady State ATPase Rates for Myosin-1b are Highly Sensitive to Calcium Concentration.*

All experiments were done at 37° C in the presence of calcium concentrations ranging from 0 – 40μM. Calcium dependence of the actin-activated steady state ATPase rate for Myo1b-IQ at high ATP (2mM) and a fixed actin concentration (20 μM). Best fit to Hill equation give an affinity of K_d = 0.10 ± 0.021 μM. Each point represents the average of three experiments.

2.3.4.2 Calcium sensitivity of the key steps in the ATPase cycle of myosin Ib

Rate and equilibrium constants associated with ATP binding, ATP hydrolysis and ADP release (**Scheme 1**) were measured as described in Section 2.3.1 in the presence or absence of 100 μM free calcium (**Table 2.4** and **Figure 2.13**). ATP binding is only moderately affected by calcium, with its effective rate K_1k_{+2}' increased ~ 2-fold by calcium (see Section 2.3.1.2, **Table 2.4** and **Figure 2.13**). The rate of going from the closed to open nucleotide-free state ($k_{+\alpha}$) is relatively unaffected by the introduction of calcium, whereas the reverse rate, $k_{-\alpha}$, is increased 1.9-fold (**Table 2.4**). The rate of ATP hydrolysis ($k_3^{app} = k_{+3} + k_{-3}$) in the presence and absence of 100 μM calcium was measured using mantATP (see Section 2.3.1.3). The maximum rates in the presence and absence of 100 μM calcium are 41 ± s^{-1} and 39 ± s^{-1}, respectively (**Figure 2.14** and **Table 2.4**), suggesting that calcium binding does not affect ATP hydrolysis. The rate of ADP release is measured at [ADP] > 10 μM, where the pyrene transients are best fit to single exponential functions (see Section 2.3.1.5) with rates of 6.7 s^{-1} and 11.3 s^{-1} in the absence and presence of 100 μM calcium, respectively (**Table 2.4** and **Figure 2.13**). The affinity of ADP binding, K_5', was similar both in the presence and absence of 100 μM calcium with a value of 0.85 μM (**Table 2.4**).

Fluorescently labeled phosphate-binding protein was used to measure the rate of phosphate release (k_{+4}'). Phosphate release is typically measured in sequential mix experiments where myosin and ATP are mixed and aged to form the M.ADP.Pi state, followed by mixing with various actin concentrations (see Section 2.3.1.4). However,

ATP Binding		
	-Calcium	+Calcium
$1/K_1'$ (μM)	330 ± 25[b]	236 ± 52[b]
k_{+2}' (s^{-1})	500 ± 15[b]	771 ± 60[b]
$K_1'k_{+2}'$ ($\mu M^{-1}s^{-1}$)	1.5 ± 0.1[c]	3.3 ± 0.8[c]
$K_1'k_{+2}'$ ($\mu M^{-1}s^{-1}$)	1.2 ± 0.04[b,d]	2.0 ± 0.04[b,d]

Nucleotide-Free Isomerization Step		
	-Calcium	+Calcium
K_α	3.7 ± 0.7[b]	2.1 ± 0.2[b]
$k_{+\alpha}$ (s^{-1})	13.0 ± 1.0[b]	14.0 ± 1.5[b]
$k_{-\alpha}$ (s^{-1})	3.5 ± 0.7[c]	6.7 ± 1.0[c]

Phosphate Release		
	-Calcium	+Calcium
k_{+4}' (s^{-1})	0.58 ± 0.06[e]	1.45 ± 0.03[e]
K_9 (μM)	53 ± 10[e]	5.5 ± .4[e]

ADP Release		
	-Calcium	+Calcium
K_5' (μM)	0.84 ± 0.07[b]	0.85 ± 0.11[b]
k_{+5} (s^{-1})	6.7 ± 0.06[b]	11.26 ± 0.11[b]
k_{-5} ($\mu M^{-1}s^{-1}$)	8.0 ± 0.7[c]	13.25 ± 1.7[c]

ATP Hydrolysis		
	-Calcium	+Calcium
k_3^{app} (s^{-1})	41 ± 4.9[f]	39 ± 3.2[f]

[a] KMg25 (10 mM MOPS (pH 7.0), 25 mM KCl, 1mM EGTA, 1mM DTT, 1mM $MgCl_2$, ±100μM $CaCl_2$, 37° C)
[b] Pyrene-actin fluorescence
[c] Calculated
[d] Determined from a linear fit of the data at low ATP concentrations
[e] Phosphate-binding protein
[f] MantATP

Table 2.4 - *Rate and Equilibrium Constants for the Myo1bIQ ATPase Cycle in the Presence and Absence of Calcium at 37°C.*[a]

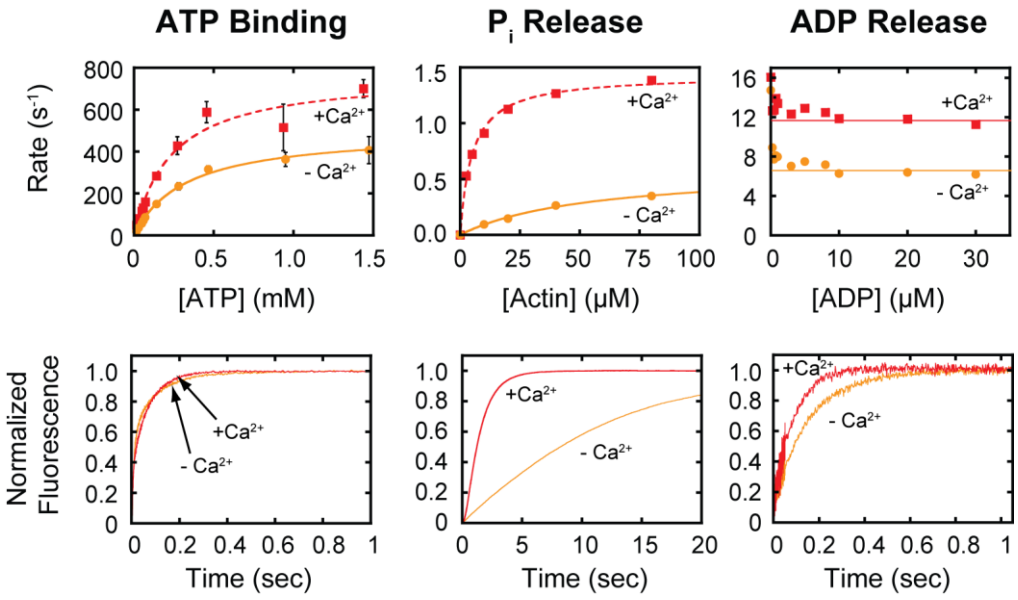

Figure 2.13 - *Calcium-Dependence of the Rates of ATP Binding (far left), P_i Release (center) and ADP Release (far right) as Observed with Myo1b^{IQ}.*

All experiments were done at 37° C in the presence (■) or absence (●) of 100 μM $CaCl_2$ and fit to either single or double exponential functions. These data points are fit by hyperbolae colored light red (100 μM $CaCl_2$) or dark red (0 μM $CaCl_2$). Representative transients are shown below, and are similarly colored. ***Far Left, Top***: Pyrene-fluorescence transients were obtained by mixing 1.0 μM actomyo1b^{IQ} with various ATP concentrations. The rates obtained from the fast phase were plotted against ATP concentration and fit to a hyperbolic function, as represented by the solid lines. ***Center, Top***: Actin dependence of the rate of phosphate release (k_4') from 2.5 μM myo1b^{IQ}. The solid lines are a fit of the data to hyperbolae. Each point is the average of 1 – 6 transients. ***Far Right, Top***: The rate of pyrene-actin fluorescence increase after mixing 1mM ATP with 0.15 μM actiomyo1b^{IQ} equilibrated with various concentrations of ADP.

pre-equilibration of myosin and calcium at 37° C in the absence of actin resulted in occasional protein aggregation. Therefore, single-mix single-turnover experiments were performed by mixing 1 μM ATP with pre-mixed 3 μM myo1b^{IQ}, 100 μM calcium, and 0 - 80 μM actin. Time courses of the phosphate-binding transients contained a small lag phase due to ATP binding and hydrolysis (**Scheme 1**). The transients were well fit by a

double exponential function, where one rate emerged as actin dependent (**Figure 2.13**). The actin-independent rate was found to be consistent with the rate of ATP binding at 1 μM ATP (~3.3 s^{-1}) in the presence of calcium for all actin concentrations. The absence of a linear component in the transient confirms that the myosin underwent a single turnover. Using equation 2.3.2, the rate of phosphate release, k_{+4}', was found to be 2.8 times faster in the presence of calcium than in its absence (**Table 2.4** and **Figure 2.13**). Furthermore, the affinity of the M.D.Pi complex for actin, K_9, was increased 7.6-fold (**Table 2.4**).

Overall, calcium increases the rates of ATP binding, phosphate release (k_4'), and ADP release (k_5') 2 – 3 fold, but does not affect the rate of the ATP hydrolysis step (k_3) (**Table 2.4** and **Figure 2.13**). The rate constant for phosphate release (k_4') increases nearly 3-fold (**Table 2.4** and **Figure 2.13**), but remains the rate-limiting step.

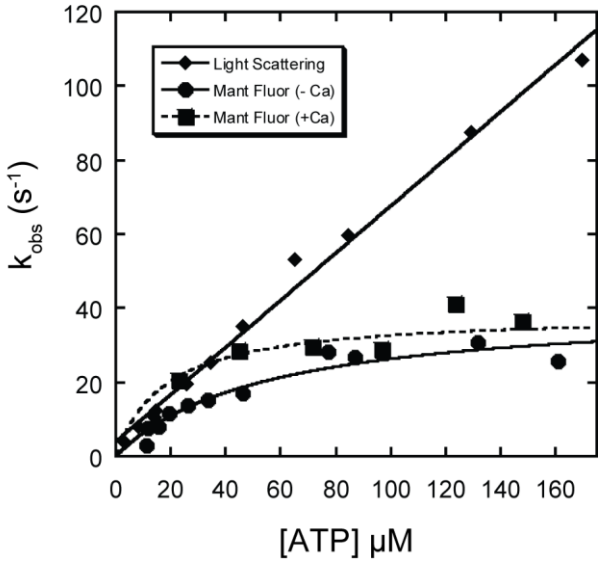

Figure 2.14 – *Presence of 100 μM free calcium does not appreciably affect the apparent rate of ATP hydrolysis ($k_{app} = k_{+3} + k_{-3}$).*

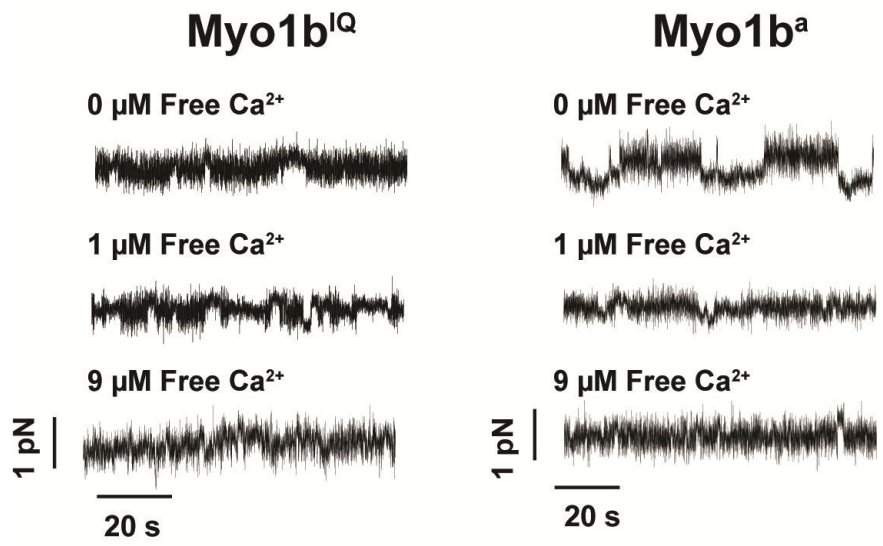

Figure 2.15 - *Calcium Dependence of the Step-Sizes (center) and Lifetimes of Attachment (bottom) for Myo1b^{IQ} (left) and Myo1b^{a} (right).*

All experiments were performed in the optical trap at room temperature and 25 µM ATP in the presence of 0 µM, 1 µM or 9 µM Calcium. ***Top:*** Traces of actin displacement by Myo1b^{IQ} (***Left***) and Myo1b^{a} (***Right***) at 0 µM, 1 µM and 9 µM Calcium. Scale bars are 1 pN, vertical bar, and 20 s, horizontal bar.

2.3.4.3 Calcium decreases the actin-attachment lifetime of myo1b

The kinetics of the interactions of myo1b^{IQ} and myo1b^{a} with actin in the presence of 0, 1 and 9 µM free calcium were determined at the single molecule level with an optical trap using the three-bead configuration (**Figure 2.15**)(see Section 2.2.5; **19**,**46**, **69**). In the presence of 25 µM ATP, myo1b actin-attachment durations decreased in with increasing concentrations of calcium (**Figure 2.18**). The distribution of actin attachments in the absence of calcium were best fit to a probability density function that is a linear combination of two exponential rates:

$$P(t_i; k_0, k_1, f) = f \cdot k_0 \cdot e^{-k_0 \cdot t_i} + (1 - f) \cdot k_1 \cdot e^{-k_1 \cdot t_i}$$

2.3.4

where t_i are the attachment durations, and k_0, k_1 and f ,$(1-f)$ are the rates and relative frequencies of these two events, respectively. The k_0 rates for both myo1b^{IQ} (k_0 = 0.20 +0.028/-0.021 s^{-1}) and myo1b^{a} (k_0 = 0.25 +0.057/-0.064 s^{-1}) (**Table 2.5**) are consistent

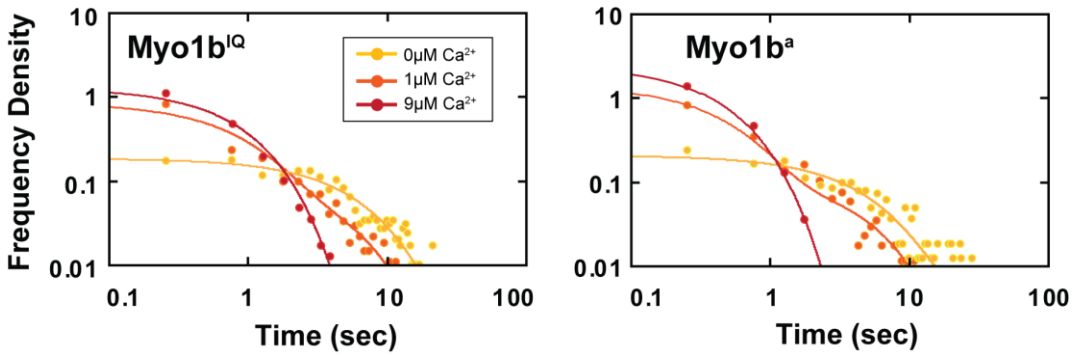

Figure 2.16 – *Calcium-dependence of the durations of actin attachment for myo1b^{IQ} (left) and myo1b^{a} (right).*

All experiments were performed in the optical trap at room temperature and 25 μM ATP in the presence of 0 μM, 1 μM or 9 μM Calcium. Durations of actin attachment are measured for each event from covariance threshold analysis. Intrinsic rates of attachment are calculated from this data using a Maximum Likelihood routine combined with a global optimization of both isoforms at each calcium concentration.

with the rate of ADP release (k_5') at 20 °C (see Section 2.3.1.5). The rates of the long duration component was similar in both constructs (k_1 = 0.054 s^{-1}, f_1 = 0.12 for myo1b^{IQ}; k_1 = 0.057 s^{-1}, f_1 = 0.23 for myo1b^{a}; **Table 2.5**).

Step Sizes for Myo1b^{IQ} and Myo1b^{a} [a]				
	$[Ca^{2+}]$ = 0μM		$[Ca^{2+}]$ = 9μM	
	Myo1b^{IQ}	Myo1b^{a}	Myo1b^{IQ}	Myo1b^{a}
Total Step (nm)	2.2 ± 0.37	12.2 ± 0.81	1.2 ± 0.17	1.7 ± 0.39
Step 1 (nm)	1.4 ± 0.24	9.0 ± 0.57	0.72 ± 0.10	1.2 ± 0.31
Step 2 (nm)	0.80 ± 0.44	3.2 ± 0.57	0.48 ± 0.20	0.50 ± 0.44

Lifetimes of Actin Attachment for Myo1b^{IQ} and Myo1b^{a} [a,c]				
	$[Ca^{2+}]$ = 0μM		$[Ca^{2+}]$ = 9μM	
	Myo1b^{IQ}	Myo1b^{a}	Myo1b^{IQ}	Myo1b^{a}
k_0 (s^{-1})	0.20 +0.028/-0.021	0.25 +0.057/-0.064	1.3 +0.092/-0.090	2.4 +0.053/-0.12
k_1 (s^{-1})	0.054 +0.014/-0.019	0.057 +0.031/-0.030	NA	NA
f_0	0.89 +0.13/-0.032	0.77 +0.15/-0.16	NA	NA
f_1	0.11 +0.13/-0.032	0.23 +0.15/-0.16	NA	NA
$f_{[Ca]=1\mu M}$	0.43 +0.039/-0.056	0.46 +0.047/-0.058	0.57 +0.039/-0.056	0.54 +0.047/-0.058
	$[Ca^{2+}]$ = 1μM			
	Myo1b^{IQ}	Myo1b^{a}		
$k_{0,+Ca}$ (s^{-1})	2.4 +1.3/-2.2	2.3 +1.3/-1.2		
$k_{0,-Ca}$ (s^{-1})	0.15 +0.058/-0.064	0.31 +0.087/-0.096		
$f_{0,+Ca}$	0.55 +0.24/-0.11	0.5 +0.26/-0.13		
$f_{0,-Ca}$	0.45 +0.24/-0.11	0.5 +0.26/-0.13		

Calcium Dependence of Myo1b^{a} Force Sensitivity [a,b,c]		
	$[Ca^{2+}]$ = 0μM	$[Ca^{2+}]$ = 9μM
k_{g0} (s^{-1})	0.74 +0.12/-0.23	0.66 +0.19/-0.16
k_i (s^{-1})	0.013 +0.004/-0.002	NA
d_{det} (nm)	18 +2.6/-2.6	2.9 +0.48/-0.56

[a] Performed in the optical trap using Motility Buffer (*materials and methods*) and 25 μM ATP at 23 °C.

[b] Isometric force was applied ranging from 0 - 5 pN using a force feedback system (see M*aterials and Methods*).

[c] Fit to a probability distribution function and optimized with a MLE routine; 90% confidence interval(see M*aterials and Methods*)

Table 2.5 - *Calcium dependence of mechanics of Myo1ba and Myo1bIQ at room temperature.*[a]

The distribution of actin attachments at 9 μM Ca^{2+}_F, a concentration at which the effect of the calcium on the ATPase rate is saturated (Figure 2.18), could be fit to a single-exponential probability distribution:

$$P(t_i; k_0) = k_0 \cdot e^{-k_0 \cdot t_i}$$

2.3.5

where the calculated k_0 rate was faster for myo1b^{IQ} (k_0 = 1.3 +0.092/-0.090 s^{-1}) and myo1b^{a} (k_0 = 2.4 +0.053/-0.12 s^{-1}) (**Table 2.5**) than in the absence of calcium. The actin-attachment distributions at 1 μM Ca^{2+}_F, an intermediate calcium concentration (**Figure 2.18**), were best fit using equation 2.3.4, yielding values for the two rates that are very similar to the respective k_0 rates from the 0 and 9 μM Ca^{2+} distributions ($k_{0,-Ca}$ = 0.15 +0.027/-0.021 s^{-1}, $k_{0,+Ca}$ = 2.4 +0.11/-0.11 s^{-1} (myo1b^{IQ}); $k_{0,-Ca}$ = 0.31 +0.096/-0.087 s^{-1}, $k_{0,+Ca}$ = 2.3 +1.3/-1.2 s^{-1} (myo1b^{a})) (**Figure 2.18** and **Table 2.5**). The relative frequency of the bound species is $f_{0,+Ca}$ = 0.55 for myo1b^{IQ} and $f_{0,+Ca}$ = 0.50 for myo1b^{a} (**Table 2.5**) at 1 μM Ca^{2+}_F. We can calculate an effective affinity for calcium binding using a simple single calcium binding model that assumes the two sub-populations of myo1b in the presence of 1 μM Ca^{2+} belong to the calcium-bound and unbound species:

$$f_{bound} = \frac{[Ca^{2+}]}{K_d + [Ca^{2+}]}$$

2.3.6

At $[Ca^{2+}]$ = 1 μM and $f_{bound} = f_{9\mu M}$, effective calcium binding affinities were calculated for myo1b^{a} and myo1b^{IQ} of K_d = 1 μM and 0.8 μM, respectively.

Time of Measurement After Ca^{2+} is Added	ATPase[b]		ADP Release[c]		Trp Fluorescence[d]	
	K_d (μM)	n_{Hill}	K_d (μM)	n_{Hill}	K_d (μM)	n_{Hill}
2 ms	—	—	3.2 ± 0.68	0.84 ± 0.15	3.6 ± 2.1	0.83 ± 0.32
5 min	0.10 ± 0.021	2.6 ± 0.24	0.85 ± 0.15	2.2 ± 0.33	1.8 ± 0.80	2.4 ± 0.88

[a] KMg25 bufer (10 mM MOPS (pH 7.0), 25 mM KCl, 1mM EGTA, 1mM DTT, 1mM $MgCl_2$, ±100μM $CaCl_2$, 37° C)

[b] Determined from the pre-calcium-dependent change in the Steady State ATPase rate.

[c] Determined from the calcium-dependent change in the rate of ADP release

[d] Determined from the calcium-dependent change in the amplitude of Trp fluorescence.

Table 2.6 - *Calcium Dependence of Steps in the Myo1bIQ ATPase Cycle at 37°C.*[a]

Individual motors from 1 μM Ca^{2+} parent distributions[b]	0μM Ca^{2+} parent distriubtion[b]		9μM Ca^{2+} parent distriubtion[b]	
	$Myo1b^{IQ}$	$Myo1b^{a}$	$Myo1b^{IQ}$	$Myo1b^{a}$
$Myo1b^{IQ}$				
1 μM Ca^{2+} Total	7.44E-24	—	7.59E-28	—
motor 1	5.78E-21	—	5.65E-13	—
motor 2	7.08E-01	—	6.78E-20	—
motor 3	3.62E-09	—	1.76E-08	—
motor 4	1.28E-12	—	4.21E-04	—
$Myo1b^{a}$				
1 μM Ca^{2+} Total	—	4.72E-26	—	2.13E-29
motor 1	—	5.66E-30	—	4.21E-18
motor 2	—	2.47E-07	—	2.71E-16
motor 3	—	2.18E-01	—	7.21E-15

[a] Null hypothesis is that distributions are from the same parent distribution, see Materials and Methods

[b] Performed in the optical trap using Motility Buffer (materials and methods) and 25 μM ATP at 23 °C.

Table 2.7 - *p-values from Kolmogorov-Smirnov two distribution test, testing the hypothesis that distributions are from different parent distribution.*[a]

The presence of the two distributions in the presence of 1 μM Ca^{2+}_F could be due to a dynamic exchange of calcium on single myo1b molecules during the experimental time-course, or to stable calcium-bound and calcium-free populations. We therefore examined the actin-attachment durations of individual experiments that make up the parent distribution. Using the Kolmogorov-Smirnov two-distribution test, we found that the individual experiments are statistically different from the 0 and 9 μM Ca^{2+}_F parent distributions (p-values < 0.001, **Table 2.7**), suggesting that the effects of calcium binding and releasing from individual motors occur on a time course faster than the experiment.

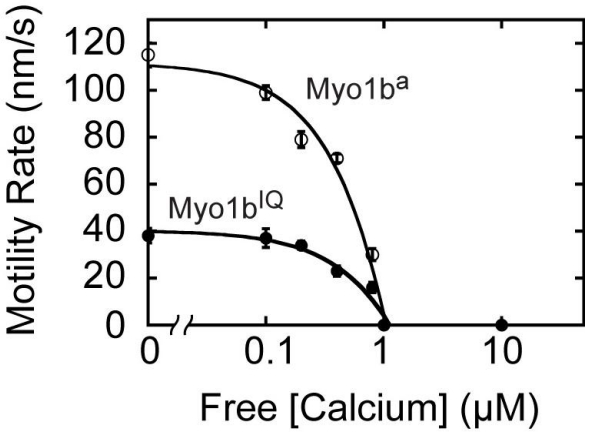

Figure 2.17 - *The Motility rates for myosin-1b are highly sensitive to calcium concentration.*

All experiments were done at 37° C in the presence of calcium concentrations ranging from 0 – 10μM. Calcium dependence of the Myo1b-IQ and Myo1b-a driven motility of actin filaments at high ATP (2mM). The tick on the log plot is defined at zero calcium.

2.3.4.4 Calcium inhibits actin gliding and decreases the myo1b working stroke

The ensemble-level mechanical activities of myo1b^a and myo1b^{IQ} were measured using an actin gliding assay (**Figure 2.17**). Myo1b proteins were site-specifically

attached to streptavidin-coated cover slips via a biotinylation tag positioned directly C-terminal to the IQ motifs, and actin gilding rates were measured in the presence of 0 – 10 µM Ca^{2+}_{F}. Motility rates of myo1b^{a} (120 ± 5.1 nm/s) at low calcium were ~ 3-fold faster than myo1b^{IQ} (38 ± 3.1 nm/s) as a result of the proteins having different lever arm lengths (**50**). Unidirectional actin gliding was eliminated for both constructs at > 1 µM Ca^{2+}_{F}, despite the increased ATPase activity (**Figure 2.12** and **Figure 2.17**).

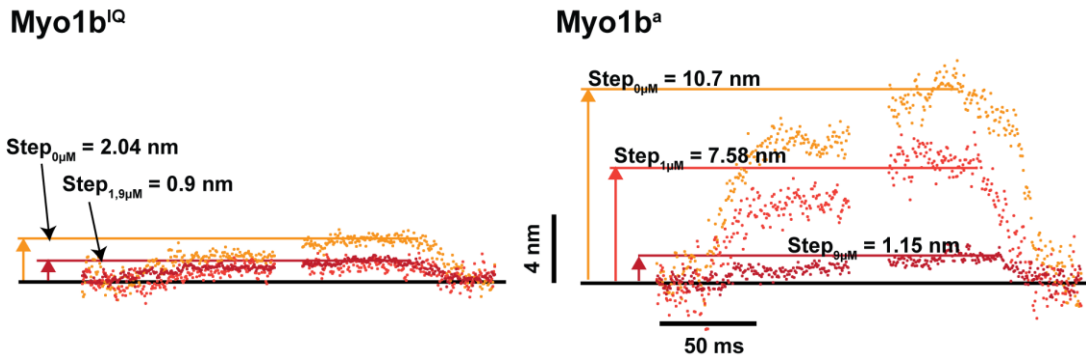

Figure 2.18 – *Calcium-dependence of the step-sizes for myo1b^{IQ} (left) and myo1b^{a} (right).*

All experiments were performed in the optical trap at room temperature and 25 µM ATP in the presence of 0 µM, 1 µM or 9 µM Calcium. Steps of individual displacement events are measured from the first 50 ms (step 1) and the last 50 ms (total step) of attachment. The second step is calculated from the difference of these two for each event.

The size of the unitary working strokes of myo1b^{IQ} and myo1b^{a} were determined in the presence and absence of calcium with an optical trap (Sections 2.2.5, 2.3.2.2, and 2.3.3.2). We've demonstrated already that the myo1b working-stoke occurs in two substeps (Section 2.3.2.1; **19**). Therefore, we determined average substep sizes by ensemble averaging the time-courses of unitary interactions synchronized at their start

times to determine the average displacement of the first substep and their end times to determine the average displacement of their total step (**Figure 2.18**). In the absence of calcium and in the presence of 25 μM ATP, the total step displacements were 11 nm and 2.0 nm for myo1b^{IQ} and myo1b^{a}, respectively. Binding of 9 μM $Ca^{2+}{}_{F}$ to myo1b^{a} and myo1b^{IQ} resulted in a dramatic reduction of their step-sizes to 1.2 nm and 0.9 nm, respectively (**Table 2.5** and **Figure 2.18**). Addition of 1 μM $Ca^{2+}{}_{F}$ resulted in the average step-sizes decreasing to 7.6 nm and 0.9 nm for myo1b^{a} and myo1b^{IQ} , intermediate to the step-sizes observed for these constructs when in the presence of 0 and 9 μM $Ca^{2+}{}_{F}$ (**Figure 2.18**). If we assume the step-sizes at the intermediate calcium concentration ($[Ca^{2+}]$ = 1 μM) result from the step-sizes of calcium bound and unbound myo1b, we calculate the frequency of bound species f_{bound} = 0.35. Using this estimate for f_{bound} in equation 2.3.6 with $[Ca^{2+}]$ = 1 μM yields an effective calcium binding affinity of K_d = 1.9 μM.

2.3.4.5 Calcium decreases actin attachment lifetimes in the presence of loads

The effect of stress on the actin detachment kinetics of myo1b^{a} was determined using a feedback system that applies a dynamic load to actomyo1b to keep the actin near its isometric position (see Sections 2.2.5 and 2.3.2). We previously demonstrated that actin-attachment durations of myo1b^{a} increase with increasing forces until a plateau is reached at ~ 1 pN, after which attachment durations are limited by the basal rate of ADP-bound myo1b from actin (**Figures 2.11** and **2.19**; **26**). Attachment durations in the presence of 9 μM $Ca^{2+}{}_{F}$ are substantially less force dependent and a plateau is not apparent at forces up to 4 pN (**Figure 2.19**).

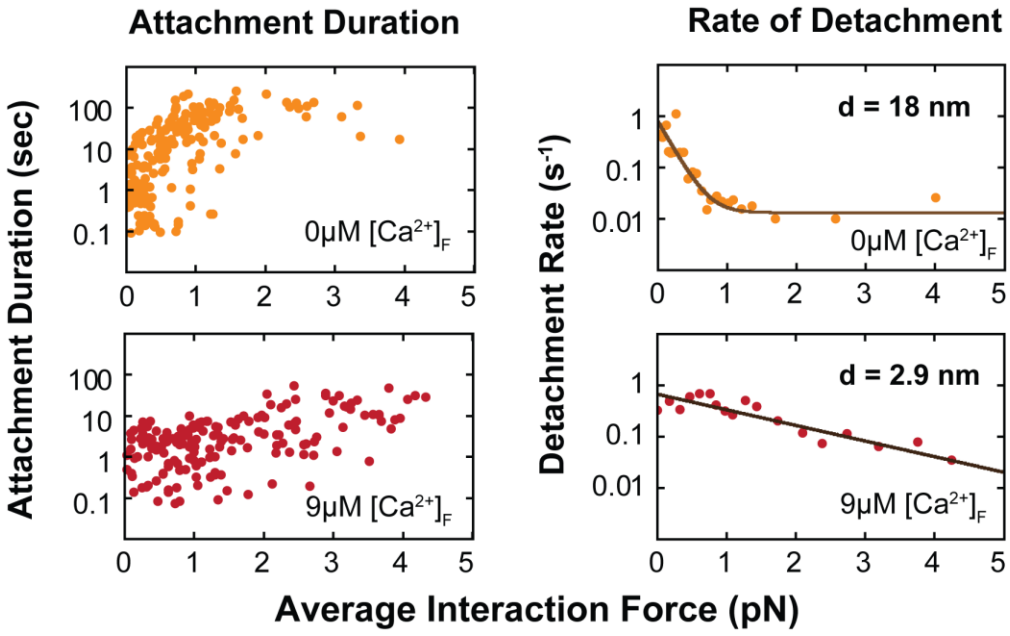

Figure 2.19 – *Calcium-dependence of the force sensitivity of Myo1b*[a] *as measured by its distance parameter, d.*

The relationship between attachment durations vs. applied force is shown for all events (*left*). These events were also binned according to force and plotted vs. their rates of detachment (*right*). These data were fit according to equation 2.3.3, which describes how the rate at zero force is influenced by applied force. This revealed a drastic reduction in the distance parameter, *d*, for myo1b[a] when going from 0 μM (d = 18 nm, *top*) to 9 μM calcium (d = 2.9 nm, *bottom*).

The detachment of myo1b[a] from actin was modeled with force dependent (k_g) and force-independent (k_i) rates of detachment according to Scheme 6 and equation **2.3.3** (see Section 2.3.2.2). Fits of the attachment durations (see **Figure 2.19**) were performed by optimizing a maximum likelihood (MLE) model (see Section 5.1) using a probability distribution function based on equation **2.3.3** (see Section 5.2). Fits of the attachment durations in the absence of calcium yielded values of k_{g0} = 0.74 s^{-1}, d_{det} = 18 nm, k_i = 0.013 s^{-1} (see Section 2.3.3; **26**) (**Table 2.5**). The best fit d_{det} value in the presence of 9 μM $Ca^{2+}{}_F$ (d_{det} = 2.9 nm, **Table 2.5**) is 6-fold smaller than in the absence of calcium (see

Section 2.3.3; **26**). This difference in force sensitivity is most clearly seen in plots of the detachment rate as a function of force (**Figure 2.19**). The decrease in the distance parameter corresponds remarkably well to the 7-fold decrease in working stroke displacement upon addition of 9 μM calcium, and is very similar to the d_{det} determined for myo1b^{IQ} in the absence of calcium (d_{det} = 3.5 nm, see Section 2.3.3; **26**).

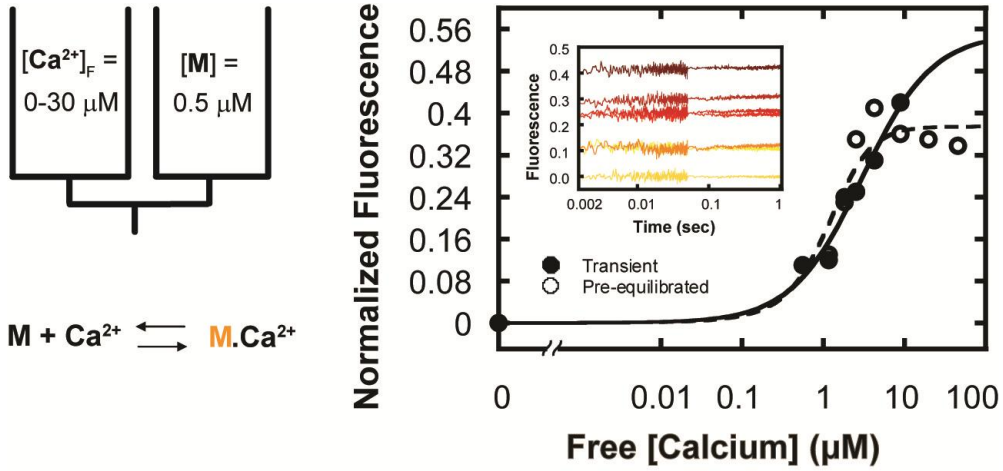

Figure 2.20 – *The calcium-dependent increase in the intrinsic tryptophan fluorescence of Myo1b^{IQ} is rapid.*

Left and Inset*:** Calcium concentrations ranging from 0 – 9 μM (yellow to dark red) are introduced to 0.5μM Nucleotide-free Myo1b^{IQ} in a stopped-flow at 37 °C. The change in intrinsic Trp fluorescence is observed at 305nm. Little to no portion of the rising phase is observed at all calcium concentrations, indicating that the reaction has come to completion within the dead-time of the instrument (~2ms). ***Right: Normalized amplitudes of the measured Trp fluorescence as a function of calcium concentration obtained from transient experiments (open diamonds) as well as experiments where Myo1b is pre-equilibrated with calcium (filled circles). The results are both fit by the Hill equations over a range of calcium concentrations (0 – 40 μM) yielding the effective affinities of K_d = 3.6 μM and K_d = 1.8 μM from the transient and pre-equilibrated calcium experiments, respectively.

2.3.4.6 The effect of calcium binding on myosin Ib conformation and kinetic activity is rapid

Stopped-flow experiments were performed to measure the rates of calcium binding's effect on the conformation and kinetic activity of myo1b. Calcium's effect on myo1b conformation was measured by a calcium-dependent change in the intrinsic tryptophan (Trp) fluorescence of myo1b^{IQ}. In these experiments, concentrations of calcium ranging from 0-15 μM were rapidly mixed with 0.5 μM nucleotide-free myo1b^{IQ} and the resulting Trp fluorescence was measured (see schematic in **Figure 2.20**). The amplitudes of the resulting transients reach their steady state levels within the dead-time of the instrument (2ms), indicating rapid (>1000 s^{-1}) calcium binding and response of the myo1b conformation to that binding (**Figure 2.20**, inset). Plots of the calcium dependence of these amplitudes are fit by the Hill equation, giving an effective affinity of K_d = 3.6 μM and n = 0.83 (**Figure 2.20** and **Table 2.6**). Complementary experiments performed where myo1b^{IQ} is pre-equilibrated with a range of calcium from 0 - 30 μM ~5 minutes prior to measurement of the Trp fluorescence demonstrate an effective calcium binding affinity of K_d = 1.8 μM and n = 2.4 (**Figure 2.20** and **Table 2.6**).

The effect of calcium-binding on the kinetic activity of myo1b was measured through the calcium-dependent change in the rate of ADP release of myo1b^{IQ}. In these experiments, concentrations of calcium ranging from 0-30 μM and 2 mM ATP were rapidly mixed with 1 μM acto-myo1b^{IQ} saturated with 30 μM ADP (see schematic in **Figure 2.21**). The amplitudes of all of the resulting transients have a fast and a slow components (**Figure 2.21**, inset), the same as in the calcium-free ADP release experiments (see Section 2.3.1.5). This indicates that the effect of calcium binding on the

rate of ADP release occurs within the dead time of the instrument (2 ms), as in the Trp fluorescence experiments. Plots of the calcium dependence of these amplitudes are fit by the Hill equation, giving an effective affinity of K_d = 3.2 μM and n = 0.84 (**Figure 2.21** and **Table 2.6**). Complementary experiments performed where myo1b^{IQ} is pre-equilibrated with a range of calcium from 0 - 30 μM ~5 minutes prior to the mixing experiment demonstrate an effective calcium binding affinity of K_d = 0.85 μM and n = 2.2 (**Figure 2.21** and **Table 2.6**).

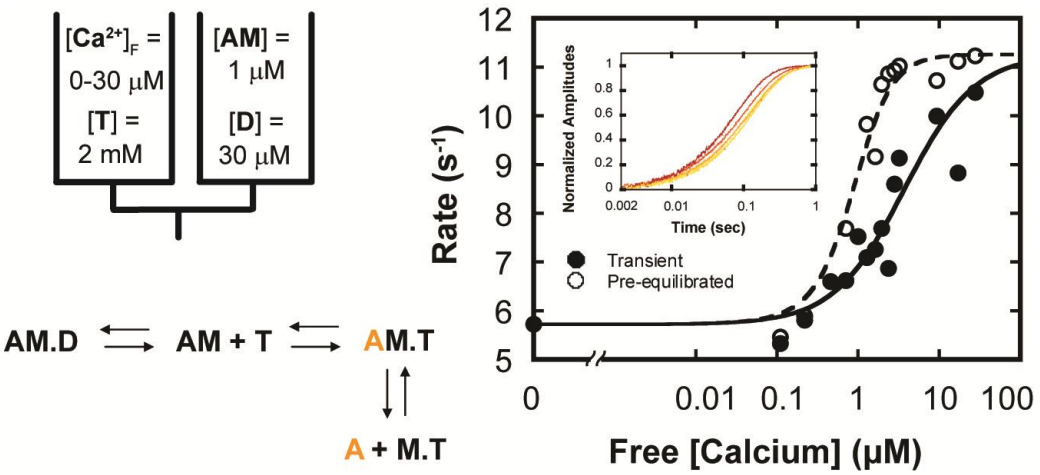

Figure 2.21 - *Calcium-dependent increase in the ADP Release Rate k_{+5}' for myo1b^{IQ} is rapid.*

Left and Inset*:** The rate of ADP release is measured in the stopped flow as before (see Section 2.3.1.5) at calcium concentrations ranging from 0 – 9 μM (yellow to dark red). Little to no portion of any amplitudes attributable to calcium binding are observed at all calcium concentrations, indicating that the reaction has come to completion within the dead-time of the instrument (~2ms). ***Right: Rates of ADP release as a function of calcium concentration obtained from transient experiments (open diamonds) as well as experiments where myo1b is pre-equilibrated with calcium (filled circles). The results are both fit by the Hill equations over a range of calcium concentrations (0 – 30 μM) yielding the effective affinities of K_d = 3.2 μM and K_d = 0.85 μM from the transient and pre-equilibrated calcium experiments, respectively.

2.4 DISCUSSION

2.4.1 Temperature dependence of nucleotide association and kinetic characterization of myo1b

2.4.1.1 ATP Binding

We confirmed previous results (**40**,**41**,**42**) showing the apparent second-order rate constant for ATP binding to actomyo1b^{IQ} to be much slower than other characterized myosins at ambient temperature (**Table 2.2**). Actomyo1b^{IQ} binds ATP ~30-fold slower than skeletal muscle myosin-II at 18 °C (**Figure 2.5**; **73**). However, at 37 °C, myo1b^{IQ} binds ATP only 5-fold slower than skeletal muscle myosin-II, and binds ATP faster than long- and short-tail myosin-I isoforms from *Acanthamoeba* (**36**) and *Dictyostelium* (**39**,**74**) at the physiological temperatures of these organisms.

An Arrhenius plot of the rate of ATP binding (K_1'k_{+2}') to actomyo1b^{IQ} yields an E_a of 111 kJ/mol, which is 2.5-fold greater than determined for myosins-II and -VI and 3-fold greater than determined for myosin-V (**Figure 2.5**; **Table 2.3**). This monstrous temperature dependence is the greatest reported for any myosin and highlights the importance of determining rate constants at physiological temperature when correlating kinetics with biological function. The isomerization step (k_{+2}') is responsible for the temperature dependence of the overall reaction, as is reflected in the similar activation energies for the steps associated with K_1'k_{+2}' and k_{+2}' (**Table 2.3**).

The equilibrium constant K_1' changes less than 2-fold between 10 – 37 °C (**Table 2.2**), supporting the assignment of the AM(ATP) state as a collision complex. This

property is similar to the initial binding steps of myosins –II and –V, but differs from myosin-VI, which has ~ 15-fold weaker K_1' (**75**). The initial ATP binding step for myosin-VI is not a true collision complex, but is best modeled by a rapid isomerization between a nucleotide-sensitive state and a nucleotide-insensitive state, similar to the much slower transition (k_α; **Scheme 1**) reported for myo1b (**75**). The sequence of "loop 1" of the myo1b motor domain has been shown to modulate this transition (**42**), thus it is plausible that this region also plays a role in regulating a similar transition in other myosins.

2.4.1.2 AM to AM' transition

The maximum rate of ATP binding (k_{+2}') is 143-fold faster than the transition from the nucleotide accessible state (AM') to the nucleotide inaccessible state (AM) at 37 °C ($k_{-\alpha}$; **Table 2.1**). Therefore, the AM state (**Scheme 1**) is not significantly populated during steady-state ATP hydrolysis.

The rates and equilibrium constants that define the AM to AM' transition depend on the temperature to a lesser extent than ATP binding (**Figure 2.5**; **Table 2.3**). A van't Hoff plot of K_α is linear from 10 – 31 °C with a break occurring at 31 °C (**Figure 2.5**). The slope between 10 – 31 °C yields an enthalpy (ΔH°) of 81 kJ/mol. There is high experimental confidence in the 37 °C point, since it is the result of multiple transients acquired at two ATP concentrations. Thus, the non-linearity in the plot is likely due to a change in the standard molar heat capacity ($\Delta C_P°$) of actomyo1b^{IQ}. Changes in $\Delta C_P°$

indicate a significant conformational change in the protein as it approaches physiological temperatures (**75**).

2.4.1.3 ATP Hydrolysis

We propose that the change in fluorescence of mantATP, excited by fluorescence resonance energy transfer, is due to a conformational change in the myosin that positions the active site to catalyze ATP hydrolysis (**Scheme 4**). Muscle myosins show a similar change in fluorescence as a result of an environmental change around tryptophan 510 (**76**,**77**), and an equivalent tryptophan is present in myo1b. We were unable to measure a change in tryptophan fluorescence directly in the presence of actin because of the low signal to noise at 37 °C and the presence of a high fluorescence background from the actin.

The observed fluorescence change is not due to mantATP binding (K_1'k_2') or actomyo1b^{IQ} dissociation (k_8), since light scattering measurements indicate that the rate does not saturate at high mantATP concentrations (**Figure 2.6**). Additionally, this fluorescence change is not reporting a conformational change due to phosphate release (k_{+4}'), since it is > 10-fold faster than the rate-limiting step. Therefore, the fluorescence change is most likely the conformational change that limits the rate of ATP hydrolysis (**76**,**77**).

2.4.1.4 Phosphate Release

The actin-concentration dependence of phosphate release (K_9 = 53 ± 9.8 μM and k_{+4}' = 0.58 ± 0.056 s^{-1}; **Table 2.1**) is identical to the actin-concentration dependence of the steady-state ATPase activity (K_{ATPase} = 50 ± 20 μM and V_{max} = 0.6 ± 0.1 s^{-1}; **50**). Therefore, phosphate release is the rate-limiting step, and the predominant steady-state intermediates are the M.ADP.P_i and AM.ADP.P_i states.

The rate of phosphate release from actomyo1b^{IQ} is much slower than other characterized myosins, even when one considers physiological temperatures. For example, phosphate release from activated *Acanthamoeba* myosin-Ic = 24 s^{-1} (**67**), myosin-V > 100 s^{-1} (**59**,**78**), and skeletal muscle myosin-II = 75 s^{-1} (**63**). It is not clear why myo1b evolved to have a slow rate of phosphate release, but it is likely that the motor is kinetically tuned to optimally sense tension allowing for force-dependent changes in its duty ratio (see below).

2.4.1.5 ADP Release

The rate of ADP release (k_{+5}') from myo1b^{IQ} is slow at all assayed temperatures (**Table 2.2**). An Arrhenius plot yields an E_a of 103 kJ/mol, which is comparable to other myosins that have slow rates of ADP release (**Figure 2.5** and **Table 2.3**), suggesting that the ADP release mechanisms for these myosins are similar.

The kinetic rates and E_a of the AM to AM' transition are remarkably similar to the rates and E_a of ADP release (**Table 2.2** and **Table 2.3**); suggesting a similar structural change is responsible for both transitions. Recent work provides evidence that a common

structural element of myo1b modulate both the rate of ADP release and k_{α} (**42**). Therefore, it is likely that k_{+5}' and $k_{+\alpha}$ are reporting the same structural transition, which in the case of ADP release, includes a rotation of the myo1b lever arm. As pointed out by Geeves et al (**41**), in the presence of a load that resists lever arm rotation, the rate of $k_{-\alpha}$ may increase and $k_{+\alpha}$ may decrease to such an extent that the AM state becomes a predominant steady-state intermediate (see below).

2.4.1.6 Relationship to other myosin-I isoforms

Myosin-I isoforms can be broadly divided into long-tail and short-tail classes based on the sequences of their motor and tail domains (**16**). Both classes follow a common ATPase pathway and have low duty ratios (< 0.1), but rate constants that define the pathways vary by > 10-fold. Based on previous studies, we predicted that all short-tail isoforms have slow rate constants (long intermediate lifetimes), and all long-tail isoforms have fast rate constants (short intermediate lifetimes) (**38**). These kinetic differences provide insight into the function of the isoforms. For example, the long lifetimes of the force-bearing intermediates of the short-tail isoforms are likely important for proposed tension-sensing and structural roles (**16**).

A recent report shows *Dictyostelium* myosin-IE (Dmyo1e), a short-tail isoform, has rate constants significantly faster at 20 °C than vertebrate short-tail isoforms measured at the same temperature (**39**). We show in this study that many of the myo1b^{IQ} rate constants are of similar magnitude to Dmyo1e when the rates are compared at the respective physiological temperatures of each organism. For example, ATP binding to

and ADP release from actomyo1b^{IQ} at 37 °C are within 4-fold of Dmyo1e at 20 °C. Given these similarities, large kinetic differences are still present. Most notably, phosphate release from actomyo1b^{IQ} at 37 °C is 15-fold slower than the steady-state ATPase rate of Dmyo1e.

Given the variation in rate constants within the short-tail subclass, it does not appear that one can predict precisely the lifetimes of the biochemical intermediates based on the myosin-I subclass alone. However, it is clear that all characterized short tail isoforms have a relatively slow rate of ADP release, a nucleotide-insensitive actin-bound state, and a low ADP coupling ratio (K_5'/K_5; **79**) as measured previously for myo1b (**40**), supporting the prediction that these isoforms are tuned for tension-sensing or tension-maintenance (**37**,**38**,**40**,**5**).

2.4.2 Myosin I can act as a molecular force sensor

2.4.2.1 The two steps of the myosin Ib working stroke are linked to ADP release and ATP binding

This study characterizes the basic mechanical properties of splice isoform "b" of myosin Ib (myo1b^{b}), whose effective lever-arm length is determined by 5 CaM-binding IQ motifs in its light chain binding domain (LCBD) (**Figure 2.1**). The working stroke of myo1b^{b} measured from optical trap experiments has a displacement of 8.4 nm, with displacements for the first and second sub-steps of 5.1 nm and 3.3 nm, respectively (see Section 2.3.2.1; **19**). The measured rate (k_{start}) of the first sub-step was found to be insensitive to the concentration of ATP, while the rate from the second sub-step (k_{end})

was found to linearly increase with increasing ATP concentrations (see Section 2.3.2; **19**). In addition, the values for the rates k_{start} and k_{end} agree closely with those of ADP release and ATP binding measured at 22 °C. These findings lead to the conclusion that the first and second mechanical steps of the myo1b working stroke correspond to the ADP release and ATP binding steps in the ATPase cycle (see Section 2.3.2; **19**). The assignments of these kinetic steps to the sub-steps of the power stroke are consistent with the findings for other myosin family members with two step power strokes (**43**,**31**).

2.4.2.2 Myosin Ib actin attachment lifetimes are dramatically decreased in the presence of loads

In the presence of 50 μM ATP and in the absence of applied force, the rate of actin detachment is k_{g0} = 1.6 s^{-1} (see Section 2.3.2.2; **19**). This agrees closely with the ADP release rate at 22 °C, which is rate limiting at higher ATP concentrations (see Section 2.3.1.5 and **Table 2.2**). The detachment rate (k_g) increases up to 75-fold when isometric forces < 2 pN are applied to myosin Ib (**Figure 2.9**; **19**). Since the rate of ADP release limits exit from the strong binding states, and the rate of P_i release limits the rate into the strong binding states (and all other rates are significantly faster), the duty ratio of myo1b under high ATP and actin concentrations can be defined as:

$$\text{duty ratio} = \frac{k'_{+4}}{k'_{+4} + k'_{+5}} \qquad \textbf{2.4.1}$$

The force dependence of the duty ratio can then be calculated using equation 2.4.1, where k_{det}(F) was used in place of k_{+5} and the rate of P_i release (k_{+4} = 0.38 s^{-1}) was measured at 25 °C (see inset of **Figure 2.9; 19**). This plot demonstrates that the major implication of the high force sensitivity of the myo1b power stroke is that myo1b^b switches from a low duty ratio motor (< 0.2) to a high duty ratio motor (> 0.5) at low (< 0.5 pN) forces.

The ADP release step has been shown to be the force sensitive step in other myosin family members (**80**) and was predicted to be the same for myo1b (**81**,**40**). The force dependence of the ends of actin attachment, d_{end}, was shown to be much less than the total d_{det} = 12 nm (d_{end} = 2.5 ± 0.85 nm) (see Section 2.3.2; **19**). Because of the correspondence of the ATP binding step to the ends of attachment (see above), the weak force dependence of this step relative to actin attachment as a whole strongly implicates the ADP release step as the principal force sensitive step (see Section 2.3.2; **19**).

2.4.3 Dependence of effective lever-arm length on the mechanical activity of isoforms of myosin Ib

2.4.3.1 The step-size of myosin Ib is non-linearly dependent on the length of its effective lever arm

We demonstrated that the step-sizes of myo1b^a, myo1b^b, myo1b^c and myo1b^{IQ}, with 6, 5, 4 and 1 IQ motifs in their LCBDs, varies non-linearly relative to the length of its lever-arm with values of 12, 8.1, 9.6 and 2.8 nm, respectively (**Figure 2.10**; **26**). Previous studies on other myosin family members demonstrated a linear dependence of their step-sizes to their respective lever-arm lengths (**48**,**49**). The reason for the different

dependencies of lever-arm length on step-size is not known, but could be due to a larger compliance in the myo1b lever-arm compared to that of the other family members (see Section 2.3.3; **26**).

2.4.3.2 The force sensitivity of myosin Ib is linearly dependent on the length of its effective lever arm

The force sensing abilities of the four myo1b constructs (myo1b^{a}, myo1b^{b}, myo1b^{c} and myo1b^{IQ}) were linearly dependent on the lengths of their respective LCBDs (**Figure 2.10** and **Figure 2.11**). The distance parameters corresponding to myo1b^{IQ} and myo1b^{c} (d_{det} = 3.5 nm (myo1b^{IQ}) and 10 nm (myo1b^{c})) matched closely to the respective total step-sizes of these two constructs (step-size = 2.8 nm (myo1b^{IQ}) and 9.6 nm (myo1b^{c}); **Figure 2.10**). Moreover, the force independent rate of myo1b actin detachment measured in the optical trap experiments (k_i = 0.013 s^{-1}) was similar to the rate of actin detachment of ADP-bound myo1b measured in the stopped flow (k_{off} = 0.0036 s^{-1}; see Section 2.3.3.2). These two observations led to the proposal of a mechanism for the force sensitive transition where the lever-arm under load is pulled back to its pre-power stroke state with the myo1b in a strongly bound state with ADP-like affinity; the force sensitive transition would therefore have to undergo the full power stroke for actin detachment to occur (**26**). This mechanism may not apply for myo1b^{b} and myo1b^{a}, whose measured distance parameters (d_{det} = 15 nm (myo1b^{b}) and 18 nm (myo1b^{a})) were significantly different from their corresponding step-sizes (step-size = 8.1 nm (myo1b^{b}) and 12 nm (myo1b^{a})) (**Figure 2.10**). The reason for this disparity in their total step and distance

parameter is not known, but may result from an increased compliance in their LCBDs arising from different splicing locations (see Section 2.3.3; **26**).

2.4.4 Calcium regulation of the chemomechanical activity of myosin Ib

It has long been recognized that calcium regulates the activity of myosin-I isoforms via calmodulins bound to the LCBD (**53**,**50**). In this study, we reveal the mechanism of myo1b regulation by showing that calcium affects the unitary displacement and force-dependence of myo1b actin-detachment kinetics.

The unitary displacements of both myo1b^{a} and myo1b^{IQ} are reduced to nearly zero (**Figure 2.18** and **Table 2.5**), and actin gliding is completely inhibited in the presence of calcium (**Figure 2.17**). These results indicate that calcium is acting on the calmodulin closest to the motor domain to uncouple structural changes in the motor from LCBD (lever arm) rotation. Structural studies of other myosins show stable interactions between the motor's converter domain and the first light chain. Since calcium-bound calmodulin remains myosin bound under our experimental conditions (**50**, **82**), we propose that rearrangements of the motor-calmodulin interface occur upon calcium binding to disrupt lever arm rotation. These results confirm the proposal that the first light chain is "not merely a passive mechanical device," but rather it plays an important role in mechanical transduction (**83**).

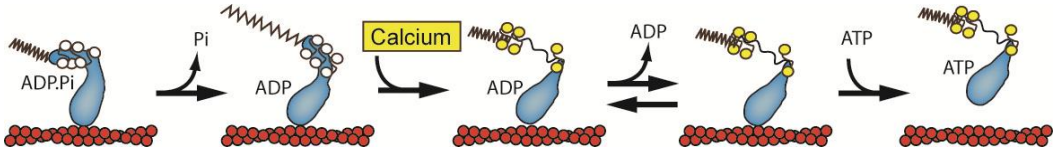

Figure 2.22 – *Model of calcium binding affecting tension sensing of myo1b.*

The force-dependence of the rate of actin detachment is substantially decreased by calcium, with the myo1b[a] distance parameter (d_{det}) decreasing 6-fold (**Figure 2.19** and **Table 2.5**). This decrease correlates with the 7-fold decrease in the unitary step-size (**Figure 2.18** and **Table 2.5**). Our previous work suggests that tension sensing occurs as stress on actomyo1b prevents the rotation of the lever arm, which inhibits ADP release and subsequent ATP binding and actin detachment (see Sections 2.3.2 and 2.3.3; **19**,**26**). Myo1b with shorter LCBDs have shorter unitary displacements and smaller distance parameters (see Section 2.3.3; **26**). Thus, the calcium-shortened myo1b step size results in a shorter distance to the transition state, resulting in decreased force sensitivity.

Calcium activates the unloaded actomyo1b ATPase kinetics (**Figure 2.13** and **Table 2.4**), but given the dramatic calcium-induced effects on myo1b mechanics, changes in the unloaded ATPase kinetics are of secondary importance and are likely a consequence of the rearrangement of the motor-calmodulin interface. Nevertheless, calcium increases the rate of phosphate release (k_{+4}`) 2.5-fold, which results in an increase in the steady-state ATPase activity, as phosphate release is the rate-limiting-step in the absence and presence of calcium. The overall effect of calcium on the unloaded ATPase kinetics is to decrease the lifetime of the intermediate steps < 3-fold, without dramatically changing their relative distributions. This result is different from the effect

of calcium on myo1c, a widely expressed short-tailed myosin-I isoform. Myo1c's rate-limiting step shifts from phosphate release to ATP hydrolysis, which increases the population of the pre-hydrolysis, weak-binding intermediates (**84**). Further experiments are required to determine if calcium affects myo1c mechanics to the same extent as myo1b.

As suggested previously, the slow and force-sensitive kinetic properties of myo1b point to tethering, anchoring, or force sensing functions for myo1b, rather than a myosin-V-like transport role (see Sections 2.3.2 and 2.3.3; **19**, **26**). Myo1b is concentrated on cellular membranes where it is well suited to play roles in controlling membrane morphology and dynamics (**20**,**21**). Because myo1b is membrane bound, it likely experiences calcium transients during a variety of signaling events. Resting cytoplasmic calcium concentrations are generally in a range (50 – 100 nM) below the concentration in which myo1b motility is inhibited. During excitation, the free calcium concentration can exceed 1 μM (**85**), which is above the calcium concentration at which mechanical inhibition occurs (**Figure 2.17** and **Figure 2.15**). Thus, a signaling event that results in a calcium transient will dramatically decrease the actin-attachment lifetime of myo1b working against a load (e.g., myo1b working against a 1 pN load will detach from actin 44-fold faster in the presence of calcium). Additionally, myo1b will not be able to translocate along actin to restore tension during the calcium transient, since motility is effectively inhibited in the presence of calcium. Thus, calcium is an effective means to terminate the remarkably long force-induced myo1b actin attachments.

It must be noted that calcium concentrations during signaling are transient, so the rate at which calcium affects the chemomechanical activity of myo1b is important.

Optical trap and stopped flow experiments support a view of a rapid calcium-binding effect on both mechanics and kinetics. The rate of the calcium-dependent increase in myo1b tryptophan fluorescence, which indicates a conformational change (**86**), was faster than could be measured (>1000 s^{-1}) (**Figure 2.20**, inset). The affinity of this calcium-dependent increase under steady-state conditions (K_d = 1.8 μM; **Table 2.6**) is very close to the affinity estimated from the myo1b step-sizes at intermediate calcium concentrations measured in the optical trap (K_d = 1.9 μM). Stopped flow experiments measuring the calcium-dependence of ADP release also indicated a rapid calcium-binding effect on its rate (**Figure 2.21**). The calcium dependence of the rate of ADP release was shown the same affinity of K_d = 0.85 μM in stopped flow experiments as was calculated from the actin attachment duration distributions at intermediate calcium concentrations (K_d = 0.8 μM, **Table 2.6**). We conclude from the correspondence of these affinities that (1) the rapid calcium-dependent increase in Trp fluorescence is reporting a rapid conformational change in myo1b that accompanies the calcium-dependent decrease in its step-size; and (2) the rapid calcium-dependent increase in the ADP release rate corresponds to a rapid calcium-dependent decrease in the lifetime of myo1b actin attachment. The disparity between the affinities of the steady state calcium-dependent changes in myo1b conformation and kinetics, observed in both the stopped flow and optical trap experiments, could be a demonstration of some level of decoupling of the mechanical and kinetic activities of myo1b.

3 The Three-Dimensional Path of Myosin V on Actin Depends on the Length of Its Lever-arm

Author Contributions

The work on the lever arm orientation of myosin V will be submitted to the Journal of General Physiology. John Lewis, John Beausang and Yale E. Goldman designed research; John Lewis, John Beausang and Yale E. Goldman performed research; John Lewis, John Beausang and Yale E. Goldman contributed new reagents/analytic tools; John Lewis, John Beausang and Yale E. Goldman analyzed data; John Lewis, John Beausang and Yale E. Goldman wrote the paper.

3.1 Introduction

Myosin V (myoV) is an unconventional myosin that exists as a dimer in cells and is able to step processively along filaments of actin for relatively large distances (~1μm) (**28**,**29**,**30**,**31**). In its role as a cargo transporter in the cell, it is required it to travel through a cytoplasm that is densely packed (**27**). How myoV is able to navigate through such a complex environment has been the subject of a number of studies, including a focus on dissecting the basic stepping mechanism of individual myoV motors on isolated actin filaments *in vitro* using single molecule techniques (**35**, **33**,**87**,**88**).

MyoV, as with other members of the myosin family, binds in a fixed orientation to filamentous actin (F-actin) through its N-terminal motor domain. At the C-terminal end of the motor domain is the light-chain binding domain (LCBD, A.K.A. the lever-arm), which is defined by 6 calmodulin (CaM) binding IQ motifs each bound to a CaM or CaM-like subunit. With each turnover of ATP, this domain undergoes a large conformational change directed along the length of the actin that is responsible for myosin's force production, a concept known as the swinging lever arm hypothesis (**17**). The LCBD has been found to have additional degrees of freedom, giving the myosin conformational flexibility (**89**). Since F-actin forms a two-stranded right-handed helix, there is a potential for myoV to take off-axis steps that would require this level of flexibility. Electron microscopic images of myoV frozen during processive motility along F-actin indicates that myoV, bound by both heads to the filament, predominantly spans 13 actin subunits, with smaller subpopulations spanning 11 and 15 subunits (**30**). The distance between 13 actin subunits represents the half-helical repeat of F-actin and equals ~36 nm, consistent with myoV's average 36 nm step-size (**28**). Two actin monomers 13 subunits apart also have approximately the same azimuthal orientation (**90**). Thus myoV should walk relatively straight by stepping typically 13 subunits (~36 nm) per step.

This view is supported by many single molecule experiments in which myoV walks along actin bound to a rigid glass surface, which inhibits large azimuthal changes (**87**,**88**,**33**). When myoV was observed to walk along filaments suspended away from the glass surface, though, the motors either walked straight or with a gradual left handed pitch, suggesting that the leading head of myoV lands on the 13^{th} and, sometimes, on the 11^{th} subunit from its trailing head (**35**). Twirling assays, which monitor the rotation of

actin gliding along multiple motors fixed to a surface, also found that myoV walks straight along actin or it follows a gradual, left-handed helical path (**34**).

Direct measurements of the three dimensional orientation of fluorescent rhodamine probes bifunctionally attached to a CaM (BR-CaM) bound to one of the myoV LCBDs have been made using a polarized total internal reflection microscopy (polTIRF) and defocused orientation and position imaging (DOPI). In polTIRF, several polarized light intensities are detected and ultimately converted to angles that describe the axial orientation of the probe absorption and emission dipoles relative to the long axis of actin, β_P, and the azimuthal orientation, α_P, (**Figure 3.2B**) (**33**). In DOPI, the shape of a slightly out of focus image provides the orientation of the probe (**88**). These techniques have clearly demonstrated that the LCBD switches between two distinct orientations associated with leading and trailing positions of the heads, providing strong support for the hand-over-hand stepping model (**33**). polTIRF and DOPI measurements showed relatively straight walking (**33**) and also some sudden sideways tilts (**91**).

In the simple case where the probe is aligned along the length of the lever arm, the probe angles (β_P and α_P) measured during the stepping of myoV would exactly equal the corresponding lever angles (β_L and α_L). When this is not the case, the changes in the probe angles can be substantially different from the corresponding changes in the lever-arm angles (**Figure 3.2C**). The magnitude of this difference strongly depends on how the fluorescent probe is oriented relative to the lever-arm, conventionally termed the local probe orientation, θ_P and φ_P (**Figure 3.2C**). Therefore, in order to describe the angular changes the lever arm undergoes during processive stepping, it is necessary to determine this local probe orientation and to compare it with expectations of structural models. To

that end, we developed an analytical method that provides an estimate of θ_P and φ_P from the values of β_P and α_P calculated from the measured polarized light intensities obtained from a series of processive runs of labeled myoVs. These parameters are then used to quantify the orientation of the LCBD itself (angles α_L, β_L) using equations for α_L and β_L expressed as functions of θ_P, φ_P, α_P, and β_P.

The step-size of myoV when stepping along actin has been demonstrated to be directly dependent on the length of its LCBD. Dimeric constructs with truncated lever arms have decreased step-size (**48**,**49**). We first postulated that myoV, with its native-length LCBD, likely takes many straight steps along actin because its average step-size matches the 36 nm half-helical repeat of actin. If this is true, then the truncation of the myoV lever arm, which causes reduction in the native step-size, should therefore cause it to take a smaller proportion of straight steps in its processive runs along actin. Since the effective length of the lever-arm is determined by the number of CaMs bound to the LCBD (**10**), this idea was tested by comparing the orientation of BR-CaM labeled myoV with either 4 or 6 IQ motifs. PolTIRF data was transformed into the frame of the LCBD, enabling us to determine the changes in α_L and β_L with altered lever-arm length. The truncated construct, indeed, walked much less straight along actin, wobbling from side to side as it progressed. We also determined the influence of the lever arm length on the axial rotation of a twirling actin filament translocated by multiple myosins in a gliding assay.

3.2 Materials and Methods

3.2.1 Preparation of Proteins

G-actin was obtained from rabbit skeletal muscle and purified as described previously (**92**). Biotinylated, Alexa 647-labeled F-actin was prepared from G-actin, Alexa-647 actin (Molecular Probes, Carlsbad, CA), and biotin-actin (Cytoskeleton, Denver, CO) at 1 μM total actin monomer concentration with a ratio of 5:1:1 of G-actin: Alexa-647: biotin and stabilized with 1.1 μM phalloidin (Molecular Probes, Carlsbad, CA). 0.3% rhodamine-labeled F-actin was prepared from 6′-IATR rhodamine-actin (**93**) and stabilized with 1.1 μM phalloidin. The myoV-6IQ and myoV-4IQ Myosin V constructs, both of which are truncated myosin V with 6 or 4 IQ motifs in their lever arm domains, respectively (**Figure 3.2A**), were obtained from the Sweeney lab. These constructs both have a FLAG affinity tag for purification.

Residues Pro66 and Ala73 of chicken calmodulin (CaM) were mutated to cysteine and labeled with bifunctional rhodamine (BR-I_2) as described by (**33**) BR-I_2 was a generous gift from Dr. J.E.T. Corrie (**94**). Myosin V was labeled by exchanging endogenous CaM with exogenous BR-I_2-labeled mutant CaM at low stoichiometry.

3.2.2 Buffers

M5 buffer (pH = 7.6) contains 25 mM KCl, 20 mM HEPES, 2 mM $MgCl_2$, and 1 mM EGTA in deionized water. $M5^+$ buffer is M5 plus 10 mM dithiothreitol (DTT) and 100 μg/ml wild-type CaM (WT-CaM, expressed in bacteria as described previously (**95**)).

The motility buffer for single-molecule motility assays is M5^{+} buffer plus 4 μM ATP. The motility buffer for actin twirling assays is M5^{+} buffer plus 100 μM ATP, 10 mM phosphocreatine (Sigma P-7936), 0.3 mg/ml creatine phosphokinase (prepared daily from powder, Sigma C3755), and 50 mM DTT.

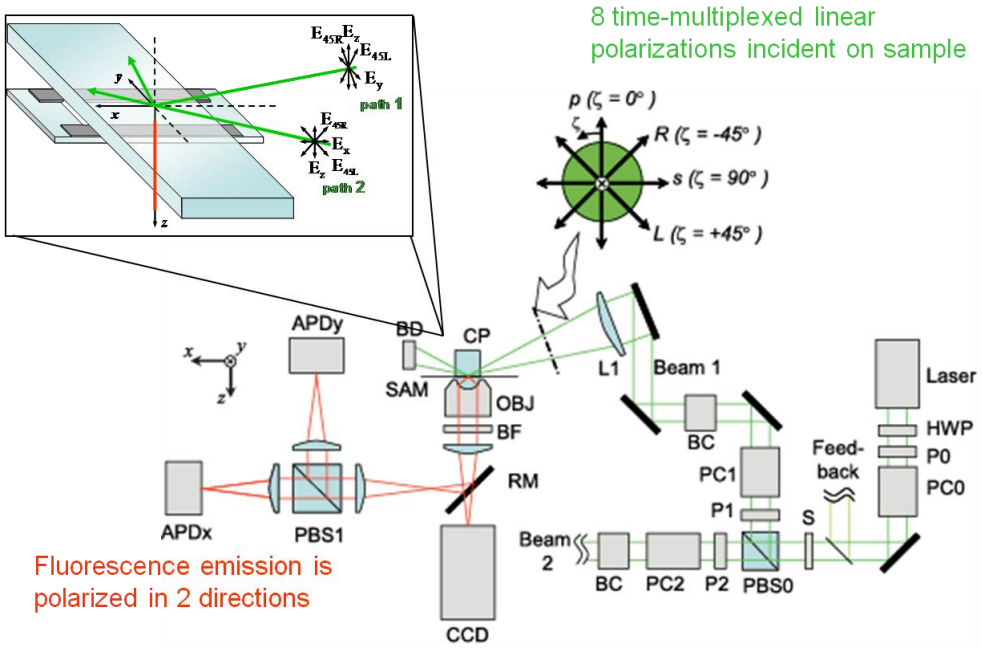

Figure 3.1 - *Experimental Setup for polTIRF Microscopy.*

The Laser is initially split by a Polarized Beam Splitter (PBS0) into Beam 1 and 2.

3.2.3 Experimental Apparatus

In the single-molecule polTIRF setup described previously (**96**), time multiplexing between two incident paths, each polarized s or p relative to the scattering plane, resulted in ambiguity of the deduced orientations outside one-eighth of a sphere. These symmetries are broken by adding time-multiplexed 45° and -45° polarizations in each of the incident directions (**34**). Eight combinations of time-multiplexed incident directions and polarizations and two simultaneously recorded emission intensities are

accumulated in each 80 ms interval, giving 16 different polarized fluorescence intensity traces (see **Figure 3.1** for schematic of relevant experimental apparatus). This arrangement allows unambiguous three-dimensional resolution of individual probe dipoles within a hemisphere. Another arrangement was used that excludes the -45° polarization gives a total of 12 channels of intensity, which gives unambiguous resolution of the probe dipole within a quarter-sphere. With the current setup, the average orientation of the probe during each 80 ms detection cycle is resolved to within ~10°. Procedures for calibration and data collection can be found in (**96**,**97**).

Data was collected using either 12 or 16 channels of polarized light intensity (**Figure 3.1** and **Figure 3.6**). Using the method described before (**33**, **34**, **97**), we calculated the orientation of the probe using these measured intensities. The initial calculation of the probe orientation is done in the lab frame, defined by the x_{lab}, y_{lab} and z_{lab}-axes; path 1 of the laser lies in the x_{lab}-z_{lab} plane, path 2 of the laser lies in the y_{lab}-z_{lab} plane, where the z_{lab}-axis is parallel to the optical axis pointing down (**Figure 3.1** and **Table 3.5**). The orientation of the probe is measured in this frame in terms of the polar coordinates θ_{lab} and φ_{lab} (**Table 3.5**).

For consistency of interpretation, we transformed the orientation of the probe from the lab frame to the actin frame of reference (see **Figure 3.2B** and **Table 3.5**). The z_A-axis for this frame is aligned along the length of the actin filament, where the positive z_A-axis points in the direction of myoV motion. The x_A-axis is perpendicular to the z_A-axis and is parallel to the surface of the flow cell, and the y_A-axis perpendicular to both of these. The orientation of the probe in the actin frame is described by $\Omega_P \equiv \{\beta_P, \alpha_P\}$ (**Table 3.5**). β_P is the axial angle measured from the z_A-axis to the probe. α_P is described as the

azimuthal angle for the probe; this angles is measured counterclockwise (when facing the $+z_A$-axis) from the x_A-axis to the projections of the probe onto the x_A-y_A plane (**Figure 3.2B** and **Table 3.5**). Because of the dipole symmetry, the probe also has an equivalent orientation of $\widetilde{\Omega}_P \equiv \{180 - \beta_P, \alpha_P \pm 180\}$. These two equivalent orientations are enough to completely describe the probe angles measured from the 16 channel data. Probe angles ($\Omega_{P,12}$) from the 12-channel data have an addition two-fold degeneracy in their measured orientation. To reduce the number of possible orientations to contend with, the symmetrically equivalent orientation for $\Omega_{P,12}$ that is most consistent with the 16 channel data was chosen.

F-actin is flowed into the experimental chamber in the direction of the x_{lab}-axis. We can unambiguously transform the x_{lab}-axis into the z_A-axis by measuring the angle and direction of myoV motion relative to the x_{lab}-axis. These measurements were done with a CCD camera, which takes two sequential images of the targeted particle just prior to photon collection with the avalanche photodiodes. The direction and angle of myoV motion relative to the lab frame were then calculated from these images.

3.2.4 Single-Molecule Motility Assay

A pre-cleaned fused silica slide (Quartz Scientific) was freshly treated in an ion plasma cleaner for 5 min and spin coated with 2 mg/ml polymethyl methacrylate (PMMA) (Aldrich Chemical, 37,003-7) in methylene chloride. The PMMA-coated slide was assembled into a 10–20 μL flow chamber with a glass coverslip and double-sided adhesive tape. Actin was adhered to the surface and flow aligned with the microscope x

axis by successive incubations with 1 mg/ml biotinylated BSA (Sigma, A-8549), 0.5 mg/ml streptavidin (Sigma, S-4762), and 100 nM biotinylated and Alexa 647-labeled F-actin, each followed by washes with $M5^+$ buffer. Myosin V, containing BR-labeled CaM, was introduced into the sample chamber at 10–1000 pM in $M5^+$ and ATP as indicated.

3.2.5 Data Selection for single molecule motility assays

There were three main criteria for including a given data trace in the main data set. The first of these was whether the observed particle was in motion just before data acquisition. This was determined from the two images taken before data collection (see Section 3.2.3). The second criterion involved the unprocessed intensities originally collected by the photodiodes. These were required to demonstrate a rise and fall in at least some of the intensity channels that correspond to the transitions in the probe orientation. Similarly, there also had to be clear transitions in the α_P and β_P that corresponded to the intensity changes. The final requirement was that there needed to be at least three separate stable states for the α_P and β_P angles. The analysis that transforms probe angles to lever angles requires a minimum of three stable angular states (see Section 3.2.7).

3.2.6 Actin Twirling Assay

A flow chamber was assembled as above by using a glass coverslip and a poly-L-lysine coated glass slide. 0.2 mg/ml anti-FLAG antibody (Sigma) was added for 1

minute. Twenty microliters of $\sim$0.2 mg/ml unlabeled myosin V with the FLAG affinity tag on its C-terminus was introduced into the sample chamber and incubated for 8 min. Exposed poly-L-lysine and fused silica were blocked by 2 × 20 μL washes with 5 mg/ml BSA. 2 × 20 μL of presheared, unlabeled F-actin was added in the absence of ATP to block any inactive myosin heads, and excess actin was removed by addition of $M5^+$ buffer at 2 mM ATP, followed by two washes of $M5^+$ without ATP. Actin filaments, sparsely (0.3%) labeled with rhodamine, were added in $M5^+$ buffer, and then motility buffer was added to initiate filament gliding and polTIRF measurements were made of the rhodamine orientation.

3.2.7 Theory and analysis for transforming probe angles to lever angles

Model of myosin V used in the analysis

The model of myosin V used in our analysis considers it as a dimer with two motor domains and lever-arms, but no tail. The principal degree of freedom is of the lever-arm relative to the motor domain. Because the motor domain stereo-specifically binds to the actin filament in a single orientation, the orientation of the lever-arm changes relative to the actin filament as well. The orientation of the lever-arm relative to the actin frame is therefore the relevant measurement for measuring the change in conformation that occurs with each step of myosin V. This orientation is defined in the actin frame as $\Omega_L \equiv \{\beta_L, \alpha_L\}$, where β_L and α_L (**Table 3.5**) are the axial and azimuthal angles and are measured the same way as the probe in the actin frame (β_P, α_P, see Section 3.2.3).

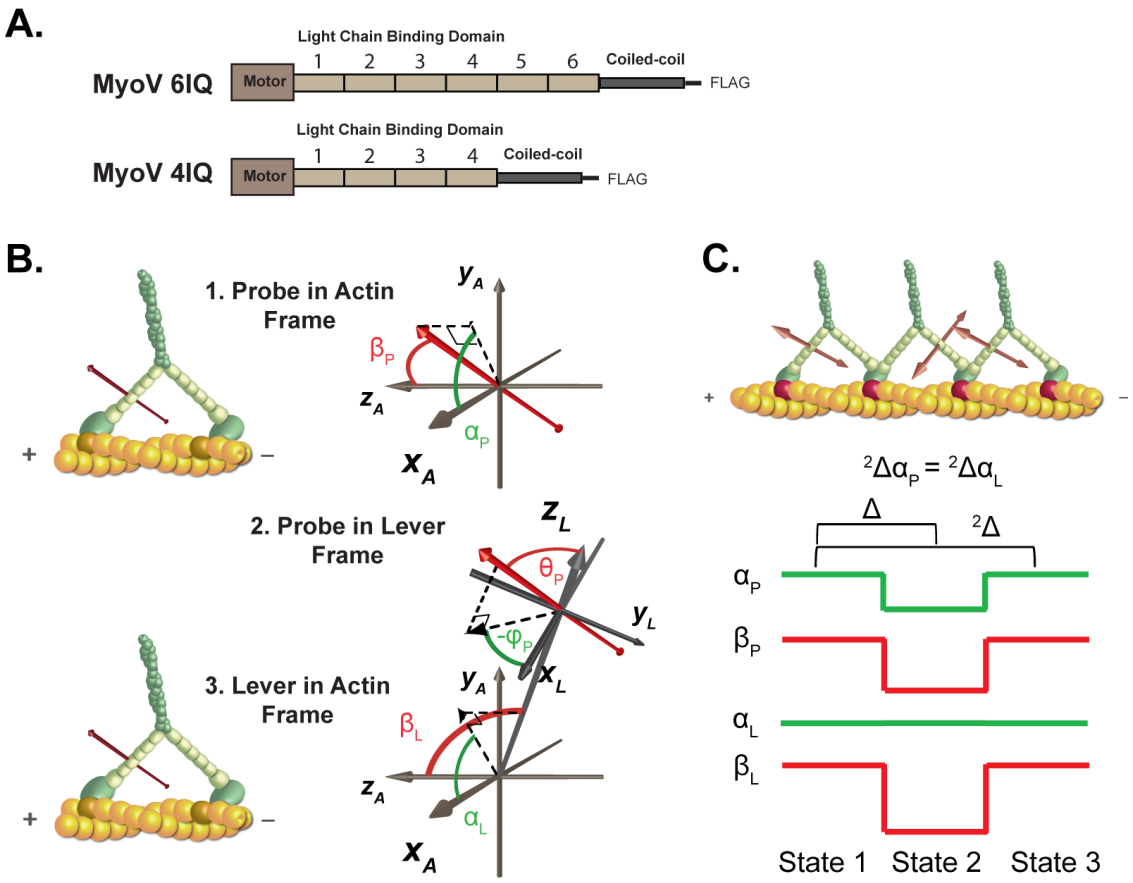

Figure 3.2 – *Myosin V Domain Map and Schematics of Relevant Frames of Reference.*

A. Domain map of the myoV-6IQ and 4IQ recombinant constructs. Both have the native myosin V motor domain and its coiled coil region, to which a FLAG tag is attached for use in the constructs' purification. They differ in the Light Chain Domain (LCBD) in which the 4IQ construct has two fewer IQ motifs than that of the 6IQ construct. **B.** Diagrams that show the orientation of the vector representing the rhodamine probe in the Actin Frame (**1**) and the Lever Frame (**2**), which is itself shown in the Actin Frame (**3**). **C.** Description of $^2\Delta\alpha$ - The changes in α_P and α_L over two steps are referred to as $^2\Delta\alpha_P$ and $^2\Delta\alpha_L$, respectively. When walking straight, the orientation of the probe attached to the myoV lever arm returns to its original position every two steps, so that both $^2\Delta\alpha_P$ and $^2\Delta\alpha_L$ equal zero and $^2\Delta\alpha_P = {}^2\Delta\alpha_L$. It can be shown that this is a general relationship so long as β_P switches regularly between two states (see Section 5.4.4).

The orientation of the probe can also be described relative to the lever-arm frame of reference, also known as the local reference frame. This frame of reference is defined

with the z_L-axis oriented along the length of the lever arm towards the C-terminus of myoV. The y_L-axis is defined as being perpendicular to the plane described by the z_L-axis (the lever-arm) and the N-terminus of the motor domain (**Figure 3.2B** and **Table 3.5**). This definition assumes that the rotation of the lever-arm along its long axis (the γ-angle, see **89**) is constant. The x_L-axis is then defined as being perpendicular to both the y_L- and z_L-axes. The orientation of the probe relative to the lever-arm is described by the polar angles θ_P and φ_P; θ_P is measured from the z_L-axis to the probe, while φ_P is measured counterclockwise (when facing the $+z_L$-axis) from the x_L-axis to the projection of the probe in x_L-y_L axes (**Figure 3.2B** and **Table 3.5**).

Values for θ_P and φ_P depend on the orientation of the probe bound to the calmodulin (CaM), which in turn is bound to the myoV lever-arm (see Section 3.2.1). The probe is rigidly bound to the CaM, so we assume that the values for θ_P and φ_P are constant for each step myoV takes along actin. There are crystal structures of myosin V with portions of the lever arm, as well as molecular models based on crystal structures that include more of the lever arm, from which one could calculate θ_P and φ_P (**98**, **99**,**100**,**101**). However, these values of θ_P and φ_P are not reliable since there are 6 unique binding sites for CaM in the native myosin V, with no direct way to determine which site is labeled for any given myosin V.

Each myosin V head switches regularly between a "leading" and "trailing" position in what is known as the "hand-over-hand" mechanism of stepping along actin (**32**). This mechanism also describes the lever-arm switching from a leading to a trailing conformation as myoV steps (**Figure 3.2C**). One of the predictions of this model was that the β_P angles (and by extension, the β_L angles) would switch between two angular states

as the lever arm transitions back and forth between the leading and trailing conformations. This view is supported by several polTIRF experiments that have clearly demonstrated myosin V switching between two angular states of β_P (**88**,**33**,**91**).

Our model for a stepping myosin V incorporates the switching between two discrete angular states of β_P as myoV takes N steps along actin (see **Figure 3.2C**). On the other hand, no assumptions are made in regards to discrete angular states existing for α_P. The N angular states of α_P (and by extension α_L) that myoV visits depends on (1) the orientation of the actin subunit relative to the actin frame to which myoV initially binds; and (2) what azimuthal changes myoV makes as it steps along actin. Because of these two factors determining the measured value of α_P, factor (1) in particular because of its largely stochastic nature, there are not expected to be discrete angular states for α_P.

Treatment of degeneracy of probe orientation for myosin V undergoing multiple β_P transitions

When using 16 channels of polarized intensity, the solution of the probe's orientation $\Omega_P \equiv \{\beta_P, \alpha_P\}$ is limited to a hemisphere of space which we define as $-180° \leq \alpha_P \leq 180°$ and $0° \leq \beta_P \leq 90°$. Because of the symmetry of the dipole ($\widetilde{\Omega}_P \equiv \{180 - \beta_P, \alpha_P \pm 180\}$, see Section 3.2.3), there is an equivalent orientation in the hemisphere from $90° \leq \beta_P \leq 180°$ (**102**). As mentioned in the last section, β_P regularly switches between two angular states as myoV takes N steps along actin. These two states, along with the two-fold dipole symmetry, lead to four equivalent expressions for the N measured orientations of the probe. We express these four equivalent orientations as N-1 pairs consisting of two

sequential angular states: ($\Omega_{P,n}$, $\Omega_{P,n+1}$), ($\Omega_{P,n}$, $\widetilde{\Omega}_{P,n+1}$), ($\widetilde{\Omega}_{P,n}$, $\Omega_{P,n+1}$), ($\widetilde{\Omega}_{P,n}$, $\widetilde{\Omega}_{P,n+1}$), where n is defined as n = 1, 2, …, N-1 and Ω_P, $\widetilde{\Omega}_{P,n}$ are defined above. For both the 12 and 16 channel data we report the solution set of the probe orientation that lies in the hemisphere defined by $0° < \beta_P < 90°$ and $-180° < \alpha_P < 180°$ for all β_P and α_P over all runs (**Figure 3.7** and **Figure 3.8**).

The change in α_P after two steps of myoV equals the corresponding change in α_L ($^2\Delta\alpha_P = {}^2\Delta\alpha_L$)

Figure 3.2C gives a schematic of a labeled molecule of myoV stepping straight along actin, demonstrating that the orientation of the probe relative to the actin returns to its original position after it takes two steps along the actin. In this simple case, it is clear that the change in the alpha probe and lever over two steps (as expressed by $^2\Delta\alpha_P$ and $^2\Delta\alpha_L$, respectively) both equal zero. This equality, as expressed in the relation $^2\Delta\alpha_P = {}^2\Delta\alpha_L$ (see Section 5.4.4 and equation 5.4.39), is a general one with the single condition that the change in β_P over two steps must be equal (or near) to zero ($^2\Delta\beta_P = 0$). This condition, as well as the $^2\Delta\alpha_P$ equality itself, is a direct consequence of the hand-over-hand mechanism of myoV stepping that accounts for the switching of β_P between two states, as discussed above.

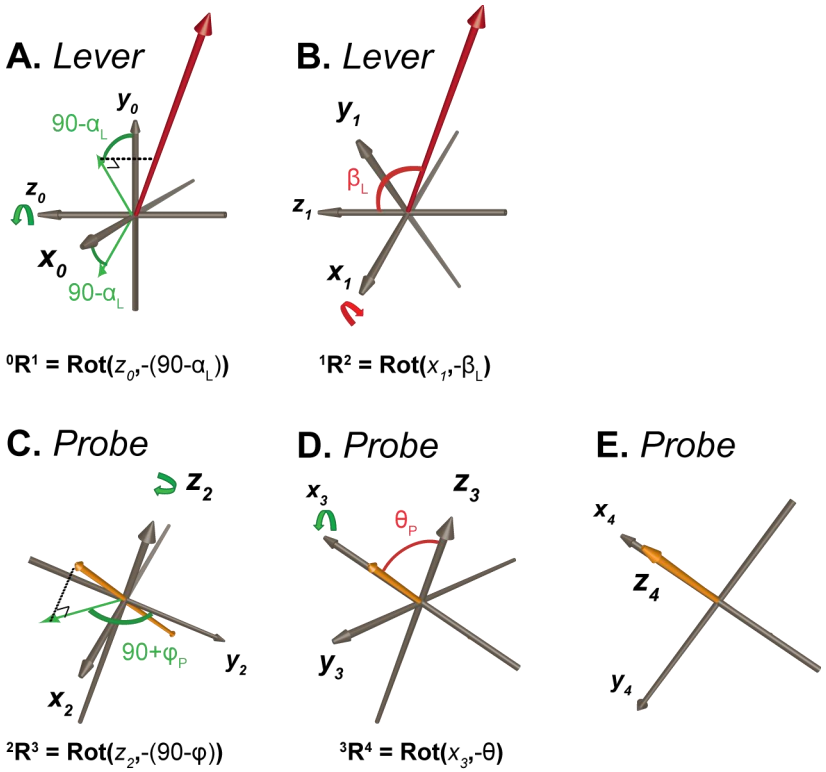

Figure 3.3 – *Rotation Scheme.*

A. *Lever in actin frame*: Counterclockwise rotation of x_0-y_0 plane about the z_0-axis by (90-α) degrees. **B.** *Lever in actin frame*: Counterclockwise rotation of y_1-z_1 plane about the x_1-axis by β degrees. C**.** *Probe in lever frame*: Counterclockwise rotation of x_2-y_2 plane about the z_2-axis by (90-ϕ) degrees. **D.** *Probe in lever frame*: Counterclockwise rotation of y_3-z_3 plane about the x_3-axis by θ degrees. **E.** *Probe in Probe frame*: Probe is now oriented with the z_4-axis of the Probe frame of reference.

Transforming the probe angles to lever angles

In order to directly transform the probe's orientation relative to actin (α_P, β_P) into its corresponding lever orientation (α_L, β_L), the orientation of the probe relative to the lever arm (θ_P, φ_P) has to be determined (see **Figure 3.2C** and Sections 5.4.1 and 5.4.2). Through a series of rotation operations that aligns the actin frame to the probe frame (**Figure 3.3**), we were able to derive equations describing α_P and β_P as functions of α_L, β_L, θ_P and φ_P (see Section 5.4.1 for derivation):

$$\beta_P(\theta_P, \varphi_P, \beta_L) = \text{acos}(-\sin\beta_L \cdot \sin\theta_P \cdot \sin\varphi_P + \cos\beta_L \cdot \cos\theta_P)$$

3.2.1

$$\alpha_P(\theta_P, \varphi_P, \alpha_L, \beta_L) = \text{atan2}([(\sin\alpha_L \cdot \cos\varphi_P + \cos\alpha_L \cdot \cos\beta_L \cdot \sin\varphi_P) \cdot \sin\theta_P + \cos\alpha_L \cdot \sin\beta_L \cdot \cos\theta_P],\ [(-\cos\alpha_L \cdot \cos\varphi_P + \sin\alpha_L \cdot \cos\beta_L \cdot \sin\varphi_P) \cdot \sin\theta_P + \sin\alpha_L \cdot \sin\beta_L \cdot \cos\theta_P])$$

3.2.2

where the atan2(x,y) function is similar to the standard arctan(y/x) function except that atan2(x,y) is single valued over a larger range ($-\pi \leq \alpha_P \leq \pi$ for atan2(x,y) and $-{}^{\pi}/_{2} \leq \alpha_P \leq {}^{\pi}/_{2}$ for arctan(y/x)).

Based on equations 3.2.1 and 3.2.2, we were able to derive expressions for α_L and β_L as functions of α_P, β_P, θ_P and φ_P (see Section 5.4.2 for derivation):

$$\beta_L(\theta_P, \varphi_P, \beta_P) = \text{acos}\left(\frac{\cos\theta_P \cdot \cos\beta_P \pm \sqrt{\sin\theta_P{}^2 \cdot \sin\varphi_P{}^2 \cdot (\sin\beta_P{}^2 - \sin\theta_P{}^2 \cdot \cos\varphi_P{}^2)}}{\cos\theta_P{}^2 + \sin\theta_P{}^2 \cdot \sin\varphi_P{}^2}\right)$$

3.2.3

$$\alpha_L(\theta_P, \varphi_P, \alpha_P, \beta_P)$$
$$= \operatorname{atan2}\Big(\Big[\big(\cos\big(\beta_L(\theta_P, \varphi_P, \beta_P)\big) \cdot \sin\varphi_P \cdot \sin\theta_P + \sin\big(\beta_L(\theta_P, \varphi_P, \beta_P)\big) \cdot \cos\theta_P\big) \cdot \cos\alpha_P - \sin\theta_P \cdot \cos\varphi_P \cdot \sin\alpha_P\Big],$$
$$\Big[\big(\cos\big(\beta_L(\theta_P, \varphi_P, \beta_P)\big) \cdot \sin\varphi_P \cdot \sin\theta_P + \sin\big(\beta_L(\theta_P, \varphi_P, \beta_P)\big) \cdot \cos\theta_P\big) \cdot \sin\alpha_P \cdot \cos\varphi_P + \sin\theta_P \cdot \cos\varphi_P \cdot \cos\alpha_P\Big]\Big)$$

3.2.4

From equations 3.2.3 and 3.2.4, it is clear that calculating α_L and β_L from the measured values of α_P and β_P hinges on finding reliable values of θ_P and φ_P for each observed myosin V.

Our strategy for calculating θ_P and φ_P lay in finding estimates for the expressions $\Delta\alpha_{L,n} = \alpha_{L,n} - \alpha_{L,n+1}$ and $\Sigma\beta_{L,n} = \beta_{L,n} + \beta_{L,n+1}$ to use in the following system of equations derived from the α_L and β_L equations (equations 3.2.3 and 3.2.4):

$$\alpha_L\big(\theta_P, \varphi_P, \alpha_{P,n}, \beta_{P,n}\big) - \alpha_L\big(\theta_P, \varphi_P, \alpha_{P,n+1}, \beta_{P,n+1}\big) = \Delta\alpha_{L,n}$$

3.2.5

$$\beta_L\big(\theta_P, \varphi_P, \beta_{P,n}\big) + \beta_L\big(\theta_P, \varphi_P, \beta_{P,n+1}\big) = \Sigma\beta_{L,n}$$

3.2.6

where n is defined over the range:

$$n = 1, 2 \ldots N - 1$$

and N is the total number of angular states in a single processive run of myoV (these equations are discussed in full in Sections 5.4.4 - 5.4.6). With the measured values for α_P

and β_P, and our assumption that θ_P and φ_P are constant over every state in *n*, we have a system of two equations (3.2.5 and 3.2.6) and four unknown parameters, θ_P, φ_P, $\Delta\alpha_L$ and $\Sigma\beta_L$. Obtaining reliable estimates for $\Delta\alpha_{L,n}$ and $\Sigma\beta_{L,n}$ for all n would reduce the problem to a system of two equations and two unknowns, allowing us to calculate a unique solution for θ_P and φ_P. An estimate for the N-1 values of $\Delta\alpha_L$ in a single run of myoV is obtained by combining the equality ${}^2\Delta\alpha_P = {}^2\Delta\alpha_L$ with ${}^2\Delta_n = \Delta_n + \Delta_{n+1}$ (see equation 5.4.42 in Section 5.4.4):

$$\Delta\alpha_{P,n} + \Delta\alpha_{P,n+1} = \Delta\alpha_{L,n} + \Delta\alpha_{L,n+1}$$

3.2.7

which is then re-arranged to give the definition for *R*, which is constant over all n:

$$\Delta\alpha_{P,0} - \Delta\alpha_{L,0} = \Delta\alpha_{P,1} - \Delta\alpha_{L,1} = \cdots = \Delta\alpha_{P,n} - \Delta\alpha_{L,n} = \cdots = \Delta\alpha_{L,N-1} - \Delta\alpha_{P,N-1} \equiv R$$

3.2.8

This allows us to express $\Delta\alpha_{P,n}$ as the sum of $\Delta\alpha_{L,n}$ and *R*:

$$\Delta\alpha_{P,n} = (-1)^n \cdot R + \Delta\alpha_{L,n}$$

3.2.9

Using this equation, every N-1 value for $\Delta\alpha_L$ can be calculated from $\Delta\alpha_P$ if a reliable value for the constant *R* can be found. This value for R is obtained by calculating the average for $\Delta\alpha_P$ over all n. If $\Delta\alpha_L$ is constant for every step, then this average for $\Delta\alpha_P$ exactly equals R (see Section 5.4.5). $\Delta\alpha_L$ (and by extension, $\Delta\alpha_P$) is not generally

constant, so a weighted average of $\Delta\alpha_P$ ($\overline{\Delta\alpha_P}_{weighted}$) is calculated that excludes values of $\Delta\alpha_P$ that are far from the constant R:

$$\overline{\Delta\alpha_P}_{weighted} = \frac{1}{N-1} \cdot \left(\sum_{n=0}^{N-1} (-1)^n \cdot W_n \cdot \Delta\alpha_{P,n} \right) \cong R$$

3.2.10

with the following definition for the weighting function W(see Section 5.4.5 for details):

$$W_n = \frac{1}{(\left|\Delta\alpha_{P,n} - \overline{\Delta\alpha_P}\right| + \epsilon)^r}$$

3.2.11

ϵ and r are user-defined values where ϵ is chosen near zero to prevent division by 0, and r is any even value greater than zero. Given N-1 values of $\Delta\alpha_P$ measured from a myoV taking N steps along actin, we use equation 3.2.10 to calculate a close approximation to the constant R. This value for R is then applied to equation 3.2.9 to calculate the N-1 corresponding values for $\Delta\alpha_L$.

To calculate θ_P and φ_P from a myoV taking N steps along actin using equations 3.2.5 and 3.2.6, we also need to calculate N-1 values for $\Sigma\beta_L$. Unlike α_L, there is no relationship that would allow us to estimate $\Sigma\beta_L$ from the measured values of α_P and β_P. We instead assume that the lever is straight and rigid in both the leading and trailing positions, from which we can conclude that $\Sigma\beta_{L,n} = \beta_{L,n} + \beta_{L,n+1} = 180°$ for every N-1 value of $\Sigma\beta_{L,n}$.

In order to calculate θ_P, φ_P, α_L and β_L from the N values of α_P and β_P measured from the processive run of a single myoV motor taking N steps, we first obtain N-1 values of $\Delta\alpha_{L,n}$ (based on calculating R) and for $\Sigma\beta_{L,n}$ (assuming it equals 180°). From these four parameters we are able to determine the optimum values for θ_P and φ_P that satisfy equations 3.2.5 and 3.2.6. These calculated values for θ_P and φ_P, along with the N values of α_P and β_P, are in turn used to calculate N values of α_L and β_L using equations 3.2.3 and 3.2.4. This procedure was used for both myoV-6IQ and myoV-4IQ constructs.

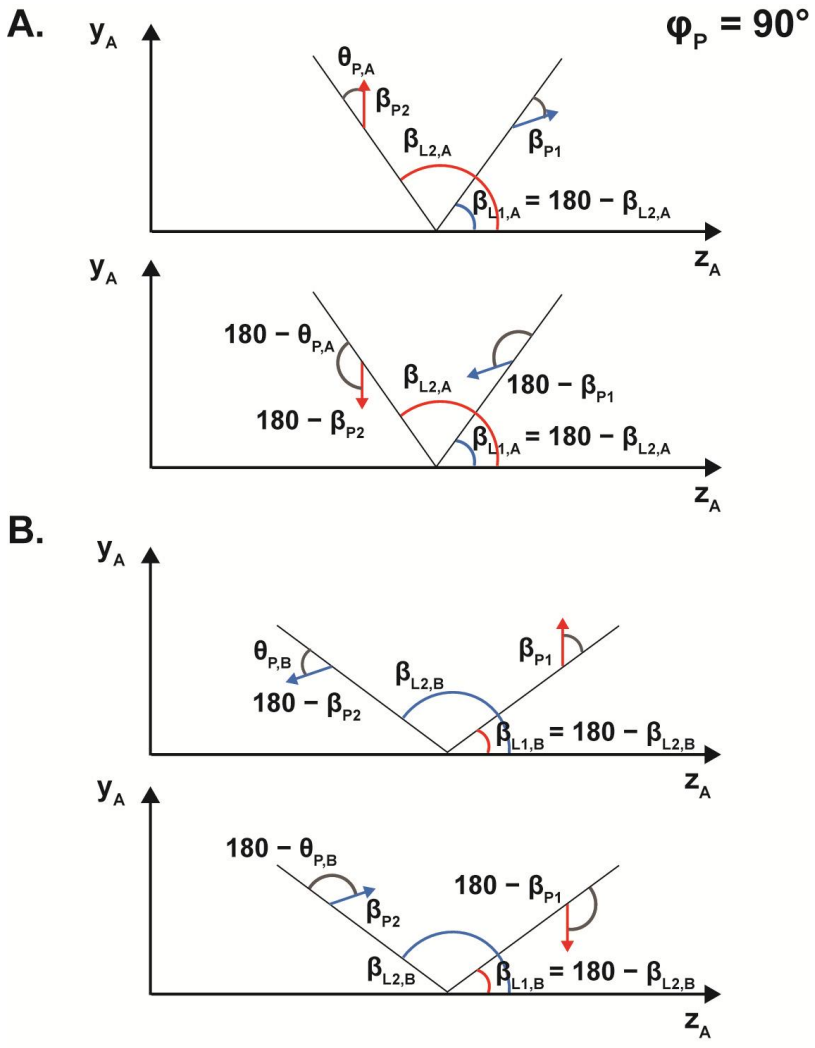

Figure 3.4 – *Schematic describing two unique lever configurations related to different β_L solutions.*

Ambiguity in the solution of the lever orientation calculated from polTIRF data

A myoV taking N steps along actin in a hand-over-hand fashion regularly switches between two β_P states (see above and **Figure 3.2C**). Because of the ambiguity of the probe's orientation arising from the symmetry in the dipole, there are four equivalent angular paths of the myoV as determined by the N angular states the probe visits in α_P and β_P. The four angular paths of the probe can be described as ($\Omega_{P,n}$, $\Omega_{P,n+1}$), ($\Omega_{P,n}$, $\widetilde{\Omega}_{P,n+1}$), ($\widetilde{\Omega}_{P,n}$, $\Omega_{P,n+1}$), ($\widetilde{\Omega}_{P,n}$, $\widetilde{\Omega}_{P,n+1}$), where n is defined as n = 1, 2, …, N-1 and $\Omega_{P,i}$ and $\widetilde{\Omega}_{P,i}$ are related by dipole symmetry (see above). These four paths of the probe can be used to calculate the four corresponding angular paths of the lever-arm, as determined by the N angular states the lever visits in α_L and β_L using equations 3.2.3 and 3.2.4.

We define the initial solution of the lever orientation in the n^{th} angular state as the solid angle $\Omega_{L,n} \equiv (\beta_{L,n}, \alpha_{L,n}) \equiv (\beta_L(\Omega_{P,n}, \theta_P, \varphi_P), \alpha_L(\Omega_{P,n}, \theta_P, \varphi_P))$ (see equations 3.2.3 and 3.2.4). The probe angle pairs ($\Omega_{P,n}$, $\Omega_{P,n+1}$) and ($\widetilde{\Omega}_{P,n}$, $\widetilde{\Omega}_{P,n+1}$) use the probe orientations (θ_P, φ_P) and (180 - θ_P, $\varphi_P \pm 180$), respectively, to calculate the same lever-arm configuration $A \equiv (\Omega^A_{L,i}, \Omega^A_{L,i\pm1})$ (see **Figure 3.4A**). There is a similar relationship between the probe angle pairs ($\Omega_{P,i}$, $\widetilde{\Omega}_{P,i\pm1}$) and ($\widetilde{\Omega}_{P,i}$, $\Omega_{P,i\pm1}$) which are both used to calculate the lever-arm configuration $B \equiv (\Omega^B_{L,i}, \Omega^B_{L,i\pm1})$ (**Figure 3.4B**). In general, there is not a simple relationship between lever-arm configurations A and B, except for the relationship between the probe angles (Ω_P and $\widetilde{\Omega}_P$) from which they are calculated (**Figure 3.4**).

There is an additional equivalent solution for the lever arm orientation that does not arise from the dipole symmetry of the probe. Given any probe solution $\Omega_{P,i}$, two

equivalent lever solutions ($\Omega_{L,i} = \widetilde{\Omega}_{L,i}$) can be calculated that satisfy equations 3.2.5 and 3.2.6, where $\Omega_{L,i}$ is described above and $\widetilde{\Omega}_{L,i} \equiv (180 - \beta_{L,i}, \alpha_{L,i} \pm 180) \equiv (\beta_L(\Omega_{P,i}, \theta_P', \varphi_P'), \alpha_L(\Omega_{P,i}, \theta_P', \varphi_P'))$ and $\theta_P' = 180 - \theta_P$, $\varphi_P' = 180 \pm \varphi_P$. These two solutions represent two lever configurations that are related by mirror symmetry, as seen in **Figure 3.5**. This 2-fold symmetry along with the four lever solutions related to the dipole symmetry give a total of eight possible solutions for the lever angles. In order to reduce the number of possible solutions, we used as a constraint the probe and lever angles (β_P, α_P, β_L, α_L, θ_P, and φ_P) calculated from a high resolution molecular model of a myosin V dimer with both heads bound to actin (**100**). This will be discussed in greater detail in the Discussion section.

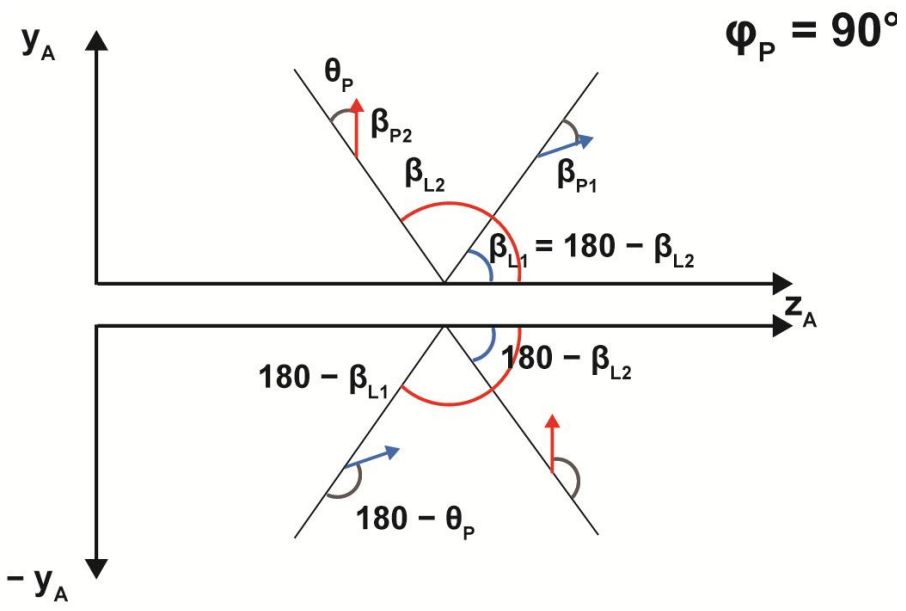

Figure 3.5 – *Principal degeneracy in lever solutions*

3.3 Results

3.3.1 Myosin V constructs myoV-6IQ and myoV-4IQ

Two recombinant constructs of chick myosin V were used in these experiments (**48**), myoV-6IQ and myoV-4IQ. Both constructs contain the native motor domain and have a coiled-coil region at the C-terminus for dimerization; the cargo-binding domain is absent in both cases (**Figure 3.2A**). MyoV-6IQ has a native length lever-arm domain made up of 6 IQ motifs, whereas myoV-4IQ has 4 IQ motifs, shortening the effective length of its lever-arm. This shortening has been shown to reduce the myoV average step-size from 36 nm to 24 nm (**48**,**49**). Single calmodulins (CaMs) bind to each IQ motif on the lever-arm of myoV. The two constructs of myoV are labeled by exchanging one of these CaMs with a CaM that has a rhodamine fluorophore bifunctionally attached (BR-CaM) such that each myoV dimer has no more than one BR-CaM (see Section 3.2.1; **33**,**94**). Throughout the paper, the myoV-6IQ and -4IQ data taken with 12 polarized fluorescence intensity channels are referred to as myoV-$6IQ_{12}$ and myoV-$4IQ_{12}$ data, while the data taken with 16 channels is referred to as myoV-$6IQ_{16}$ data.

3.3.2 3-Dimensional orientation of Myosin V during single molecule processive motility

The single molecule processive motility assay is carried out in a flow cell in which F-actin is bound to the microscope slide surface through biotin-streptavidin

linkages (see Section 3.2.4). BR-CaM labeled myoV-6IQ or myoV-4IQ is flowed in along with an activation mix, which includes 4 μM MgATP. Video sequences of BR on

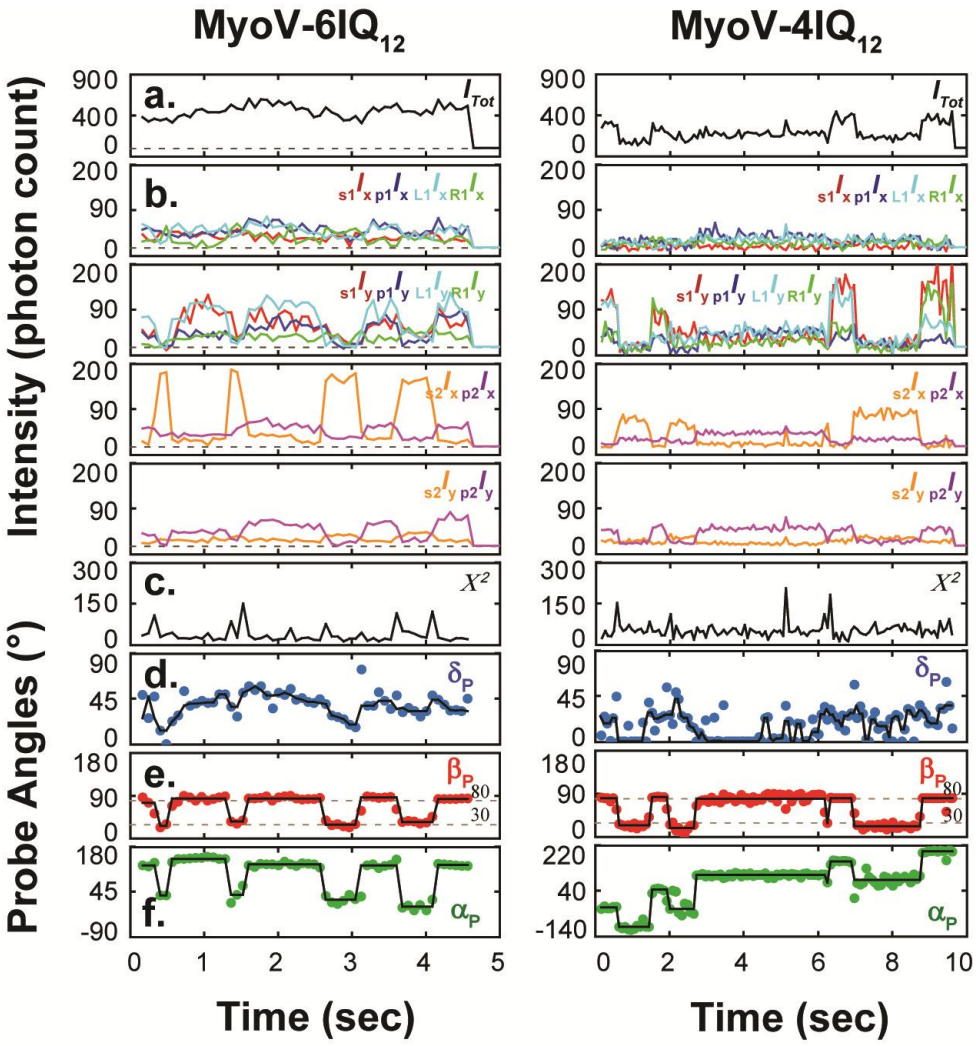

Figure 3.6 - *Representative traces from the processive runs of single motors of rhodamine-labeled myoV-6IQ$_{12}$ (left) and -4IQ$_{12}$ (right) along actin filaments.*

Panels a,b: The total measured intensity is shown (***a***), along with the 12 component intensities that make it up (***b***). The time at which the intensities drop to zero indicates when the rhodamine probe bleached. ***Panels c-f:*** Calculation of the orientation of the probe in the actin frame. ***c.*** Trace of the χ^2 demonstrating the goodness-of-fit of the measured intensities to the calculated probe angles δ_P, θ_{lab}, and ϕ_{lab}. ***d-f.*** Traces of the angles δ_P (***d***), β_P (***e***), and α_P (***f***) in the Actin Frame, which were transformed from the angles θ_{lab} and ϕ_{lab} in the Laboratory Frame (see Section 3.2.3).

single myoV molecules moving processively on the actin are recorded in several areas on the microscope slide to determine each construct's average velocity. MyoV-6IQ and -4IQ traveled at average velocities of V_{ave} = 103 ± 3 nm/s (mean ± s.e.m, n = 92) and 85 ± 3 nm/s (n = 50) respectively at 4 μM MgATP, consistent with prior findings (**103**). A typical moving molecule is selected from pairs of images recorded ~3 s apart which are also used to measure the direction of its motility. Six or eight input polarizations and two emission polarizations are used to record a set of 12 or 16 polarized fluorescence intensities (**Figure 3.1**), from which the three-dimensional orientation of the probe is calculated in the laboratory reference frame, θ_{lab} and φ_{lab} (see Section 3.2.3; **96**,**97**,**34**), with a time resolution of 80 ms. These angles are then transformed to the more biologically relevant actin frame of reference with angles β_P and α_P (see Section 3.2.3 and **Figure 3.2B**).

Representative recordings of the 12 individual polTIRF intensities and the total combined fluorescence for myoV-6IQ and -4IQ show that the individual traces are typically stable for periods of several hundred ms and then suddenly transition to new intensity levels (**Figure 3.6**, *top panels*). Complementary changes in other traces during these transitions result in the total intensity remaining relatively constant. Dwell periods with stable intensities indicate times when the probe's orientation is constant, so that the (β_P) and azimuthal (α_P) angle traces are also stable in the corresponding time periods (**Figure 3.6**, *bottom panels*). Mean values for β_P and α_P over these stable intervals were calculated for use in histograms of these angles for all measured myoV (**Figure 3.7**).

3.3.3 β_P and α_P distributions for myoV-6IQ and myoV-4IQ are similar

For individual processive runs of myoV-6IQ$_{12}$, myoV-6IQ$_{16}$ and myoV-4IQ$_{12}$, time dependent traces of β_P demonstrate regular switching between two stable angular states (**Figure 3.6**, *bottom panels*), as has been shown before for native myoV (**88**,**33**).

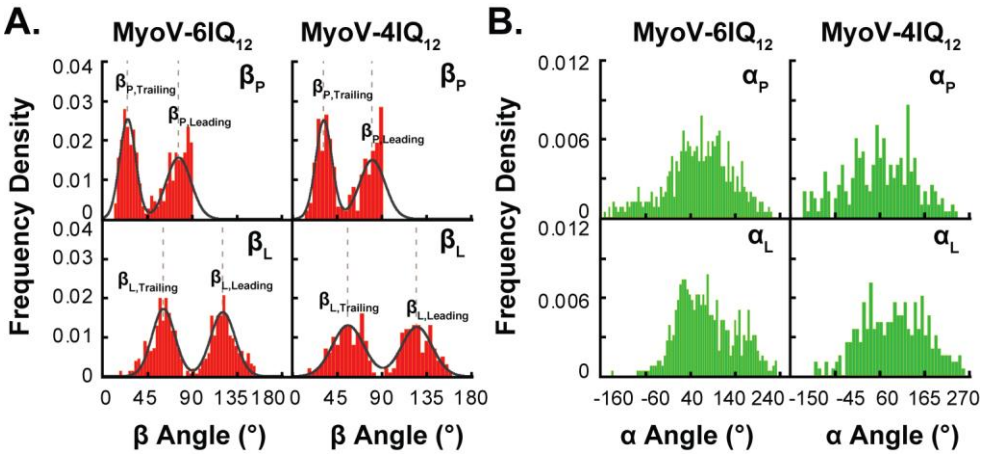

Figure 3.7 – *Distributions for β_P, β_L and α_P, α_L for myoV-6IQ$_{12}$ and -4IQ$_{12}$.*

Histograms of the β_P, β_L and α_P, α_L angles collected from the mean angular states that were visited during the individual runs of myoV-6IQ$_{12}$ (*Top*: n=73, states=515) and 4IQ$_{12}$ (*Bottom:* n=49, states=246). The beginning and end of each angular state of α_P and β_P were defined by the transitions in β_P. Histograms are normalized so that the total area of the distribution is equal to one. **A.** β_P and β_L distributions. Each of these distributions was best fit by a bimodal Gaussian equation, where the resulting parameters are shown in **Table 3.1** and **Table 3.3. B.** α_P and α_L distributions.

The peak values of these two states were determined from the distributions of β_P for all measured myoV-6IQ and myoV-4IQ motors that demonstrated processive motility (**Figure 3.7A** and **Figure 3.8A**). These distributions were well fit by bimodal Gaussian models (**Table 3.1**), where the peak β_P angles of the probe when the lever arm is in the leading and trailing positions are 76° and 25° for myoV-6IQ$_{12}$, respectively; 92° and 26° for myoV-6IQ$_{16}$; and 80° and 30° for myoV-4IQ$_{12}$. These values for β_P are similar to

	β_P Angles (deg)		
	MyoV 6IQ		MyoV 4IQ
	Quartersphere	Hemisphere	Quarter-sphere
$\beta_{Leading}$	76 ± 13 (51%)	92 ± 13 (47%)	80 ± 13 (48%)
$\beta_{Trailing}$	25 ± 8.1 (49%)	26 ± 14 (53%)	30 ± 8.3 (52%)
	$^2\Delta\beta_P$ Angles (deg)		
	MyoV 6IQ		MyoV 4IQ
	Quartersphere	Hemisphere	Quarter-sphere
$^2\Delta\beta$	−0.32 ± 7.9	−0.30 ± 11	−1.0 ± 11
	$\Delta\alpha_P$ Angles (deg)		
	MyoV 6IQ		MyoV 4IQ
	Quartersphere	Hemisphere	Quarter-sphere
$\Delta\alpha$	1.9 ± 57	−2.4 ± 85	4.3 ± 87
	$^2\Delta\alpha_P$ Angles (deg)		
	MyoV 6IQ		MyoV 4IQ
	Quartersphere	Hemisphere	Quarter-sphere
$^2\Delta\alpha_1$	−39 ± 27 (15%)	−34 ± 13 (24%)	NA
$^2\Delta\alpha_2$	1.8 ± 16 (55%)	0.32 ± 13 (51%)	9.9 ± 88 (10%)
$^2\Delta\alpha_3$	32 ± 28 (30%)	35.3 ± 22 (25%)	NA

Values result from Gaussian fits to distributions, and report peak mean ± σ.

Table 3.1 - *Analysis of the distributions of α and β angles for MyoV-6IQ and -4IQ in the Probe frame of reference*

those previously reported (**88**,**33**) when the orientational ambiguity due to the dipole symmetry is considered (see Sections 3.2.3 and 3.2.7).

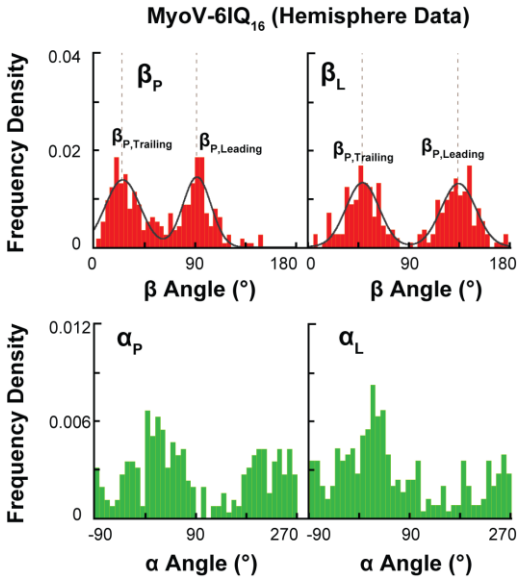

Figure 3.8 – *Distributions for α and β probe and lever for myoV 6IQ$_{16}$ with probe solution isolated to a hemisphere of space.*

α_P visits numerous stable angular states during individual runs of myoV-6IQ$_{12}$, -6IQ$_{16}$ and -4IQ$_{12}$ (**Figure 3.6**, *bottom panels*). This is likely due to the observed myosins starting their runs from different subunits of the helical actin filament (see Section 3.2.7). This randomness leads to broad distributions of α_P constructed from the total runs of the two myoV constructs with no obvious differences (**Figure 3.7B** and **Figure 3.8B**). To better understand the nature of the azimuthal paths seen in the α_P traces such as in **Figure 3.6**, independent of the starting azimuth we consider instead the change in α_P as myoV steps along actin, where the change over one step is referred to as $\Delta\alpha_P$ (**Figure 3.2C**).

If the probe were aligned along the length of the lever arm (i.e. $\theta_P = 0°$), $\Delta\alpha_P$ would equal $\Delta\alpha_L$ and would therefore be a good measure of the azimuthal motion of

myoV as it walks along actin. However, as demonstrated in Figure 3.2C, when $\theta_P \neq 0°$, $\Delta\alpha_P$ does not equal $\Delta\alpha_L$ and extracting azimuthal information about the lever-arm from the probe angles is no longer as straightforward. In fact, the $\Delta\alpha_P$ distributions for both myoV-6IQ and -4IQ, which might be expected to have quite different azimuthal paths because of their different step-sizes, are very similar (**Figure 3.9**). We instead found that in order to determine $\Delta\alpha_L$ from the orientation of the probe, we need to consider the change in α_P as after myoV takes two successive steps, referred to as $^2\Delta\alpha_P$.

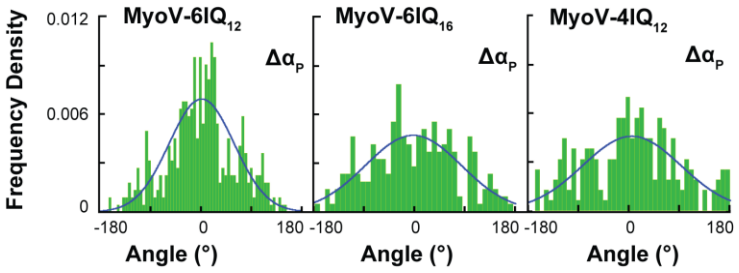

Figure 3.9 – *Distributions for $\Delta\alpha_P$ for myoV-6IQ$_{12}$, -6IQ$_{16}$ and -4IQ$_{12}$.*

Histograms of the $\Delta\alpha_P$ angles calculated from the mean angular states of a_P that were visited during the individual runs of myoV-6IQ$_{12}$ (*Left)* and myoV-6IQ$_{16}$ (*center*) and myoV-4IQ$_{12}$ (*Right*).

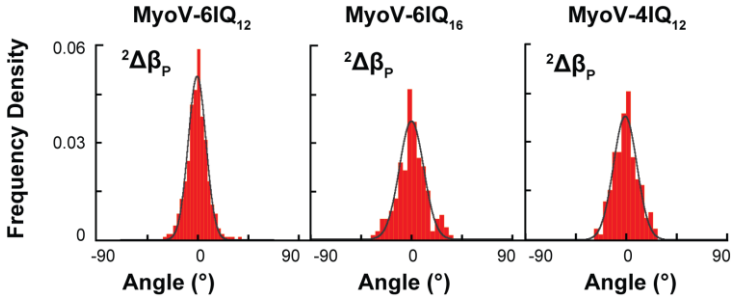

Figure 3.10 – *Distributions for $^2\Delta\beta_P$ myoV-6IQ$_{12}$, -6IQ$_{16}$ and -4IQ$_{12}$.*

Histograms of the $^2\Delta\beta_P$ angles calculated from the mean angular states of β_P that were visited during the individual runs of myoV-6IQ$_{12}$ (*Left*), myoV-6IQ$_{16}$ (*Center*) and myoV-4IQ$_{12}$ (*Left*). Histograms are normalized so that the total area of the distribution is equal to one. Each of these distributions was best fit by a Gaussian equation, where the resulting parameters are shown in **Table 3.1**.

3.3.4 $^2\Delta\alpha_P$ distributions for myoV-6IQ and myoV-4IQ

In order to relate the probe orientation to $\Delta\alpha_L$ in a way that is independent of θ_P and φ_P, we used the change in α_P over *two* steps, $^2\Delta\alpha_P$ (see **Figure 3.2C**). The relationship $^2\Delta\alpha_P = {}^2\Delta\alpha_L$ allows us to directly equate azimuthal changes in the probe (α_P) over two steps of myoV with the corresponding azimuthal changes in the lever (α_L) irrespective of the local probe angles θ_P and φ_P (see **Figure 3.2C** and Section 3.2.7). This equality is a general one with the single condition that the change in β_P over two steps must be equal (or near) to zero ($^2\Delta\beta_P = 0$) (see Section 5.4.4). The $^2\Delta\beta_P$ distributions for myoV-6IQ$_{12}$, -6IQ$_{16}$ and -4IQ$_{12}$ are narrow and centered on zero (**Figure 3.10** and **Table 3.1**),

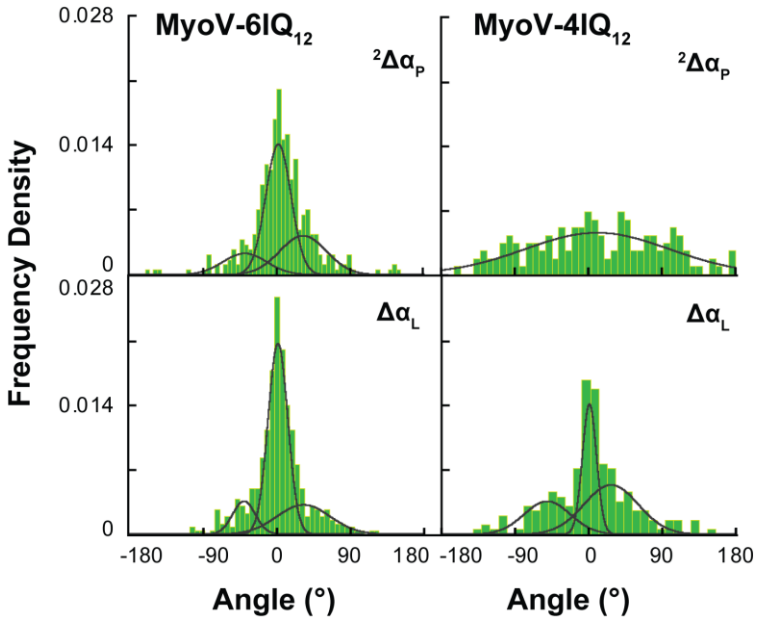

Figure 3.11 – *Distributions for $^2\Delta\alpha_P$ and $\Delta\alpha_L$ for myoV-6IQ$_{12}$ and -4IQ$_{12}$.*

Histograms of the $^2\Delta\alpha_P$ and $\Delta\alpha_L$ angles calculated from the mean angular states of α_P and α_L, respectively, that were visited during the individual runs of myoV-6IQ$_{12}$ (*Left*) and -4IQ$_{12}$ (*Right*). Histograms are normalized so that the total area of the distribution is equal to one. Each of these distributions was best fit by a trimodal Gaussian equation, where the resulting parameters are shown in **Table 3.1** and **Table 3.3.**

demonstrating that this condition is essentially satisfied in our measurements. $^2\Delta\beta_P$ equaling zero is an expected consequence of myoV stepping hand-over-hand, which causes the measured β_P angles to switch between two states (see Section 3.2.7). The $^2\Delta\alpha_P$ distribution for myoV-6IQ$_{12}$ has three apparent populations ($^2\Delta\alpha_P = -39°$, 2°, and 32°, **Figure 3.11** and **Table 3.1**). Similar populations are seen in the $^2\Delta\alpha_P$ distribution constructed for the myoV-6IQ$_{16}$ data (**Figure 3.12** and **Table 3.1**). Distinct sub-populations could not be distinguished for the $^2\Delta\alpha_P$ distribution of myoV-4IQ$_{12}$ (**Figure 3.11**), which was very broad with a fitted peak at $^2\Delta\alpha_P = 9.9$ ($\sigma = 88°$) (**Table 3.1**).

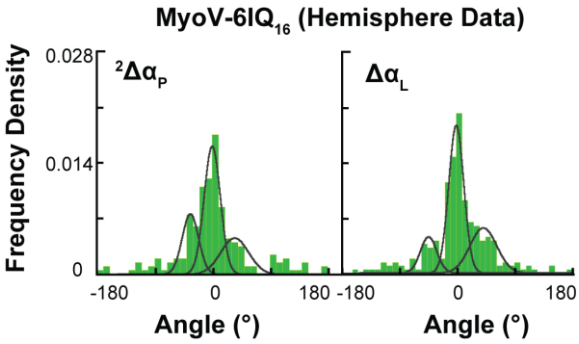

Figure 3.12 – *Distribution of $^2\Delta\alpha_P$ and $\Delta\alpha_L$ for myoV-6IQ$_{16}$ with probe solution isolated to a hemisphere of space.*

3.3.5 Multiple sub-populations in the distributions of θ_P vs. φ_P for myoV-6IQ and myoV-4IQ

θ_P and φ_P measure the orientation of the probe relative to the lever-arm frame of reference (see Section 3.2.7 and **Figure 3.2B**). From a relationship that relates the orientation of the lever arm to that of the probe (equations 3.2.1 and 3.2.2), we are able to find values for θ_P and φ_P from the measured α_P and β_P angles and estimated values for α_L and β_L (see Section 3.2.7 for full details). The estimated values for α_L arise from the

relationship $^2\Delta\alpha_P = {}^2\Delta\alpha_L$; while the values for β_L are based on the assumption that if the lever arm is rigid, then the sum of β_L in the leading and trailing positions is 180° ($\Sigma\beta_L = \beta_{L,trail} + \beta_{L,lead} = 180°$).

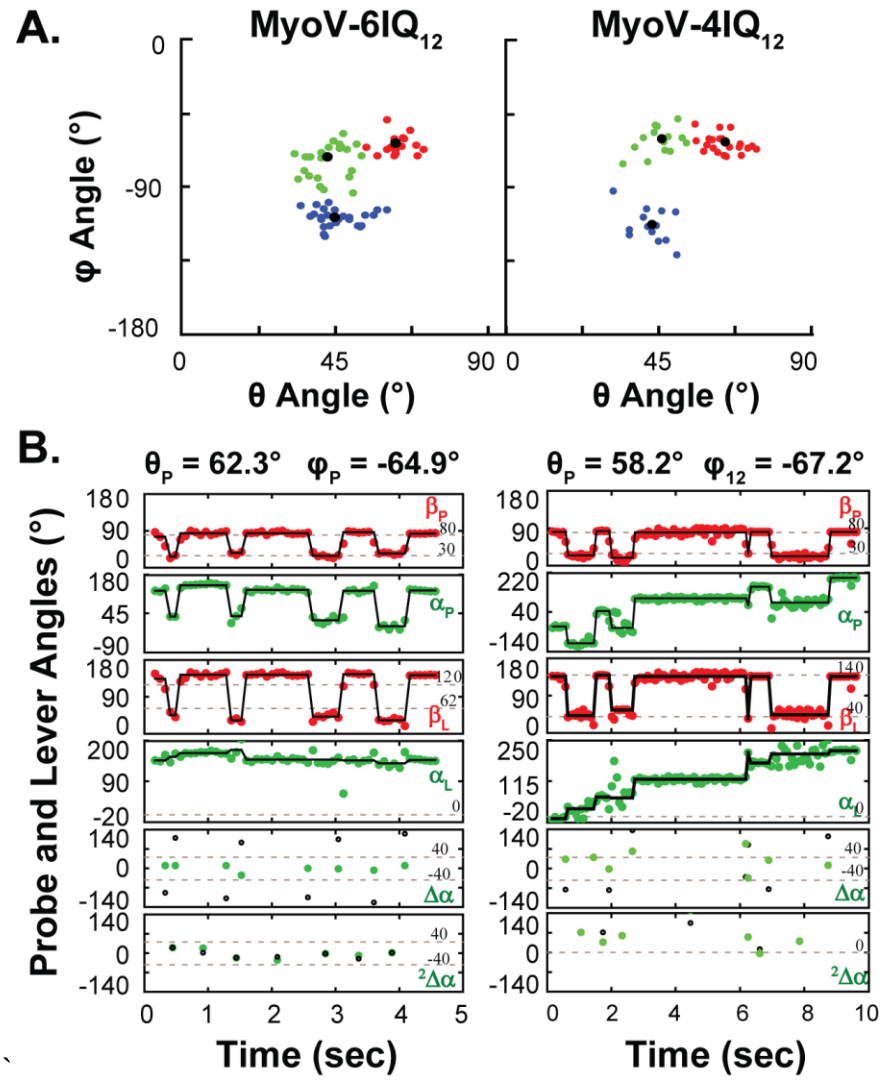

Figure 3.13 – *Distributions for θ_P vs. ϕ_P for myoV-6IQ$_{12}$ and -4IQ$_{12}$.*

A. θ_P vs. ϕ_P distributions calculated from individual processive runs of myoV-6IQ$_{12}$ (*left*, n=73) and -4IQ$_{12}$ (*right*, n=49) describing the orientation of the Probe in the Lever Frame. **B.** Representative traces of β_L and α_L, which are the angles measuring the orientation of the Lever in the Actin Frame, were calculated from the optimized θ_P and ϕ_P (6IQ: θ_P = 62°, ϕ_P = -65°; 4IQ: θ_P = 42°, ϕ_P = -124°) and from the β_P and α_P traces shown in **Figure 3.6**. Also shown are the calculated $\Delta\alpha$ and $^2\Delta\alpha$ values (○ = probe angles, ● = lever angles, see **Figure 3.2C** for definition).

Scatter plots of θ_P vs. φ_P calculated from individual runs of myoV-6IQ$_{12}$, myoV-6IQ$_{16}$ and myoV-4IQ$_{12}$ are shown in **Figure 3.13A** and **Figure 3.14**. The distributions for myoV-6IQ$_{12}$ and myoV-6IQ$_{16}$ have three fairly distinct populations, each of which were separately binned into 2-D histograms and fit by a two-dimensional Gaussian function: θ_1 = 45° and φ_1 = -110°; θ_2 = 43° and φ_2 = -73°; θ_3 = 63° and φ_3 = -65° (**Table 3.2**). The distribution for myoV-4IQ$_{12}$ was strikingly similar to that of myoV-6IQ, also demonstrating three populations with similar parameters when fit by a 2-D Gaussian function: θ_1 = 43° and φ_1 = -113°; θ_2 = 46° and φ_2 = -60°; θ_3 = 65° and φ_3 = -62° **(Table 3.2**).

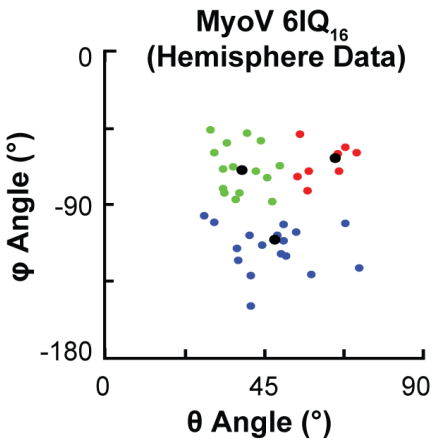

Figure 3.14 – *Plot of θ_P vs. ϕ_P for myoV-6IQ$_{16}$.*

α_L and β_L give the orientation of the lever arm relative to the actin frame of reference (see Section 3.2.7 and **Figure 3.2B**). Using the calculated values for θ_P and φ_P and equations 3.2.3 and 3.2.4, we were able to directly calculate the values for α_L and β_L from the measured values of α_P and β_P for each observed myoV-6IQ$_{12}$ (n=73), myoV-6IQ$_{16}$ (n=42) and myoV-4IQ$_{12}$ (n=49) (see **Figure 3.13B** for representative traces). Distributions of α_L for both constructs show that the range lies roughly between 0° and

	MyoV 6IQ$_{12}$ (Quartersphere)		
	θ_P (deg)	ϕ_P (deg)	% Total
Probe 1	45.2 ± 7.67	-110 ± 5.12	38%
Probe 2	43.2 ± 7.96	-73.0 ± 12.8	28%
Probe 3	63.0 ± 4.05	-64.9 ± 7.06	34%
	MyoV 6IQ$_{16}$ (Hemisphere)		
	θ_P (deg)	ϕ_P (deg)	% Total
Probe 1	47.8 ± 7.32	-111 ± 8.66	42%
Probe 2	38.3 ± 7.12	-69.5 ± 15.6	38%
Probe 3	64.7 ± 5.51	-62.8 ± 9.17	20%
	MyoV 4IQ		
	θ_P (deg)	ϕ_P (deg)	% Total
Probe 1	42.9 ± 5.39	-113 ± 11.1	26%
Probe 2	45.9 ± 5.71	-59.8 ± 8.83	45%
Probe 3	64.5 ± 6.59	-61.9 ± 4.45	29%

Table 3.2 - *Analysis of the θ_P vs. φ_P distributions calculated from the processive runs of MyoV-6IQ and -4IQ*

180° (**Figure 3.7B** and **Figure 3.8B**). Distributions of β_L for both constructs have two sub-populations with peak values that add up to approximately 180° (**Figure 3.7A**, **Figure 3.8A** and **Table 3.3**), as we would expect from the given constraint.

3.3.6 $\Delta\alpha_L$ distributions for myoV-6IQ and -4IQ

Distributions of $\Delta\alpha_L$ for both constructs (**Figure 3.11** and **Figure 3.12**) report the azimuthal changes in the lever arm of myoV after single steps along actin. The distributions constructed from the myoV-6IQ$_{12}$ and -6IQ$_{16}$ data sets each have three distinct populations with similar fitted peaks at $\Delta\alpha_{L,12} = -40°$, 1.4°, 33° and $\Delta\alpha_{L,16} = -46°$, -2.6°, 39° (**Table 3.3**). The straight-walking populations ($\Delta\alpha_{L,12} = 1.4°$ and $\Delta\alpha_{L,16}$

	β_L Angles (deg)		
	MyoV 6IQ		MyoV 4IQ
	Quartersphere	Hemisphere	Quarter-sphere
$\beta_{Leading}$	120 ± 12 (50%)	134 ± 16 (51%)	125 ± 15 (49%)
$\beta_{Trailing}$	61 ± 12 (50%)	48 ± 15 (49%)	56 ± 16 (51%)
	$^2\Delta\beta_L$ Angles (deg)		
	MyoV 6IQ		MyoV 4IQ
	Quartersphere	Hemisphere	Quarter-sphere
$^2\Delta\beta$	0.33 ± 9.4	−0.18 ± 14	0.48 ± 15
	$\Delta\alpha_L$ Angles (deg)		
	MyoV 6IQ		MyoV 4IQ
	Quartersphere	Hemisphere	Quarter-sphere
$\Delta\alpha_1$	−40 ± 14 (12%)	−46 ± 13 (15%)	−51 ± 28 (23%)
$\Delta\alpha_2$	1.4 ± 12 (62%)	−2.6 ± 12 (55%)	1.1 ± 8.6 (30%)
$\Delta\alpha_3$	33 ± 32 (26%)	39 ± 21 (30%)	28 ± 33 (44%)
	$^2\Delta\alpha_L$ Angles (deg)		
	MyoV 6IQ		MyoV 4IQ
	Quartersphere	Hemisphere	Quarter-sphere
$^2\Delta\alpha_1$	−37 ± 28 (16%)	−39 ± 20 (27%)	NA
$^2\Delta\alpha_2$	1.9 ± 15 (52%)	1.6 ± 16 (53%)	6.7 ± 88
$^2\Delta\alpha_3$	30± 29 (32%)	48± 19 (20%)	NA

Values result from Gaussian fits to distributions, and report peak mean ± σ.

Table 3.3 - *Analysis of the distributions of α and β angles for MyoV-6IQ and -4IQ in the Lever Arm frame of reference*

= -2.6°) make up ~60% of the total population in both data sets, indicating a heavy bias for myoV-6IQ to walk straight along the actin. The $\Delta\alpha_L$ distribution of myoV-4IQ$_{12}$ also has three sub-populations with peak values strikingly similar to those from the myoV-6IQ distributions ($\Delta\alpha_L$ = −51°, 1.1° and 28°; **Table 3.3**). Unlike the myoV-6IQ distribution, however, the straight-walking population from the myoV-4IQ distribution ($\Delta\alpha_L$ = 1.1°)

makes up only 30% of the total population, where the non-zero peaks make up a total of 70% of the population. This disparity shows that an individual molecule of myoV-4IQ is far likelier to take steps to the left or right than steps that are straight.

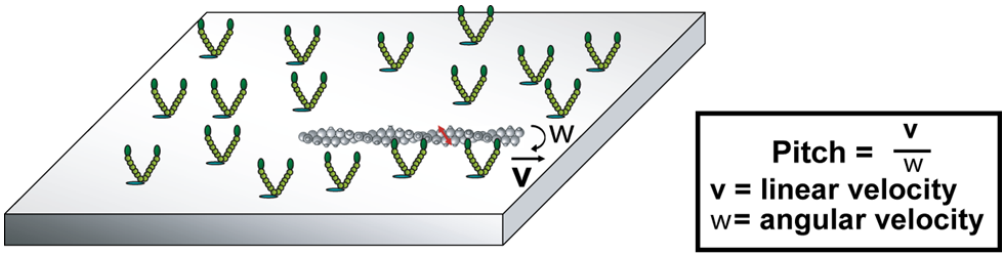

Figure 3.15 – *Experimental design for twirling experiment.*

myoV-6IQ or -4IQ is fixed to the surface and sparsely labeled BR F-Actin is flowed in along with 100 μM ATP. The angular velocity (w) is calculated from the change in α_P over time and the linear velocity (v) is calculated separately from gliding assays using myoV-6IQ or -4IQ.

3.3.7 Twirling of Actin in Gliding Assays with Myosin V-6IQ and -4IQ

In this assay, unlabeled myoV-6IQ or -4IQ with a Flag tag (see **Figure 3.2A**) was first introduced into a flow chamber coated with anti-Flag antibodies. Following this, actin sparsely labeled with rhodamine on cysteine-374 (0.3% rhodamine-actin, see Section 3.2.6), was flowed in (**Figure 3.15**; **34**). Activation mix containing 100 μM MgATP was then added and filament sliding velocities were measured with values of V = 112 ± 5.8 and 133 ± 7.0 nm/s for myoV-6IQ and -4IQ, respectively. The angle of the fluorescent probe in actin is determined during gliding by recording 16 polarized fluorescence intensities (**34**). This procedure enables the probe angle to be unambiguously determined within a hemisphere defined by β_P ranging from 0° to 90° and α_P ranging from -180° to 180° (see Section 3.2.3).

For both myoV-6IQ and -4IQ, the polTIRF intensities continuously rose and fell, where the individual polarizations exhibited various phase shifts relative to one another (**Figure 3.16**, *top*). These intensity changes indicate changes of probe angles as the actin

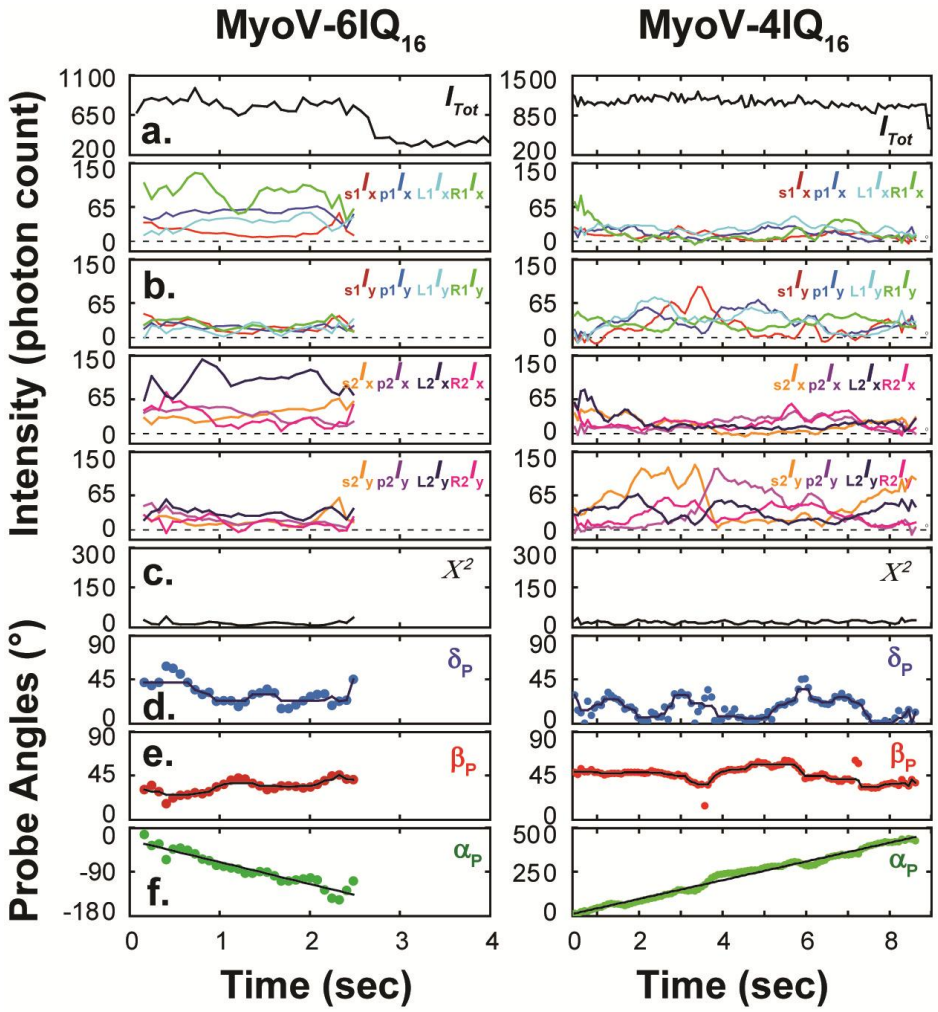

Figure 3.16 - *Representative traces from rhodamine-labeled actin filaments twirling over either myoV-6IQ$_{16}$ (left) or -4IQ$_{16}$ (right).*

Panels a-e: The total measured intensity is shown (***a***), along with the 16 component intensities that make it up (***b***). The time at which the intensities drop to zero indicates when the rhodamine probe bleached. ***Panels c-f:*** Calculation of the orientation of the probe in the actin frame. ***c.*** Trace of the χ^2 demonstrating the goodness-of-fit of the measured intensities to the calculated probe angles δ_P, θ_{lab}, and ϕ_{lab}. ***d-f.*** Traces of the angles δ_P (***d***), β_P (***e***), and α_P (***f***) in the Actin Frame, which were transformed from the angles θ_{lab} and ϕ_{lab} in the Laboratory Frame (see Section 3.2.3).

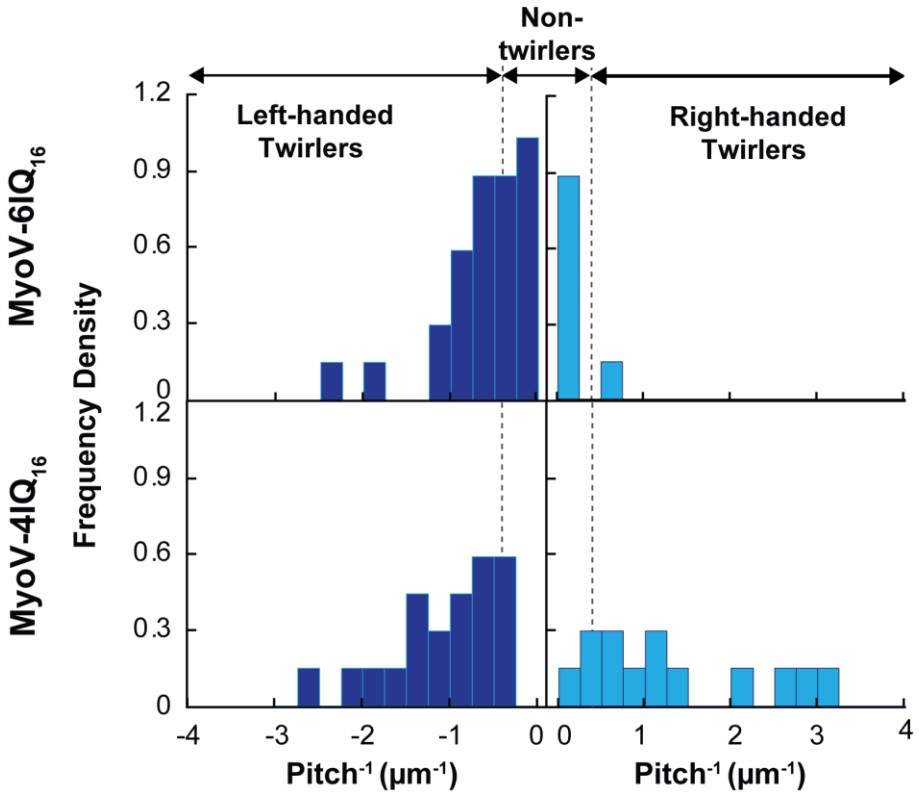

Figure 3.17 – *Inverse pitch (um^{-1}) distributions for myoV-6IQ$_{16}$ and -4IQ$_{16}$.*

Histograms of the inverse pitch (μm^{-1}) calculated from individual twirling actin filaments twirling along either the myoV-6IQ$_{16}$ (*Top*) or 4IQ$_{16}$ (*Bottom*) construct. Histograms are normalized so that the total area of the distribution is equal to one. Actin filaments with an inverse pitch < 0.4 μm^{-1} (pitch > 2.5 μm) are classified as non-twirlers. myoV-6IQ$_{16}$ twirls with a left-handed pitch, with a mean value of 1.4 μm, while myoV-4IQ$_{16}$ twirls either with a left- or right handed pitch, with mean values of 1.2 and 1.0 μm, respectively.

twirled around its axis during gliding (**34**). β_P often changes very little over the course of the experiment, as is expected since the probe is fixed to the actin. On the other hand, α_P changes linearly with a negative slope in myoV-6IQ and either a positive or negative slope in -4IQ (**Figure 3.16**). For each actin filament we calculated the pitch = V/ω, where V is the average linear velocity ($nm \cdot s^{-1}$) of sliding and ω is the angular velocity (rotations/s^{-1}) calculated from $\Delta\alpha_P/\Delta t$. Lower values for the pitch indicate more extreme twirling, and positive and negative signs indicate right- and left-handed twirling,

respectively. Inasmuch as some of the filaments did not twirl, as described for myosins II, V and VI (**34**,**104**), we calculated the inverse pitch (pitch^{-1} = μm^{-1}) to display both twirling and non-twirling filaments on single plots of their distributions (**Figure 3.17**). These distributions reveal two clear differences in the twirling behavior of myoV-6IQ and -4IQ. First we notice that a significant portion of the distribution for myoV-6IQ are non-twirlers (|pitch^{-1}| <0.4 μm^{-1} = 50%) compared to myoV-4IQ (|pitch^{-1}| <0.4 μm^{-1} = 6%). The other significant difference in twirling behavior of the two constructs lies in the handedness of the filaments that do twirl. Whereas myoV-6IQ twirls with a left-handed pitch with a mean value of 1.4 ± 0.13 μm (mean ± s.e.m.), agreeing with earlier studies of native myoV (**34**), -4IQ twirls either to the left (56%) or to the right (38%) with average pitches of 1.2 ± 0.14 μm and 1.0 ± 0.19 μm, respectively. MyoV-4IQ is the first myosin tested that can twirl robustly with either handedness.

3.4 Discussion

3.4.1 MyoV-4IQ has more frequent non-zero changes in α_L than myoV-6IQ

Subunits of F-actin form a right-handed helix with a helical half-pitch repeat of ~13 subunits equaling ~36 nm, the same distance as the average step-size of myosin V (**28**). EM studies have shown that a single step of myosin V can span 11, 13, or 15 actin subunits (**30**), corresponding to values for $\Delta\alpha_L$ of 27°, 0° and -27°, respectively ($\Delta\alpha_L$ is the change in α_L after one step of myosin V; **Figure 3.2C**). The principal peak of the distribution of myoV-6IQ $\Delta\alpha_L$ has a peak at $\Delta\alpha_L = 1.4 \pm 12°$ and accounts for 62% of the total distribution (**Figure 3.11** and **Table 3.3**). Such a large percentage of the myoV-6IQ steps being near zero would strongly bias it to walk straight along the actin filament. This $\Delta\alpha_L$ distribution also has sub-populations indicating myoV-6IQ taking occasional steps to the left ($\Delta\alpha_L = 33 \pm 32°$; 26%) and less frequently to the right ($\Delta\alpha_L = -40 \pm 14°$, 12%).

When looking at myoV-6IQ mediated actin twirling, we noted that a large portion of the observed actin filaments (50%) did not show any appreciable sign of twirling (**Figure 3.17**). This behavior is likely due to the bias for myoV-6IQ to step straight demonstrated in the $\Delta\alpha_L$ distributions (**Figure 3.11** and **Table 3.3**). The other 50% of the observed filaments from the twirling assay twirled with a left-handed pitch (**Figure 3.16** and **Figure 3.17**), as was observed previously (**35**,**34**). Only 26% of the observed steps in the myoV-6IQ $\Delta\alpha_L$ distribution were left-handed (**Table 3.3**), but this may be enough to bias the stepping of myosin V so as to cause actin to twirl with a left-handed pitch.

$^2\Delta\alpha_P$ is the change in α_L over two steps (equation 5.4.39 and **Figure 3.2C**), which can also be expressed as the sum of two sequential changes in α_L, $^2\Delta\alpha_P = \Delta\alpha_{L,1} + \Delta\alpha_{L,2}$. The three peaks from the myoV-6IQ $\Delta\alpha_L$ distribution have values of $\Delta\alpha_L$ = 33°, 1.4° and -40°, and the three peak values from $^2\Delta\alpha_P$ distribution are $^2\Delta\alpha_P$ = 32°, 1.8° and -39°. There are 6 unique values for $^2\Delta\alpha_P$ that can arise when considering every possible combination of $\Delta\alpha_L$ resulting from two sequential steps of myoV. The largest magnitudes of the possible values for $^2\Delta\alpha_P$ ($^2\Delta\alpha_P$ = 33° + 33° = 66° and $^2\Delta\alpha_P$ = -40° + -40° = -80°) are not apparent in the $^2\Delta\alpha_P$ distribution (**Figure 3.11** and **Table 3.1**). The $^2\Delta\alpha_P$ value arising from the combination of a left step followed by a right step ($^2\Delta\alpha_P$ = 33° + -40° = -7°) is near zero and would only compose a small portion of the near-zero peak in the $^2\Delta\alpha_P$ distribution since the frequency of right-handed steps is small (12%). The remaining possible values for $^2\Delta\alpha_P$ ($^2\Delta\alpha_P$ = 33° + 1.4° = 34°, $^2\Delta\alpha_P$ = -40° + 1.4° = -39°; $^2\Delta\alpha_P$ = 1.4° + 1.4° = 2.8°) represent the values of the fairly distinct peaks of the myoV-6IQ $^2\Delta\alpha_P$ distribution (**Figure 3.11** and **Table 3.1**). The near-zero peak ($^2\Delta\alpha_P$ = 1.8°) indicating two sequential straight steps makes up the major peak in the $^2\Delta\alpha_P$ distribution (55%), re-emphasizing that myoV-6IQ is strongly biased to walk straight.

MyoV-4IQ has an average step-size of 24 nm (**48**, **49**), two-thirds the size of the native myosin V's step-size. The principal peak of the myoV-4IQ distribution of $\Delta\alpha_L$ has a value of $\Delta\alpha_L$ = 28° and accounts for 44% of the total distribution (**Figure 3.11** and **Table 3.3**). A similar proportion of the steps myoV-4IQ takes are straight ($\Delta\alpha_L$ = 1.1°; 30%) and to the right ($\Delta\alpha_L$ = -51°, 23%). This puts this non-native, truncated construct in the interesting situation of having no directional bias when walking on actin. In the twirling assays for myoV-4IQ, only a few of the observed actin filaments did not twirl

(5.9%), and those that did twirl had either a left-handed (56%) or right-handed pitch (38%), an unprecedented behavior for myosin. The $^{2}\Delta\alpha_P$ for myoV-4IQ is very broad (σ = ± 88°) without distinguishable peaks (**Figure 3.11** and **Table 3.1**). The lack of a strong near-zero peak, as seen in the $^{2}\Delta\alpha_P$ distribution for myoV-6IQ, indicates that myoV-4IQ does not regularly take sequential straight steps.

.

3.4.2 Sub-populations in the distributions of θ_P vs. φ_P

The distributions of θ_P vs. φ_P from the processive runs of the myoV-6IQ constructs reveal three fairly distinct sub-populations; θ_1 = 45° and φ_1 = -110°; θ_2 = 43° and φ_2 = -73°; θ_3 = 63° and φ_3 = -65° (**Figure 3.13**A and **Table 3.2**). The calculated θ_P vs. φ_P depends on the orientation of the probe relative to the lever-arm (A.K.A., LCBD) of the individual myosin V being observed (see **Figure 3.2B**). The LCBD of myosin V has six IQ motifs to which calmodulin can bind. The crystal structure based model of the isolated LCBD with associated calmodulins has shown that each calmodulin has a different binding orientation relative to the LCBD (**101**). Because the labeled calmodulin has the probe rigidly bound to it on a single site (see Section 3.2.1), the three different sub-populations most likely arose due to the labeled calmodulin binding to different IQ motifs in the LCBD.

Strikingly, the three sub-populations that appear in the myoV-6IQ distributions are also apparent in the myoV-4IQ distributions, whose peak values and standard deviations correspond to those of myoV-6IQ: θ_1 = 43° and φ_1 = -113°; θ_2 = 46° and φ_2 = -60°; θ_3 = 65° and φ_3 = -62° (**Figure 3.13A** and **Table 3.2**). Our assumption about these

sub-populations indicates that there are three preferred sites for the labeled calmodulin to bind to. Since myoV-4IQ has only 4 IQ motifs in its LCBD, and since the sub-populations in the distributions from the two myoV constructs are comparable to one another, the possible IQ motifs to which the labeled calmodulins are bound should be limited to sites 1-4.

3.4.3 Comparing θ_P and φ_P values calculated from polTIRF data and myoV molecular model

A molecular model of a myosin V dimer with the two motor domains bound 13 actin subunits apart was recently constructed based on atomic-level and lower resolution structures (**100**). From this myoV model, we calculated the parameters θ_P, φ_P, β_P, α_P, β_L and α_L for each of the six potential labeling positions on the LCBD in both its leading and trailing positions (**Table 3.4** and **Figure 3.18**). The probe orientation was measured from a vector drawn between the two rhodamine labeling positions on each CaM (from P66 to the A73 position on the α-carbon, see **33**,**94**); the lever-arm orientation was measured from a vector drawn tangent to the myosin heavy chain at positions near the center of each CaM binding site. The probe vectors corresponding to the first three IQ positions have values for θ_P and φ_P (θ_1 = 58.3° and φ_1 = -118°; θ_2 = 49° and φ_2 = -45.1°; θ_3 = 58.3° and φ_3 = -59.5°) that are remarkably similar to the centers of the sub-populations from the θ_P vs. φ_P distributions for myoV-6IQ and -4IQ (**Table 3.2**, **Table 3.4**, and **Figure 3.18**). This is consistent with the three sub-populations isolated from the θ_P vs. φ_P distributions

arising from the labeled CaMs binding to either the 1st, 2nd, or 3rd IQ motif on the myosin V LCBD.

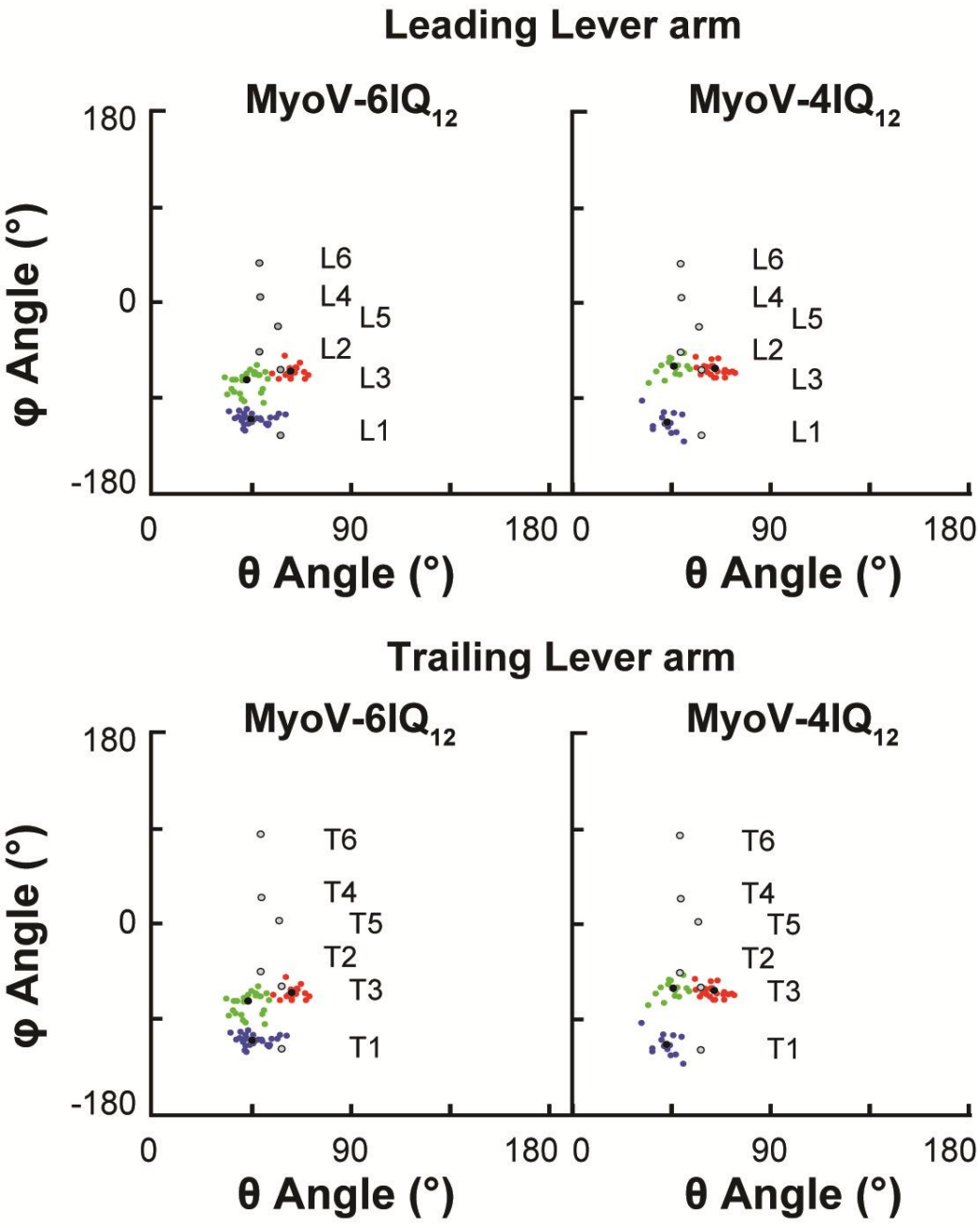

Figure 3.18 – *θ_P and ϕ_P values calculated from myoV model vs. those calculated from myoV-6IQ$_{12}$ and -4IQ$_{12}$.*

LCD in Trailing Position (Model)						
Labeled CaM	θ_P (°)	ϕ_P (°)	β_P (°)	α_P (°)	β_L (°)	α_L (°)
IQ 1 (T1)	58.3	-118	25.1	-165	46.8	87.7
IQ 2 (T2)	49	-45.1	32.2	0.4	37.1	93.6
IQ 3 (T3)	58.3	-59.5	27.1	-20.1	45.3	88.1
IQ 4 (T4)	49.4	24.5	73	31.4	40.3	77.6
IQ 5 (T5)	57.1	2.7	69.7	20.2	46.3	83.6
IQ 6 (T6)	48.9	83.9	102.3	68.9	53.6	73.7
LCD in Trailing Position (polTIRF)						
Peak Number	θ_P (°)	ϕ_P (°)	β_P (°)	α_P (°)	β_L (°)	α_L (°)
1	45.2 ± 7.67	-110 ± 5.12	21.4 ± 7.46	—	60.9 ± 11.4	—
2	43.2 ± 7.96	-73.0 ± 12.8	24.6 ± 6.32	—	63.6 ± 6.34	—
3	63.0 ± 4.05	-64.9 ± 7.06	29.0 ± 6.36	—	42.0 ± 10.3	—
LCD in Leading Position (Model)						
Labeled CaM	θ_P (°)	ϕ_P (°)	β_P (°)	α_P (°)	β_L (°)	α_L (°)
IQ 1 (L1)	58.3	-125	67	138	116	106
IQ 2 (L2)	49	-47	70.1	74.8	107	108
IQ 3 (L3)	58.3	-63.4	81.3	65.2	136	88
IQ 4 (L4)	49.3	4.9	119	17.6	132	77
IQ 5 (L5)	57.1	-23	104	15.9	143	69
IQ 6 (L6)	49	36.5	143	-39.8	146	50
LCD in Leading Position (polTIRF)						
Peak Number	θ_P (°)	ϕ_P (°)	β_P (°)	α_P (°)	β_L (°)	α_L (°)
1	45.2 ± 7.67	-110 ± 5.12	75.6 ± 12.3	—	119 ± 9.86	—
2	43.2 ± 7.96	-73.0 ± 12.8	78.8 ± 8.29	—	114 ± 9.23	—
3	63.0 ± 4.05	-64.9 ± 7.06	76.8 ± 12.2	—	138 ± 11.6	—
Deltas from Leading to Trailing Transition (Model)						
Labeled CaM	$\Delta\theta_P$ (°)	$\Delta\phi_P$ (°)	$\Delta\beta_P$ (°)	$\Delta\alpha_P$ (°)	$\Sigma\beta_L$ (°)	$\Delta\alpha_L$ (°)
IQ 1 (T1)	0	-7	41.9	-57	162.8	18.3
IQ 2 (T2)	0	-1.9	37.9	74.4	144.1	14.4
IQ 3 (T3)	0	-3.9	54.2	85.3	181.3	-0.1
IQ 4 (T4)	-0.1	-19.6	46	-13.8	172.3	-0.6
IQ 5 (T5)	0	-25.7	34.3	-4.3	189.3	-14.6
IQ 6 (T6)	0.1	-47.4	40.7	-108.7	199.6	-23.7
Deltas from Leading to Trailing Transition (polTIRF)						
Peak Number	$\Delta\theta_P$ (°)	$\Delta\phi_P$ (°)	$\Delta\beta_P$ (°)	$\Delta\alpha_P$ (°)	$\Sigma\beta_L$ (°)	$\Delta\alpha_L$ (°)
1	—	—	54.2	40.8 ± 18.4	180	10.5 ± 8.61
2	—	—	54.2	19.5 ± 11.2	180	11.0 ± 6.58
3	—	—	47.8	89.3 ± 15.5	180	10.5 ± 8.50

Table 3.4 - *Parameters from myosin V molecular model and myoV-6IQ polTIRF data*

The expected values of β_P from the model when the LCBD is in both the leading and trailing position are very similar to the measured values from our data (**Table 3.4**). There are differences, however, when considering the β_L values calculated from the polTIRF data and those calculated from the model. This difference is most easily seen from the calculated values for $\Sigma\beta_L$ (see equation 3.2.6) from our data and from the model. Each of the three sub-populations of the distributions for θ_P vs. φ_P calculated from the polTIRF data had corresponding calculated values for $\Sigma\beta_L$ of 180°, matching the constraint imposed by the analysis (see Section 3.2.7 and **Table 3.4**). In the model of myoV, the probe at IQ position 3 also has a $\Sigma\beta_L$ of ~180°, and the values for θ_P vs. φ_P closely match the values from the third peak of the θ_P vs. φ_P distribution (**Table 3.4** and **Figure 3.18**). The values for θ_P and φ_P calculated for IQ positions 1 and 2 from the myoV model are moderately shifted compared to the values calculated from peaks 1 and 2 of the θ_P vs. φ_P distributions of the polTIRF data (**Table 3.4** and **Figure 3.18**). The $\Sigma\beta_L$'s of 163° and 144° calculated from IQ position 1 and 2 of the model, are significantly different from the $\Sigma\beta_L$ = 180° constraint placed on our analysis because of the curvature of the leading arm in the model; this may account for the small shift between the parameters from our data and those of the model.

As myosin V steps along actin, it switches between one of two β_P states, generally attributed to the leading and trailing positions of the lever arm (**88**,**33**) (see Section 3.2.7). The ambiguity of the probe orientation that arises from the dipole exists for each angular state of a processive run of myoV. Considering that myoV alternates between two β_P states where each of these states has two equivalent orientations due to the dipole symmetry, any processive run of myoV has $2^2 = 4$ potential probe solutions (see Section

3.2.7). When taking into consideration the two-fold degeneracy intrinsic to the lever solution, there are then eight potential lever solutions calculated from the four measured probe orientations (see Section 3.2.7 see **Figure 3.4** and **Figure 3.5**). Our method for calculating θ_P and φ_P, coupled with a molecular model of myosin V (**100**), gives us the means to reduce the number of probe and lever solutions considerably shown in **Figures 3.4** and **3.5**. By comparing the potential probe orientations β_P and α_P from the polTIRF data with a myoV molecular model, we can limit the number of possible solutions. The values for β_L, α_L, θ_P and φ_P calculated from the polTIRF data can also be used to compare to the molecular model so as to constrain the possible solutions. Conversely, if we had some other means to limit the potential probe solutions, this method would allow us to better refine existing molecular models of myosin V such as the Bryant model (**100**).

3.4.4 Conclusion

We found that the removal of two IQ motifs from the LCBD of myosin V led to myoV-4IQ taking fewer straight steps than the native myoV-6IQ construct, as we expected. However, considering the 24 nm step-size of myoV-4IQ, the observation that the -4IQ and -6IQ took steps to the left and right of similar magnitude, as measured by $\Delta\alpha_L$, was unexpected. Although these left and right handed steps are very frequent in myoV-4IQ constructs, this may not fully explain the actin twirling experiment for -4IQ, where it twirled to the left and right with similar frequency. Since the twirling of actin is a result of a *group* of myosin Vs stepping on actin, more detailed experiments are

required that examine the effects of neighboring myosin Vs on one another's stepping behavior.

We also found three distinct sub-populations in the distribution of the θ_P vs. φ_P angles (**Figure 3.13** and **Figure 3.14**). We tentatively attribute these sub-populations to distinct binding sites of the labeled BR-CaM on the LCBD of myosin V. This agrees with other studies that have also inferred BR-CaM binding to three separate sites on the LCBD (**88**,**91**). The θ_P and φ_P values calculated from our polTIRF data also closely agree with expected values for the IQ positions 1, 2 and 3 determined from a molecular model of myosin V (**100**).

Actin Frame of Reference	
Variable	Definition
x_A	x_A z_A and x_A slide surface
y_A	y_A z_A and y_A x_A
z_A	z_A actin; points toward myoV motion
β_P	Axial angle of probe - measured from the z_A-axis
α_P	Azimuthal angle of probe - measured from the x_A-axis to the projection of the probe in the x_A-y_A plane
Ω_P	Solid angle of the lever relative to actin, described by β_P and α_P
β_L	Axial angle of lever - measured from the z_A-axis
α_L	Azimuthal angle of lever - measured from the x_A-axis to the projection of the lever in the x_A-y_A plane
Ω_L	Solid angle of the lever relative to actin, described by β_L and α_L
Lever Frame of Reference	
Variable	Definition
x_L	x_L z_L and x_L y_L
y_L	y_L z_L-motor domain plane
z_L	z_A lever; points toward myoV C-terminus
θ_P	Local angle of probe - measured from the z_L-axis
ϕ_P	Local angle of probe - measured from the x_L-axis to the projection of the probe in the x_L-y_L plane
Lab Frame of Reference	
Variable	Definition
x_{lab}	x_{lab} z_{lab}; Laser path 1 lies in the x_{lab}-z_{lab} plane
y_{lab}	y_{lab} z_{lab}; Laser path 2 lies in the y_{lab}-z_{lab} plane
z_{lab}	z_{lab} microscope objective; points down
θ_{lab}	Angle of probe - measured from the z_{lab}-axis
ϕ_{lab}	Angle of probe - measured from the x_{lab}-axis to the projection of the probe in the x_{lab}-y_{lab} plane

Table 3.5 - *List of Variables*

4 Global Discussion

My main goal for this thesis has been in relating the kinetic function of myosin to its mechanical function; how the small conformational changes upon ATP binding and hydrolysis that occur in the nucleotide binding pocket of the motor domain is translated to the much larger swing of the lever arm is of great interest to me. When looking at myosin Ib, the principal approach that I took for relating the chemical and mechanical activities to one another was to characterize key rates of its ATPase cycle using bulk solution experiments measured in the stopped flow, and relate these to the rates associated with the mechanical steps observed in the single molecule optical trap experiments. Doing this for myosin Ib demonstrated that the two sub-steps associated with its power stroke that occurred during actin attachment corresponded well to the ADP release and ATP binding steps of the ATPase cycle (see Section 2.3.2; **19**). Moreover, because ADP release was rate limiting for exiting the strong binding state and the overall ATP turnover time was long, we were able to predict the extreme force sensitivity that was later observed in the force feedback experiments (see Section 2.3.2; **19**).

Putting the basic chemomechanical activity of the myosin Ib into the context of its function in a cellular environment requires looking at the response of the myo1b activity to cellular regulation. We first looked at a genetic regulatory element of myosin Ib, specifically the dependence of the light chain binding domain (LCBD) on its mechanical function. We found that the overall dependence of the LCBD length to the step-size had a non-linear relationship. This was surprising since other studies performed on other myosin family members showed a linear dependence on the LCBD length for the step-size. We suspect this is due to some compliance in the LCBD. What was most interesting

from this study was the finding that the force sensing of myo1b, measured by the distance parameter d_{det}, was linearly dependent on the LCBD length. In the case of the myo1b with 1 IQ and 4 IQs in its LCBD, their calculated values for d_{det} matched their calculated step-sizes. This led to the proposed model where the LCBD under tension is pulled back the full distance of its power-stroke where it remains strongly bound to actin in an ADP-bound like state.

The calcium regulation experiments performed on myo1b were an example of external regulation. These studies provided a mechanism that explains the paradoxical influence of calcium on the mechanics and kinetics, where motility in gliding assays are stopped by the same concentration of calcium that increase the myo1b kinetic activity. We found through single molecule optical trap and ensemble-level stopped flow experiments that calcium binding to the the myo1b LCBD leads to a drastic reduction (7-fold) in myo1b step-size and a corresponding increase in rate of actin detachment. The force sensing of myo1b as measured by was also dramatically decreased 6-fold in the presence of calcium. Because the step-size results were similar for myo1b with 1 ($myo1b^{IQ}$) and 6 IQ motifs ($myo1b^{a}$); and because $myo1b^{a}$ in the presence of calcium had the same value for d_{det} as calcium-free $myo1b^{IQ}$, we concluded that the first calmodulin was most important to the observed regulatory effect of calcium. We were also able to conclude that the effects of calcium binding on both the mechanical and kinetic activities of myo1b are very fast (>1000 s^{-1}).

The single molecule experiments, and consequent analysis, on myosin V (myoV) were designed to track the dynamic conformational changes in the LCBD as it processively steps along actin. The experiments performed used polarized TIRF

microscopy (polTIRF) provided time resolved measurements of the orientation of the rhodamine probe that labeled the calmodulin bound to the myoV LCBD. In general, the orientation of the probe does not accurately report the orientation of the lever arm. We therefore developed an analysis that allows us to transform the time-resolved probe orientations to the time-resolved orientations of the lever arm that the probe is attached to. This analysis was done on probe measurements obtained from recombinant myoV with a native-length lever arm (myoV-6IQ) and a truncated lever arm (myoV-4IQ). The axial angles of the lever arm (β_L) (corresponding to the swing of the lever as myoV steps) was similar for both constructs. However, differences in the azimuthal angle of the lever arm (α_L) between the two constructs demonstrated that the native myoV-6IQ is heavily biased to walk straight; whereas the truncated myoV-4IQ rarely steps straight and steps to the left or right on actin with equal likelihood. The orientation of the probe relative to the lever arm was calculated for each of the observed myosins from both constructs and we found that both had three nearly identical sub-populations. Based on comparison to a molecular model, these sub-populations closely correspond to labeling positions on the first three IQ motifs of the LCBD.

4.1 Future Directions

4.1.1 Does calcium regulate myosin Ib on a physiologically relevant time scale?

The regulation of myosin Ib tension sensing by calcium binding was discussed in Chapter 2. The calcium-dependent decreases in the step size and distance parameter (d_{det}) of myo1b were significant, but were at their steady state levels by the time the individual events were measured. Using a range of calcium concentrations for these experiments, we inferred that calcium binds to and decreases the myo1b step size on a fast time scale. Because the rate of calcium binding and its effect on step size establishes the relevance of this calcium binding in a living cell, it is vital to conclusively establish the rate of the calcium regulation using direct measurements.

Calcium can be kept from binding to the calmodulins bound to myosin Ib by using a caged calcium that can be released by photolysis when flashed by a laser. This caged calcium can be used in conjunction with the optical trap experiments described in chapter 2, where the caged calcium would be released as a single myosin Ib is undergoing actin attachment events. Releasing the caged calcium in this way is conceptually the same as rapidly introducing calcium to the system, as would be done in a stopped flow apparatus, and so would allow us to calculate the rate of calcium's effect on the myo1b step size.

4.1.2 What residues in the myo1b binding pocket contribute to its force sensitivity?

Chapter 2 demonstrated that the force sensitivity of myosin Ib is dependent on the length of its lever arm. As the lever arm gets shorter, the force sensitivity as measured by its distance parameter (d_{det}) also gets smaller. The direct impact of the application of force along the lever arm is to increase the lifetime of actin attachment for myosin Ib. More specifically, the force dependent decrease in the rate of ADP release becomes the rate limiting step for actin detachment. The decrease in the rate of ADP release could be a result of the force applied to the lever arm leading to a global conformational change in the motor domain, physically blocking the ADP from unbinding. Another possibility is that the force transmitted along the lever arm changes the relative positions of some of the residues in the myo1b nucleotide binding pocket, leading to a greater stabilization of the ADP in the nucleotide binding pocket. The latter possibility can be tested by mutating residues in the binding pocket that make contact with ADP based on the atomic resolution structure of myosin. The residues important for binding would be mutated to amino acids with shorter or longer side chains. The purpose of changing the side chain length is to perturb the stability of ADP binding when it is in its force induced state. We could then measure the force dependence of the various mutant myo1bs in the same way as described in chapter 2; those mutants that lead to a significant change in the distance parameter of myo1b would be important to its force sensing ability. It will be important to do controls that these mutants are still competent to undergo the myo1b ATPase cycle, although the rates of the individual steps might be altered.

4.1.3 How does the conformation of the myosin lever arm change during actin attachment?

The power stroke is the primary function of myosin, which occurs during the strongly actin-bound stage of its crossbridge cycle (see Chapter 1). Although there are numerous crystal structures of myosin at different stages of ATP hydrolysis when it is unbound to actin, there are no structures of myosin at any stage when it is strongly bound to actin. Experiments in chapter 3 demonstrate how to measure the conformation of the lever arm as myosin V steps along actin filaments. This same method could be used to measure the change in the myo1b lever arm conformation relative to actin as it undergoes its two step power stroke. Simultaneous measurements of the actin displacement caused by the myo1b power stroke and the corresponding change in lever arm conformation can be achieved with an instrument that combines the optical trap (see Chapter 2) with a polTIRF setup (see Chapter 3). The myo1b would be labeled in a similar fashion to that described in Chapter 3, where the fluorescently labeled calmodulin BR-CaM was singly exchanged onto one of the lever arms of myosin V. This setup would also allow us to measure the difference in lever arm conformations for the three different isoforms of myosin Ib, which had different lever arm lengths; this may help resolve why the lever arm length dependence of the myo1b step-size is non linear.

4.1.4 How are the chemical steps of ATP hydrolysis coupled to the mechanical steps of the power stroke of myosin Ib?

I indicated in Chapter 2 that the two steps of the power stroke of myo1b are associated with the steps of ADP release and ATP binding. This was inferred based on determining which of the two sub-steps of the myo1b power stroke were ATP-dependent, which was found to be the second one. It was recently shown that one can simultaneously measure individual steps of ATP hydrolysis associated with the myosin ATPase cycle and the corresponding actin displacement associated with the myosin power stroke by using a combined TIRF and optical trap experimental setup (**105**). The trap is in a similar configuration to that described in Chapter 2; and the TIRF is used so as to measure changes in intensity of a fluorescent ATP as it is hydrolyzed by myosin. This combined optical setup would allow for direct, time-resolved measurements of ADP release and ATP binding coupled to the mechanical events of the myo1b power stroke.

5 Appendix

5.1 Program for Optimization of a Maximum Likelihood Estimator

5.1.1 Maximum Likelihood Estimator (MLE)

Maximum Likelihood Estimation is a well established method for finding the optimum parameters of a model that fits a given set of data. I offer a brief treatment of it here, but it discussed extensively in numerous texts; particularly clear descriptions are given in Numerical Recipes for C (**66**) or Bevington's Data Analysis (**105**).

Given a set of data *x* with *N* members defined as:

$$x \equiv \{x_0, x_1, x_2, \dots, x_N\} \tag{5.1.1}$$

We assume that *x* is represented by a distribution with an associated probability distribution function (PDF) *f*:

$$PDF = f(x, \Omega); \quad \Omega \equiv \{\omega_0, \omega_1, \omega_2, \dots, \omega_k\} \tag{5.1.2}$$

where Ω is the set of parameters that describes the PDF. We wish to determine the set of parameters Ω that best fit our data. For a given set of Ω, we can calculate the Likelihood function for our data according to the following:

$$L = \prod_{i=0}^{N} \mathrm{f}(x_i, \Omega)$$

5.1.3 - Likelihood Function

where $i = 0, 1, \ldots, N$. Likelihood is similar to the probability, except likelihood describes events that occurred in the past, and probability describes the behavior of future events (**105**). There is a set of parameters Ω_0 that represents the "true" parameters representing the distribution for x. The maximum of the Likelihood function (equation 5.1.3) occurs when $\Omega = \Omega_0$ (**105**). Therefore, Maximum Likelihood Estimation allows us to estimate Ω_0 by finding the maximum of equation 5.1.3. This maximum can be explicitly found in some cases by calculating the partial derivatives of the Likelihood function, L:

$$\frac{\partial L}{\partial \omega_j} = 0$$

5.1.4

When this system of equations cannot be solved analytically, an optimization routine is necessary to find the parameters, Ω_0. Because the Likelihood frequently calculates unmanageably small numbers, it is generally more convenient to use the Log Likelihood function ($\ln(L)$)(**105**):

$$\ln(L) = \sum_{i=0}^{N} \ln\big(\mathrm{f}(x_i, \Omega)\big)$$

5.1.5 - Log Likelihood Function

When a single model is applied to multiple data sets for simultaneous fitting, a two-dimensional form of equation 5.1.5 is required:

$$\ln(L) = \sum_{j=0}^{M} \sum_{i=0}^{N} \ln\left(\mathrm{f}\left(X_{i,j}, \Omega\right)\right) \qquad \textbf{5.1.6}$$

where $X_{\mathrm{i,j}}$ is a matrix with j columns of the data x (see expression 5.1.1), j = 0, 1, … M, and M is the number of data sets. Finding the extremum of equation 5.1.6 would provide the best fit single set of parameters Ω that characterize the M data sets, $X_{\mathrm{i,j}}$.

5.1.2 Optimization of a MLE Model Using a Modified Nelson-Mead Downhill Simplex method

Fitting data with multi-parameter models can be challenging. The range of solutions for a model can be represented as a multi-dimensional landscape, and the goal for any optimization routine is to find the global minimum of that landscape. The dimension of that landscape is determined by the number of parameters that are being optimized. In other words, a model with N parameters requires finding the global minimum for an N-dimensional landscape of model solutions. Popular optimization routines such as Levenberg-Marquadt and Conjugate Gradient have algorithms that hunt for minima by following downhill slopes in the solution landscape (**66**). A major drawback of these methods is their propensity for getting trapped in the (often numerous) wells of local minima spread throughout a solution landscape. The parameters associated

with these local minima are often far from those associated with the global minimum. Thus it is desirable to use an optimization routine that will find the global minima of the N-dimensional solution landscape without getting trapped in any local minima.

A modified Nelson-Mead downhill simplex optimization algorithm was developed to avoid the local minima of the model's solution landscape. Given a model with N parameters, the N+1 vertices of the simplex are formed by calculating values from the expression to be optimized using N+1 guesses for the parameters (**66**) (a simplex is a geometric shape, where a triangle is a simplex with three vertices in a plane). The vertex of the simplex that corresponds to the worst solution is thrown out and replaced with a new vertex calculated based on causing a reflection, expansion, contraction or reduction of the simplex in an N-dimensional space (**66**). The movement of the simplex looking for the global minimum has been described as similar to that of an amoeba looking for food, going through multiple contortions. When the volume of the simplex has been minimized, which in many cases means the N+1 vertices have converged to a single point, the algorithm assumes the global minimum has been found.

Unfortunately, the downhill simplex algorithm by itself is confounded by solution landscapes with many local minima. To avoid these local minima, the simplex optimization routine was re-started multiple times. With each re-start, one of the N parameters is randomly selected and a new value for the parameter is determined (**Figure 5.1**). The new value for the currently selected parameter is calculated from its current value by randomly adding or subtracting a fraction of that value:

$$p_i^* = p_i \pm \Delta p_i$$

5.1.7

where $i = 1, 2, \ldots, N$ (N = number of parameters in the model) and the decision whether

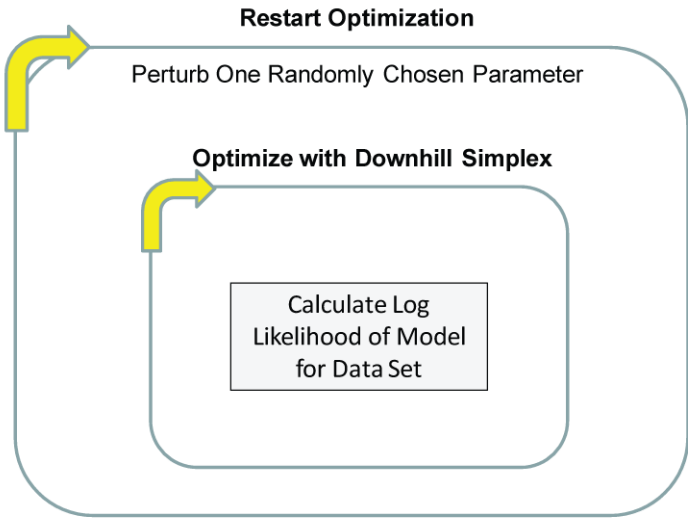

Figure 5.1 – *Program Flow Chart for Downhill Simplex/Annealing Optimization Routine*

Routine for finding optimized parameters from fitting a model to a data set (or one of M simulated data sets). The optimization routine is general and can be applied using MLE- or χ^2-based models .

to add or subtract Δp_i is random. Increasing or decreasing the value of this selected parameter after an initial optimization effectively "kicks" the routine out of any local minima it may be trapped by in the solution landscape. This approach is similar to the Annealing method for continuous functions discussed before (**66**). The value for the increment Δp_i is determined by:

$$\Delta p_i = (r - j * \Delta r) * p_i$$

5.1.8

where *r* a user-defined value between 0 and 1 and j•Δ*r* = r, where j is an arbitrary user-defined value. Because of the term j•Δ*r*, the increment Δp_i added to or subtracted from the value of the selected parameter becomes progressively smaller with each re-start of the optimization routine. Choosing good values for r and j is currently based largely on trial and error and further work needs to be done to find a robust algorithm similar to equation 5.1.8 that does not require user input.

5.1.3 Confidence Intervals are Determined by Using Bootstrap Monte Carlo Simulations

There are errors in measuring a data set, *D*, that influence the parameters, *p*, calculated from a model fit to *D* (**66**). Because some of these errors are random, each fit to *M* subsequent data sets measuring the same process will result in *M* unique parameters. Therefore, the data sets resulting from M measurements of the same process are D_0, D_1, …, D_M with corresponding fit parameters $P \equiv p_0, p_1, \ldots, p_M$ (**66**), where the original data and parameters are D_0 and p_0. The breadth of the distribution P is a reflection of the underlying error intrinsic to obtaining the measurements in *D*. The location of p_0 relative to the elements of *P* gives us a definition of our confidence interval. The confidence interval for p_0 is established by the boundaries that contain a certain percentage of the *M* data sets with p_0 at the center. For example, a confidence interval of 94%, is defined by

boundaries containing 94% of the M data sets and centered on p_0 (**Figure 5.2**). The confidence interval itself is calculated from the difference between p_0 and the values of the parameters associated with the boundaries, where (+) values is the interval to the right, and (-) values is the interval to the left in **Figure 5.2**. 90% is generally satisfactory for most scientific research, and the lowest acceptable value is 67%. (**66**).

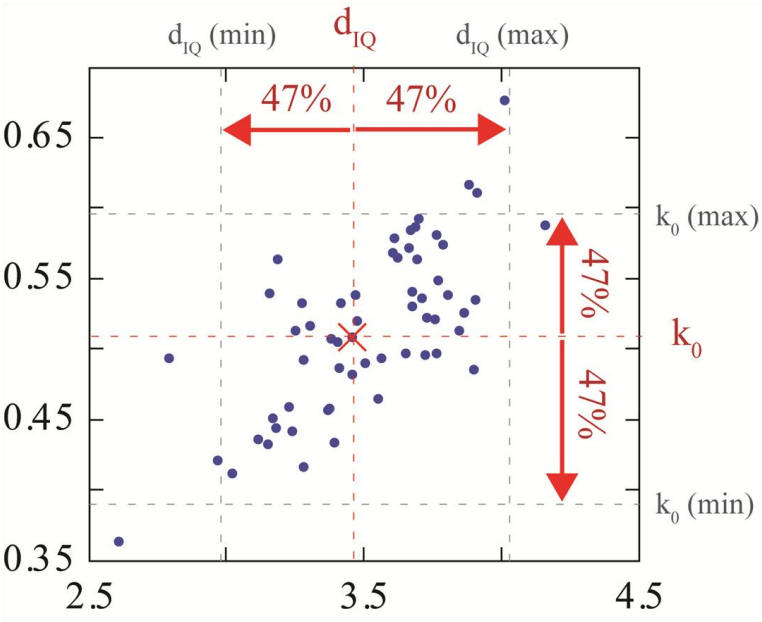

Figure 5.2 – *Calculating the confidence interval*

Calculating the confidence interval is visualized here by mapping out the two-dimensional parameter space for k_0 and d_{IQ}. The optimized parameter values calculated from the data are shown at the center of the plot (X), where $k_0 = 0.46\ s^{-1}$ and $d_{IQ} = 3.45$ nm. The blue dots plotted represent the optimized parameter values obtained from N = 50 boot-strap simulated data sets. For a confidence interval of 94%, maximum and minimum values for both k_0 and d_{IQ} are defined by the outermost boundaries of a box that contains 94% of the simulated data sets. By subtracting these values from the original fit values, the +/- confidence intervals are determined for each parameter.

In that re-measuring a process multiple times is often not feasible, an acceptable alternative is to simulate the data sets. A particularly powerful simulation method that is

easy to use is known as Bootstrap Monte Carlo or simply as Bootstrap (**66**). Bootstrap can simulate a data set, *D*, without having to assume a particular model or distribution (**66**). For a data set *D* with *N* elements, a simulated data set D^S is generated by taking *N* random draws from *D*. Because the draws are random, there is duplication of some of the points from *D* that are used to make up D^S. In fact ~ 37%, or 1/e, of the original *N* data points from *D* are duplicated in D^S (**66**). Bootstrap has the single condition the *N* elements of *D* be independent and identically distributed (iid), which essentially means that the order of the *N* data points is not important to the process being studied (**66**). Restarting this process *M*-times results in *M* unique simulated data sets. The distribution of parameters, P^S, calculated by fitting the model to these data sets allows us to calculate the confidence intervals of our original parameters, as described above.

5.1.4 General Simplex Fit model fitting program

5.1.4.1 Overview of program features - General Simplex Fit is a program for simultaneously fitting a model to multiple data sets

The General Simplex Fit program is written in Labview and utilizes the Annealing algorithm described above (see Section 5.1.2) to find the optimized parameters for any model fit to a given data set. The program allows for fitting to either χ^2- or MLE-based models. This program also allows for simultaneously fitting a model to multiple data sets. This feature is flexible, so each parameter of the model has the option of being simultaneously fit to the data sets (see equation 5.1.8). Multiple models can also be fit to multiple data sets. In short, this program is very flexible to allow the user to make as

complex, or simple, model fitting as they choose.

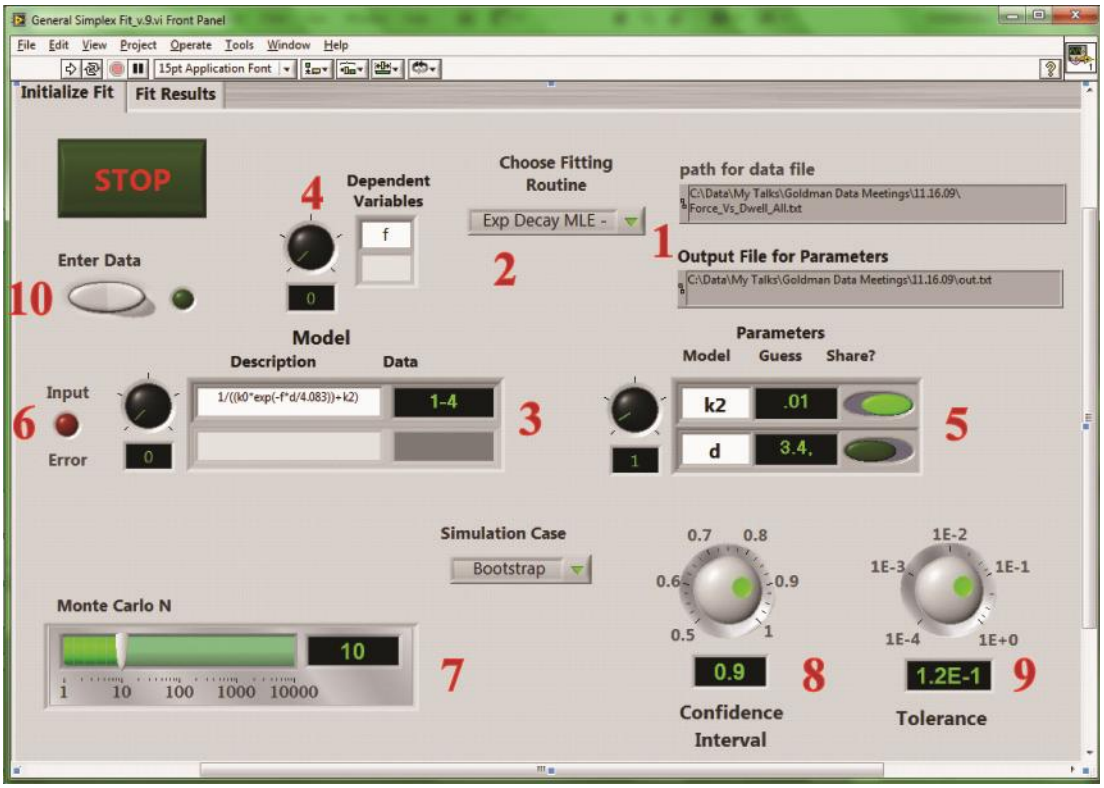

Figure 5.3 – *Front panel of General Simplex Fit program.*

5.1.4.2 Data and model input

Figure 5.3 shows the front panel of the General Simplex Fit program. The front panel has multiple fields for inputting the data to be fit; inputting the model and guesses for its associated parameters; and variables affecting the optimization process. This section details the required input for each field on the front panel of the program.

Data input. Data is input from a *.txt file. The path to this file is input in the field labeled "**path for data file**" (see **1** in **Figure 5.3**). This file is formatted with the measured data placed in the first column and the variable(s) the measured data is dependent upon is placed in the next column(s). This program allows for one independent variable (measured data) and any number of dependent variables.

Fit parameters and their associated confidence intervals are written to a *.txt file named by the user. The path to this file is input in the field labeled "**Output File for Parameters**" (see **1** in **Figure 5.3**).

Inputting the model and its associated parameters. This program will accept χ^2- or MLE-based models for optimization (see **2** in **Figure 5.3**). Data for χ^2 models must include both independent and dependent variables. Data for MLE models do have to include an independent variable. MLE models must be expressed in the form of a probability distribution function. The parameters for both MLE and χ^2 models are optimized using the Annealing algorithm described above (see Section 5.1.2).

The model and the data sets it is applied to are placed in the fields under "**Model**" (see **3** in **Figure 5.3**). The equation describing the model is placed in the field labeled "**Description**". This field accepts only ASCII characters, so symbols or characters from other formats will not be recognized. When inputting parameters or variables, they should use at most one lower case letter followed by a number, such as k1, k2, … or x1, x2,

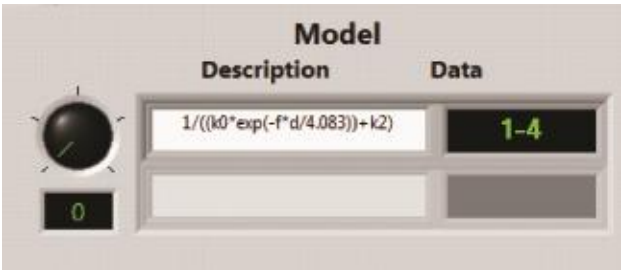

…. Any unrecognized characters will cause the "**Input Error**" light to turn on (see **6** in **Figure 5.3**). There is no explicit limit to the number of parameters and dependent variables declared in the model. The data sets that the model is to be applied to are indicated in the "**Data**" field. Multiple data sets have to be entered with commas separating them (1, 2, 3, 4) or with a hyphen if they're sequential (1-4). Multiple models can be entered as well. Both the "**Description**" and "**Data**" fields point to arrays, so any number of models can be applied to any number of data sets. The dial to the left of the fields changes the index of the arrays that the "**Description**" and "**Data**" fields point to.

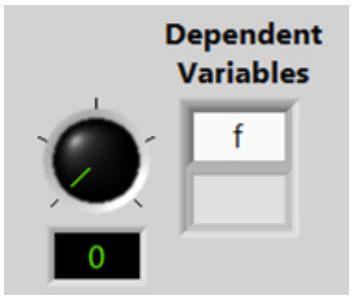

The dependent variables associated with the model have to be entered in the "**Dependent Variable**" field (see **4** in **Figure 5.3**). Any number of dependent variables can be associated with the model. When entering the variable names in the field they must exactly match what was placed in the "**Model Description**" field (see above). If they do not match, or are absent, the "**Input Error**" light will turn on (see **6** in **Figure 5.3**).

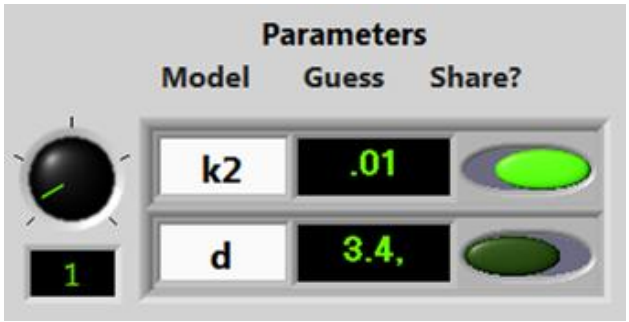

Initial guess values for the parameters associated with the model(s) are entered in the "**Parameters**" field (see **5** in **Figure 5.3**). Any number of parameters can be associated with the model. When entering the parameter names in the "**Model**" field they must exactly match what was placed in the "**Model Description**" field (see above), otherwise an "**Input Error**" light will turn on (see **6** in **Figure 5.3**). If the parameter will be calculated from

all of the data sets, turn on the "**Share**" toggle; leave it off otherwise. The default is for it to be on. A guess value must be associated with each parameter. If the "**Share**" toggle is on, enter only one guess. Otherwise, enter one guess for each data set the parameter is being calculated for. When multiple guesses are entered, they must be separated by commas.

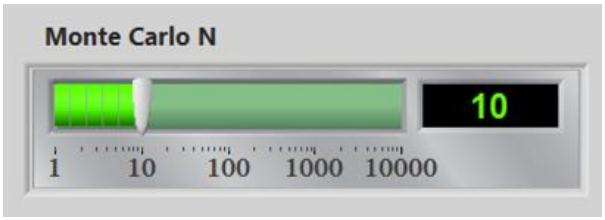

Inputs for error handling. The "Monte Carlo N" slider in **7** from **Figure 5.3** controls the number of simulated data sets constructed from the Bootstrap Monte Carlo method (see Section 5.1.3). A setting of 1 will only display the data; a setting of 2 will initiate fitting of the data without forming any simulated data sets; a setting of N > 2 will cause the data to be fit and generate N-2 simulated data sets from which the confidence intervals are calculated (see Section 5.1.3). The desired confidence interval is entered in the "Confidence Interval" input field (see **8** in **Figure 5.3**). The maximum input value is 1 (100% confidence interval).

The "Tolerance" input field allows control of the precision of the fit parameters (see **9** in **Figure 5.3**). A setting of 0.1 is sufficient for initial test fits, while lower settings (<0.001) should be used when precision is required.

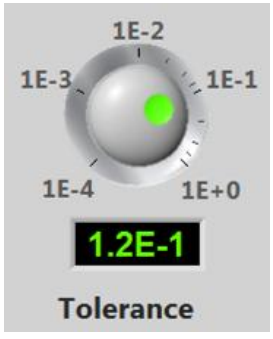

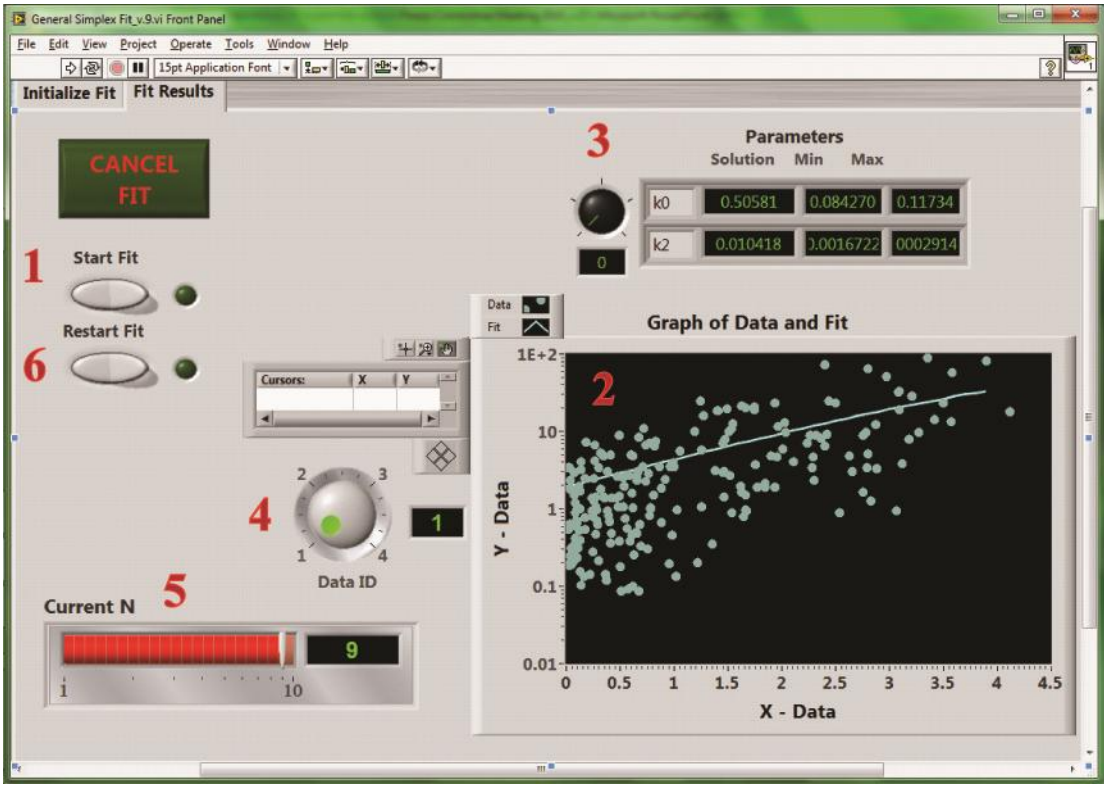

Figure 5.4 – *Back panel of General Simplex Fit program*

Back panel of program for output of fit parameters and data visualization.

5.1.4.3 Output for model fit

Once all of the necessary information is place in the input fields (see Section 5.1.4.2), turning on the "**Enter Data**" toggle (see **10** in **Figure 5.3**) switches to the back panel (**Figure 5.4**). Once on this panel, activate the "**Start Fit**" toggle (see **1** in **Figure 5.4**). If the setting for "**Monte Carlo N**" is 1, then all of the data sets will be displayed in the plot window (see **2** in **Figure 5.4**). When there are multiple data sets, the "**Data ID**" knob (see **3** in **Figure 5.4**) allows the user to switch the data set being displayed in the plot window. If the setting for "**Monte Carlo N**" is 2, then the values for the optimized

parameters will be displayed in the "**Parameters Solution**" output display (see **4** in **Figure 5.4**). Any "**Monte Carlo N**" setting greater than 2 will initiate fits on the original data and on the N-2 simulated data sets. The "**Current N**" indicator displays how many simulated data sets have been fit so far (see **5** in **Figure 5.4**). Once this has reached N-1, the fitting is done and the results for the optimized parameters and their respective confidence intervals are displayed in the "**Parameters**" output display. Once the fitting is done, you can return to the front panel by toggling the "**Restart Fit**" switch (see **6** in **Figure 5.4**). At this point you can enter different values in any of the input fields except for the "**path for data file**" field. To input a new data set, the main vi has to be stopped first.

5.2 Model for Myosin Detachment from Actin Through a Force-dependent or –independent Pathway

In the model for myosin detachment from actin given in **Scheme 6** of Section 2.3.2.2, there is a force-dependent and a force-independent path from the attached to the detached state. The probabilities of being in the attached and detached state are expressed as p_a and p_d, respectively. Given that the rate of detachment for the force dependent path is k_g and that of the force independent path is k_i, the rate equation is written as:

$$\frac{d}{dt}p_a(t) = -k_g \cdot p_a(t) - k_i \cdot p_a(t) = -\left(k_g + k_i\right) \cdot p_a(t)$$

5.2.1

As a homogenous linear differential equation, the solution of this is straightforward:

$$p_a(t) = e^{-k_{obs} \cdot t}$$

5.2.2

where k_{obs} is defined as:

$$k_{obs} = k_g + k_i$$

5.2.3

Since k_g is force-dependent (see **Scheme 6**), this is described by the Bell Equation (**106**, **107**):

$$k_g(F) = k_{g0} e^{\left(\frac{F \cdot d}{k_B T}\right)}$$

5.2.4 – Bell Equation

where F is the applied force, k_{g0} is the value of k_g at zero force, and d is the distance parameter. Replacing equation 5.2.4 with k_g in equation 5.2.3 leads to the expression:

$$k_{obs}(F) = k_{g0} e^{\left(\frac{F \cdot d}{k_B T}\right)} + k_i$$

5.2.5

Using the Maximum Likelihood Estimation described in Section 5.2 requires expressing equation 5.2.2 as a probability distribution function (pdf), P_a:

$$P_a(t) = \int_0^t p_a(t) dt = \int_0^t e^{-k_{obs} \cdot t} dt$$

5.2.6

the solution of which is:

$$P_a(t) = -\frac{1}{k_{obs}} \cdot e^{-k_{obs} \cdot t}$$

5.2.7

A principal feature of a pdf is that the area under the curve of a pdf such as equation 5.2.7 is equal to one, which is expressed mathematically as:

$$\int_0^\infty p_a(t)dt = 1 \qquad \textbf{5.2.8}$$

which equation 5.2.7 satisfies.

5.3 Calcium Binding Rate Equations and Derivations

Presented here are derivations of rate equations based on speculations on kinetic mechanisms for various processes discussed in Section 2. These equations were not used for any published analysis, so this section should be taken as instructional for those wishing to derive rate equations based on their own mechanisms

5.3.1 Calcium binding to nucleotide-free myo1b^{IQ}

Here we present a two calcium binding model to describe the calcium-dependent increase of tryptophan fluorescence described in Section 2.3.4.6 (**Figure 2.20**). The simplest model that was consistent with the data was one assuming two rapid calcium binding events that lead to a conformational change:

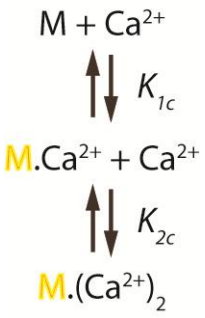

Scheme 7

where "M" indicates myosin and K_{1c} and K_{2c} are the affinities for the first and second calcium binding events, respectively. The increase in tryptophan fluorescence was assumed to occur after the final step in the pathway, as indicated by the highlighted "M". The total steady state fluorescence can be calculated according to the following:

$$\mathrm{A}_{Tot} \cdot [\mathrm{M}_{Tot}] = \mathrm{A}_0 \cdot [\mathrm{M}] + \mathrm{A}_1 \cdot ([\mathrm{MCa}^{2+}] + [\mathrm{M(Ca}^{2+})_2])$$

5.3.1

Where A_0 and A_1 represent fluorescent states characteristic of different states of calcium bound myosin and A_{Tot} is the total observed fluorescence at a given concentration of calcium. This expression can be simplified by calculating the chemical species assuming steady state conditions. The equations for these species are:

$$[\mathrm{M}] = \frac{K_{1c}K_{2c} \cdot [\mathrm{M}_{Tot}]}{K_{1c}K_{2c} + K_{2c}[\mathrm{Ca}^{2+}] + [\mathrm{Ca}^{2+}]^2}$$

5.3.2

$$[\mathrm{MCa}^{2+}] = \frac{K_{2c}[\mathrm{Ca}^{2+}] \cdot [\mathrm{M}_{Tot}]}{K_{1c}K_{2c} + K_{2c}[\mathrm{Ca}^{2+}] + [\mathrm{Ca}^{2+}]^2}$$

5.3.3

$$[\mathrm{M(Ca}^{2+})_2] = \frac{[\mathrm{Ca}^{2+}]^2 \cdot [\mathrm{M}_{Tot}]}{K_{1c}K_{2c} + K_{2c}[\mathrm{Ca}^{2+}] + [\mathrm{Ca}^{2+}]^2}$$

5.3.4

where $[M_{Tot}]$ represents the total concentration of myo1b^{IQ} present and K_{1c} and K_{2c} are the dissociation constants for calcium binding. Plugging these equations into equation 5.3.1 yields:

$$A_{Tot} = \frac{A_0 \cdot K_{1c}K_{2c} + A_1 \cdot (K_{2c}[Ca^{2+}] + [Ca^{2+}]^2)}{K_{1c}K_{2c} + K_{2c}[Ca^{2+}] + [Ca^{2+}]^2}$$

5.3.5

This can be normalized by dividing the total fluorescence (A_{Tot}) by the fluorescence at t = 0, when $[M_{Tot}] = [M]$ and $A_{Tot} = A_0$. This yields:

$$A^*_{Tot} = \frac{K_{1c}K_{2c} + A^*_1 \cdot (K_{2c}[Ca^{2+}] + [Ca^{2+}]^2)}{K_{1c}K_{2c} + K_{2c}[Ca^{2+}] + [Ca^{2+}]^2}$$

5.3.6

This is further simplified by subtracting one from both sides, which leads to the expression:

$$A'_{Tot}([Ca^{2+}]) = \frac{A'_1 \cdot (K_{2c}[Ca^{2+}] + [Ca^{2+}]^2)}{K_{1c}K_{2c} + K_{2c}[Ca^{2+}] + [Ca^{2+}]^2}$$

5.3.7

where $A`_{Tot}$ and $A`_1$ are defined as:

$$A'_{Tot} = \frac{A_{Tot}}{A_0} - 1$$

$$A'_1 = \frac{A_1}{A_0} - 1$$

5.3.8

5.3.2 Calcium binding to myo1b^{IQ} undergoing phosphate release

The calcium binding event that affects phosphate release is modeled as a two-step sequential process as shown in Scheme 8:

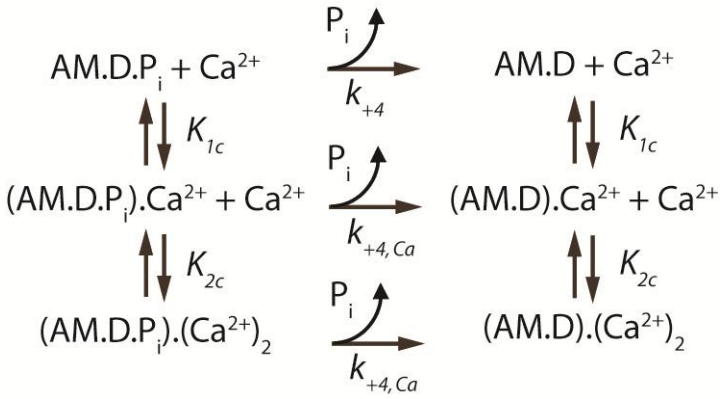

Scheme 8

where "AM" is actomyosin, "D" is ADP, "P_i" is inorganic phosphate and K_{1c} and K_{2c} are the affinities of the first and second calcium binding events, respectively. In this model, we assumed that myo1b^{IQ} releases P_i at the base rate of k_{+4} until calcium binds, at which point it releases P_i at a rate of $k_{+4,Ca}$. In this experiment we were monitoring the increase in free phosphate, so we were interested in determining the time course of the production of P_i. In order to do this, we had to solve the equation describing the rate of production of P_i (equation 5.3.9):

$$\frac{d}{dt}[\mathrm{P}_i](t) = k_{+4}[\mathrm{AM.D.P}_i](t) + k_{+4,Ca}\left([(\mathrm{AM.D.P}_i).\mathrm{Ca}^{2+}](t) + [(\mathrm{AM.D.P}_i).(\mathrm{Ca}^{2+})_2](t)\right)$$

5.3.9

We make the further assumption that calcium binding occurs very fast, so that by the time measurement begins (t ~ 0), the calcium bound chemical species are at their steady state concentrations. We also note that since the concentration of myo1b^{IQ} (5uM) is much greater than that of ATP (1uM), this experiment monitors a single turnover of the ATP. From this, the assumption of rapid equilibrium, and from the calcium binding model given in Scheme 9 we are able to derive expressions for the chemical species [AM.D.P_i], [(AM.D.P_i).Ca^{2+}], [(AM.D.P_i).$(Ca^{2+})_2$] from equation 5.3.9:

$$[\mathrm{AM.D.P}_i](t) = \frac{K_{1c}K_{2c} \cdot \left([\mathrm{P}_{Tot}] - [\mathrm{P}_i](t)\right)}{K_{1c}K_{2c} + K_{2c}[\mathrm{Ca}^{2+}] + [\mathrm{Ca}^{2+}]^2}$$

5.3.10

$$[(\mathrm{AM.D.P}_i).\mathrm{Ca}^{2+}](t) = \frac{K_{2c}[\mathrm{Ca}^{2+}] \cdot \left([\mathrm{P}_{Tot}] - [\mathrm{P}_i](t)\right)}{K_{1c}K_{2c} + K_{2c}[\mathrm{Ca}^{2+}] + [\mathrm{Ca}^{2+}]^2}$$

5.3.11

$$[(\mathrm{AM.D.P}_i).(\mathrm{Ca}^{2+})_2](t) = \frac{[\mathrm{Ca}^{2+}]^2 \cdot \left([\mathrm{P}_{Tot}] - [\mathrm{P}_i](t)\right)}{K_{1c}K_{2c} + K_{2c}[\mathrm{Ca}^{2+}] + [\mathrm{Ca}^{2+}]^2}$$

5.3.12

Inserting these expressions into equation 5.3.9 yields the expression:

$$\frac{d}{dt}[\mathrm{P}_i] = \left(\frac{k_{+4}K_{1c}K_{2c} + k_{+4,Ca}(K_{2c}[\mathrm{Ca}^{2+}] + [\mathrm{Ca}^{2+}]^2)}{K_{1c}K_{2c} + K_{2c}[\mathrm{Ca}^{2+}] + [\mathrm{Ca}^{2+}]^2}\right) \cdot ([\mathrm{P}_{Tot}] - [\mathrm{P}_i])$$

5.3.13

where $[P_{Tot}]$ is defined by adding together all chemical species containing P_i:

$$[P_{Tot}] = [P_i] + [AM.D.P_i] + [(AM.D.P_i).Ca^{2+}] + [(AM.D.P_i).(Ca^{2+})_2]$$

5.3.14

This is a linear, inhomogeneous differential equation, which can be solved analytically. Doing so provides a precise expression for the time dependence of P_i production:

$$[P_i](t) = [P_{Tot}] \cdot (1 - e^{-k_{obs} \cdot t})$$

5.3.15

where k_{obs} is the calcium dependent observed rate of P_i release, which is defined as:

$$k_{obs}([Ca^{2+}]) = \frac{k_{+4}K_{1c}K_{2c} + k_{+4,Ca}(K_{2c}[Ca^{2+}] + [Ca^{2+}]^2)}{K_{1c}K_{2c} + K_{2c}[Ca^{2+}] + [Ca^{2+}]^2}$$

5.3.16

5.3.3 Calcium-dependent steady state ATPase rate of myo1b^{IQ}

Since P_i release is the rate limiting step in the ATPase cycle, under steady state conditions this rate equals the ATPase rate. Therefore, the steady state rate equation can be derived from equation 5.3.9 using the following steady state assumptions:

$$\frac{d}{dt}[\mathrm{P}_i](t) \neq 0$$

$$\frac{d}{dt}[\mathrm{AM.D.P}_i](t) = 0$$

$$\frac{d}{dt}[(\mathrm{AM.D.P}_i).\mathrm{Ca}^{2+}](t) = 0$$

$$\frac{d}{dt}[(\mathrm{AM.D.P}_i).(\mathrm{Ca}^{2+})_2](t) = 0$$

5.3.17

This means that under steady state conditions the chemical species [AM.D.P_i], [(AM.D.P_i).Ca^{2+}], [(AM.D.P_i).(Ca^{2+})$_2$] from equation 5.3.9 will remain constant. Since these species are formed just before the rate limiting phosphate release step, they will be the predominant form of the total myo1b^{IQ} (M_{Tot}) at steady state:

$$[\mathrm{M}_{Tot}] = [\mathrm{AM.D.P}_i] + [(\mathrm{AM.D.P}_i).\mathrm{Ca}^{2+}] + [(\mathrm{AM.D.P}_i).(\mathrm{Ca}^{2+})_2]$$

5.3.18

Again using Scheme 9, we can calculate the steady state concentrations of [AM.D.P_i], [(AM.D.P_i).Ca^{2+}], and [(AM.D.P_i).(Ca^{2+})$_2$] relative to the total myo1b^{IQ} concentration, [M_{Tot}]:

$$[\mathrm{AM.D.P}_i] = \frac{K_{1c}K_{2c} \cdot [\mathrm{M}_{Tot}]}{K_{1c}K_{2c} + K_{2c}[\mathrm{Ca}^{2+}] + [\mathrm{Ca}^{2+}]^2}$$

5.3.19

$$[(\mathrm{AM.D.P}_i).\mathrm{Ca}^{2+}] = \frac{K_{2c}[\mathrm{Ca}^{2+}] \cdot [\mathrm{M}_{Tot}]}{K_{1c}K_{2c} + K_{2c}[\mathrm{Ca}^{2+}] + [\mathrm{Ca}^{2+}]^2}$$

5.3.20

$$[(\mathrm{AM.D.P}_i).(\mathrm{Ca}^{2+})_2] = \frac{[\mathrm{Ca}^{2+}]^2 \cdot [\mathrm{M}_{Tot}]}{K_{1c}K_{2c} + K_{2c}[\mathrm{Ca}^{2+}] + [\mathrm{Ca}^{2+}]^2}$$

5.3.21

Note that these expressions are very similar to those given in equations 5.3.10 - 5.3.12, except that these are independent of P_i concentration and constant over all time. Substituting these into equation 5.3.9 and simplifying gives the steady state rate equation for P_i release:

$$\frac{d}{dt}[\mathrm{P}_i](t) = \left(\frac{k_{+4}K_{1c}K_{2c} + k_{+4,Ca}(K_{2c}[\mathrm{Ca}^{2+}] + [\mathrm{Ca}^{2+}]^2)}{K_{1c}K_{2c} + K_{2c}[\mathrm{Ca}^{2+}] + [\mathrm{Ca}^{2+}]^2}\right) \cdot [\mathrm{M}_{Tot}]$$

5.3.22

Since $[M_T]$ is a constant, and $[P_i] = 0$ at $t = 0$, the solution of this is trivial:

$$[\mathrm{P}_i](t) = \left(\frac{k_{+4}K_{1c}K_{2c} + k_{+4,Ca}(K_{2c}[\mathrm{Ca}^{2+}] + [\mathrm{Ca}^{2+}]^2)}{K_{1c}K_{2c} + K_{2c}[\mathrm{Ca}^{2+}] + [\mathrm{Ca}^{2+}]^2}\right) \cdot t$$

5.3.23

As expected, the observed steady state rate at different calcium concentrations can be expressed by the same equation as for the transient case.

5.3.4 Calcium binding to myo1b^{IQ} undergoing ADP release

The calcium binding event that affects ADP release is modeled as a two-step sequential process as shown in Scheme 9:

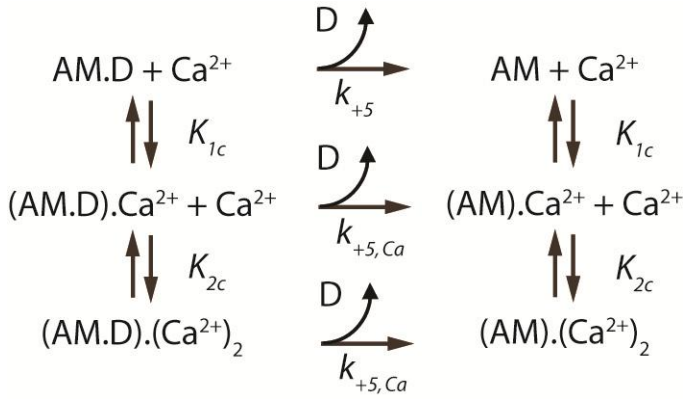

Scheme 9

where "AM" is actomyosin, "D" is ADP and K_{1c} and K_{2c} are the affinities of the first and second calcium binding events, respectively. In this model, we assumed that myo1b^{IQ} releases ADP at the base rate of k_{+5} until calcium binds, at which point it releases ADP at a rate of $k_{+5,Ca}$. In this experiment we were monitoring the increase in fluorescence from the unquenched pyrene actin after ATP-bound myo1b^{IQ} dissociates. Since myo1b^{IQ} is pre-equilibrated in a high concentration of ADP (30 μM), the resulting transient is composed of two exponentials: one with a slow rate associated with ADP release and the other with a combined rate associated with ATP binding. To calculate the calcium dependence of this slow rate, we solve the equation describing the rate of production of ADP (D) (equation 5.3.24):

$$\frac{d}{dt}[\mathrm{ADP}](t) = k_{+5}[\mathrm{AM.D}](t) + k_{+5,Ca}\left([(\mathrm{AM.D}).\mathrm{Ca}^{2+}](t) + [(\mathrm{AM.D}).(\mathrm{Ca}^{2+})_2](t)\right)$$

5.3.24

We make the further assumption that calcium binding occurs very fast, so that by the time measurement begins (t ~ 0), the calcium bound chemical species are at their steady state concentrations. From the assumption of rapid equilibrium, and from the calcium binding model given in Scheme 10 we are able to derive expressions for the chemical species [AM.D], [(AM.D).Ca^{2+}], [(AM.D).$(Ca^{2+})_2$] from equation 5.3.24:

$$[\mathrm{AM.D}](t) = \frac{K_{1c}K_{2c} \cdot \left([\mathrm{ADP}_{Tot}] - [\mathrm{ADP}](t)\right)}{K_{1c}K_{2c} + K_{2c}[\mathrm{Ca}^{2+}] + [\mathrm{Ca}^{2+}]^2}$$

5.3.25

$$[(\mathrm{AM.D}).\mathrm{Ca}^{2+}](t) = \frac{K_{2c}[\mathrm{Ca}^{2+}] \cdot \left([\mathrm{ADP}_{Tot}] - [\mathrm{ADP}](t)\right)}{K_{1c}K_{2c} + K_{2c}[\mathrm{Ca}^{2+}] + [\mathrm{Ca}^{2+}]^2}$$

5.3.26

$$[(\mathrm{AM.D}).(\mathrm{Ca}^{2+})_2](t) = \frac{[\mathrm{Ca}^{2+}]^2 \cdot \left([\mathrm{ADP}_{Tot}] - [\mathrm{ADP}](t)\right)}{K_{1c}K_{2c} + K_{2c}[\mathrm{Ca}^{2+}] + [\mathrm{Ca}^{2+}]^2}$$

5.3.27

Inserting these expressions into equation 5.3.24 yields the expression:

$$\frac{d}{dt}[\mathrm{ADP}] = \left(\frac{k_{+4}K_{1c}K_{2c} + k_{+4,Ca}(K_{2c}[\mathrm{Ca}^{2+}] + [\mathrm{Ca}^{2+}]^2)}{K_{1c}K_{2c} + K_{2c}[\mathrm{Ca}^{2+}] + [\mathrm{Ca}^{2+}]^2}\right) \cdot \left([\mathrm{ADP}_{Tot}] - [\mathrm{ADP}](t)\right)$$

5.3.28

where $[\mathrm{ADP}_{\mathrm{Tot}}]$ is defined by adding together all chemical species containing ADP:

$$[\mathrm{ADP}_{Tot}] = [\mathrm{ADP}] + [\mathrm{AM.D}] + [(\mathrm{AM.D}).\mathrm{Ca}^{2+}] + [(\mathrm{AM.D}).(\mathrm{Ca}^{2+})_2]$$

5.3.29

This is a linear, inhomogeneous differential equation, which can be solved analytically. Doing so provides a precise expression for the time dependence of P_i production:

$$[\mathrm{ADP}](t) = [\mathrm{ADP}_{Tot}] \cdot (1 - e^{-k_{obs} \cdot t})$$

5.3.30

where k_{obs} is the calcium dependent observed rate of ADP release, which is defined as:

$$k_{obs}([\mathrm{Ca}^{2+}]) = \frac{k_{+5}K_{1c}K_{2c} + k_{+5,Ca}(K_{2c}[\mathrm{Ca}^{2+}] + [\mathrm{Ca}^{2+}]^2)}{K_{1c}K_{2c} + K_{2c}[\mathrm{Ca}^{2+}] + [\mathrm{Ca}^{2+}]^2}$$

5.3.31

It should be noted that equation 5.3.31 is identical in form to that given in equation 5.3.16 and differs only in the rates being influenced (k_{+5} vs. k_{+4}).

5.4 Derivations of Equations for Transforming the Orientation of the Probe to that of the Lever-arm

5.4.1 Derivation of Expression for the Orientation of the Probe Relative to Actin (α_P, β_P) as a Function of the Lever-arm Orientation (α_L, β_L) and Probe Orientation Relative to the Lever-arm Frame (θ_P, φ_P)

The intensities measured in our experiments are used to calculate the orientation of the probe attached to myoV relative to the laboratory frame of reference (θ_{lab}, φ_{lab}), which we then transform to the actin reference frame (α_P, β_P). The orientation of the probe can also be described relative to the frame of the lever-arm (θ_P, φ_P), whose orientation is itself measured relative to the actin frame (α_L, β_L) (**Figure 3.2B** and Section 3.3 for description).

In deriving an expression relating the orientations relative to the actin frame of the probe to the lever-arm, we note that this expression must also account for the orientation of the probe relative to the frame of the lever-arm. We therefore start our derivation by constructing the rotation matrix ${}^{A}\mathbf{R}^{P}$ which is derived from four separate rotation operations that rotates the probe frame (P) to the actin frame (A) (**Figure 5.5**). The combined rotation matrix ${}^{A}\mathbf{R}^{P}$ is derived by multiplying together the four rotation matrices. We describe rotations as positive or negative if the rotation is right- or left-handed, respectively. The first two rotations that align the z_A-axis with the lever-arm are performed so that the resulting axes are consistent with our definition of the lever-arm

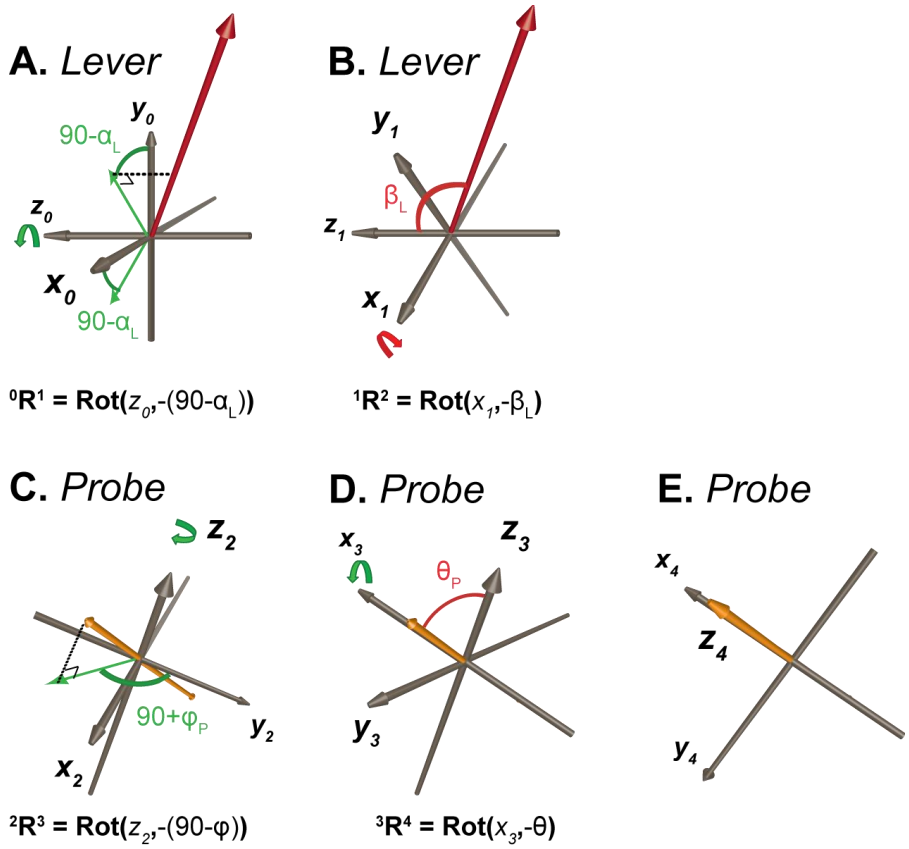

Figure 5.5 – *Rotation Scheme.*

A. *Lever in actin frame*: Counterclockwise rotation of x_0-y_0 plane about the z_0-axis by (90-α) degrees. **B.** *Lever in actin frame*: Counterclockwise rotation of y_1-z_1 plane about the x_1-axis by β degrees. C**.** *Probe in lever frame*: Counterclockwise rotation of x_2-y_2 plane about the z_2-axis by (90-ϕ) degrees. **D.** *Probe in lever frame*: Counterclockwise rotation of y_3-z_3 plane about the x_3-axis by θ degrees. **E.** *Probe in Probe frame*: Probe is now oriented with the z_4-axis of the Probe frame of reference.

frame of reference (see **Figure 3.2B** and Section 3.3).These initial rotations are performed on the actin frame of reference, defined by the axes x_0, y_0, and z_0 (where $x_0 = x_A$, $y_0 = y_A$ and $z_0 = z_A$; see **Figure 5.5A**). The first rotation matrix describes the negative rotation of these axes about the z_0 axis by an amount equal to $(\pi/2 - \alpha_L)$, so that the y_0-axis is aligned with the projection of the lever-arm that lies in the x_0-y_0 plane perpendicular to the actin filament:

$$ {}^{0}\mathbf{R}^{1} = Rot\left(z_0, -\left(\frac{\pi}{2} - \alpha_L\right)\right) = \begin{bmatrix} \sin\alpha_L & \cos\alpha_L & 0 \\ -\cos\alpha_L & \sin\alpha_L & 0 \\ 0 & 0 & 1 \end{bmatrix} $$

5.4.1

This rotation results in a coordinate frame defined by x_1, y_1 and z_1, where $z_1 = z_0$ (see **Figure 5.5B**). The second rotation matrix describes the negative rotation about the x_1 axis by an amount equal to β_L, so that the z_1-axis is aligned with the Lever vector:

$$ {}^{1}\mathbf{R}^{2} = Rot(x_1, -\beta_L) = \begin{bmatrix} 1 & 0 & 0 \\ 0 & \cos\beta_L & \sin\beta_L \\ 0 & -\sin\beta_L & \cos\beta_L \end{bmatrix} $$

5.4.2

This rotation results in a coordinate frame defined by x_2, y_2 and z_2, where $x_2 = x_1 = x_L$, $y_2 = y_L$, and $z_2 = z_L$, where the x_L, y_L and z_L-axes describe the lever-arm frame of reference (see **Figure 5.5C** and **Figure 3.2B**). The third rotation matrix describes the negative rotation about the z_2-axis by an amount equal to $(\pi/2 - \varphi_P)$, so that the y_2-axis is aligned with the projection of the probe that lies in the x_3-y_3 plane perpendicular to the lever-arm:

$$ {}^{2}\mathbf{R}^{3} = Rot\left(z_2, -\left(\frac{\pi}{2} - \varphi_P\right)\right) = \begin{bmatrix} \sin\varphi_P & \cos\varphi_P & 0 \\ -\cos\varphi_P & \sin\varphi_P & 0 \\ 0 & 0 & 1 \end{bmatrix} $$

5.4.3

This rotation results in a coordinate frame defined by x_3, y_3 and z_3, where $z_3 = z_2$ (see **Figure 5.5D**). The final rotation matrix describes the negative rotation about the x_3 axis by an amount equal to θ_P, so that the z_3-axis is aligned with the probe vector:

$$^{3}\mathbf{R}^{4} = Rot(x_3, -\theta_P) = \begin{bmatrix} 1 & 0 & 0 \\ 0 & \cos\theta_P & \sin\theta_P \\ 0 & -\sin\theta_P & \cos\theta_P \end{bmatrix}$$

5.4.4

The total rotation operation is described by:

$$^{A}\mathbf{R}^{P} = {}^{0}\mathbf{R}^{4} = {}^{0}\mathbf{R}^{1} \cdot {}^{1}\mathbf{R}^{2} \cdot {}^{2}\mathbf{R}^{3} \cdot {}^{3}\mathbf{R}^{4}$$

5.4.5

The result of this last rotational operation is that the z_3-axis is aligned with the vector of the probe $\vec{\mathbf{v}}_P$ (**Figure 5.5E**), where the $x_4 = x_P$, $y_4 = y_P$ and $z_4 = z_P$-axes represent a probe frame of reference. In the probe frame, $\vec{\mathbf{v}}_P$ is a unit vector aligned with the z_4-axis:

$$\vec{\mathbf{v}}_P = \begin{pmatrix} v_{x_P} \\ v_{y_P} \\ v_{z_P} \end{pmatrix} = \begin{pmatrix} 0 \\ 0 \\ 1 \end{pmatrix}$$

5.4.6

This vector $\vec{\mathbf{v}}_P$, defined in the probe frame (P), can be redefined in the actin frame (A) as the vector $\vec{\mathbf{v}}_A$ by multiplying it by the rotation matrix $^{A}\mathbf{R}^{P}$ (Equation 5.4.5):

$$\begin{pmatrix} v_{x_A} \\ v_{y_A} \\ v_{z_A} \end{pmatrix} = \vec{\mathbf{v}}_A = {}^A\mathbf{R}^P \cdot \vec{\mathbf{v}}_P$$

5.4.7

This is converted to α_P and β_P using the following trigonometric relationships:

$$\alpha_P = \text{atan2}\left(v_{x_P}, v_{y_P}\right)$$

5.4.8

$$\beta_P = \text{acos}\left(v_{z_P}\right)$$

5.4.9

Solving the above relationships, we find the two expressions for α_P and β_P as functions of α_L, β_L, θ_P, and φ_P:

$$\beta_P(\theta_P, \varphi_P, \beta_L) = \text{acos}(-\sin\beta_L \cdot \sin\theta_P \cdot \sin\varphi_P + \cos\beta_L \cdot \cos\theta_P)$$

5.4.10 - β_p equation

where the range of β_P is defined as:

$$0 \leq \beta_P \leq \pi$$

5.4.11

$$\alpha_P(\theta_P, \varphi_P, \alpha_L, \beta_L)$$

$$= \operatorname{atan2}([(\sin\alpha_L \cdot \cos\varphi_P + \cos\alpha_L \cdot \cos\beta_L \cdot \sin\varphi_P) \cdot \sin\theta_P + \cos\alpha_L \cdot \sin\beta_L \cdot \cos\theta_P],$$

$$[(-\cos\alpha_L \cdot \cos\varphi_P + \sin\alpha_L \cdot \cos\beta_L \cdot \sin\varphi_P) \cdot \sin\theta_P + \sin\alpha_L \cdot \sin\beta_L \cdot \cos\theta_P])$$

5.4.12 - α_P equation

where the range of α_P is defined as:

$$-\pi \leq \alpha_P \leq \pi$$

5.4.13

and the atan2(x, y) function is similar to the standard arctan(y/x) function except that atan2(x, y) is single valued over a larger range ($-\pi \leq \alpha_P \leq \pi$ for atan2(x,y) and $-{}^{\pi}/_{2} \leq \alpha_P \leq {}^{\pi}/_{2}$ for arctan(y/x)).

5.4.2 Derivation of Expression for Lever-arm Orientation Relative to Actin (α_L, β_L) as a Function of the Probe Orientation Relative to Actin (α_P, β_P) and Relative to the Lever-arm (θ_P, φ_P).

We wish to find an expression for the orientation of the lever-arm in terms of the orientation of the probe, both in relation to the actin frame of reference (x_A, y_A, z_A). We derive the lever arm angles by finding the inverse functions for equations 5.4.10 and 5.4.12.

We start by rearranging equation 5.4.10:

$$-\sin\beta_L \cdot \sin\theta_P \cdot \sin\varphi_P = \cos\beta_L \cdot \cos\theta_P - \cos\beta_P$$

5.4.14

$$(-\sin\beta_L \cdot \sin\theta_P \cdot \sin\varphi_P)^2 = (\cos\beta_L \cdot \cos\theta_P - \cos\beta_P)^2$$

5.4.15

$$(1-\cos{\beta_L}^2)\cdot \sin{\theta_P}^2 \cdot \sin{\varphi_P}^2$$
$$= \cos{\beta_L}^2 \cdot \cos{\theta_P}^2 + \cos{\beta_P}^2 - 2\cdot(\cos\beta_L \cdot \cos\theta_P \cdot \cos\beta_P)$$

5.4.16

$$\cos{\beta_L}^2 \cdot (\cos{\theta_P}^2 + \sin{\theta_P}^2 \cdot \sin{\varphi_P}^2) - \cos\beta_L \cdot (2\cdot\cos\theta_P \cdot \cos\beta_P)$$
$$+ (\cos{\beta_P}^2 - \sin{\theta_P}^2 \cdot \sin{\varphi_P}^2) = 0$$

5.4.17

We find an expression for β_L using the quadratic formula:

$$\beta_L(\theta_P, \varphi_P, \beta_P)$$
$$= \operatorname{acos}\left(\frac{\cos\theta_P \cdot \cos\beta_P \pm \sqrt{\sin{\theta_P}^2 \cdot \sin{\varphi_P}^2 \cdot (\sin{\beta_P}^2 - \sin{\theta_P}^2 \cdot \cos{\varphi_P}^2)}}{\cos{\theta_P}^2 + \sin{\theta_P}^2 \cdot \sin{\varphi_P}^2}\right)$$

5.4.18 - β_L equation

where the range of β_L is defined as:

$$0 \leq \beta_L \leq \pi$$

5.4.19

To solve for α_L, we start by rearranging equation 5.4.12:

$$\tan \alpha_P = \frac{(-\cos \varphi_P + \tan \alpha_L \cdot \cos \beta_L \cdot \sin \varphi_P) \cdot \sin \theta_P + \tan \alpha_L \cdot \sin \beta_L \cdot \cos \theta_P}{(\tan \alpha_L \cdot \cos \varphi_P + \cos \beta_L \cdot \sin \varphi_P) \cdot \sin \theta_P + \sin \beta_L \cdot \cos \theta_P}$$

5.4.20

$$\tan \alpha_L \cdot (\sin \theta_P \cdot \tan \alpha_P \cdot \cos \varphi_P - \sin \theta_P \cdot \cos \beta_L \cdot \sin \varphi_P - \sin \beta_L \cdot \cos \theta_P) = \tan \alpha_P \cdot (\sin \theta_P \cdot \cos \beta_L \cdot \sin \varphi_P + \sin \beta_L \cdot \cos \theta_P) - \sin \theta_P \cdot \tan \alpha_P \cdot \cos \varphi_P$$

5.4.21

Rearranging this yields an expression for α_L:

$$\alpha_L(\theta_P, \varphi_P, \alpha_P, \beta_P) = \operatorname{atan2}\Big(\big[\big(\cos\big(\beta_L(\theta_P, \varphi_P, \beta_P)\big) \cdot \sin \varphi_P \cdot \sin \theta_P + \sin\big(\beta_L(\theta_P, \varphi_P, \beta_P)\big) \cdot \cos \theta_P\big) \cdot \cos \alpha_P - \sin \theta_P \cdot \cos \varphi_P \cdot \sin \alpha_P\big], \big[\big(\cos\big(\beta_L(\theta_P, \varphi_P, \beta_P)\big) \cdot \sin \varphi_P \cdot \sin \theta_P + \sin\big(\beta_L(\theta_P, \varphi_P, \beta_P)\big) \cdot \cos \theta_P\big) \cdot \sin \alpha_P \cdot \cos \varphi_P + \sin \theta_P \cdot \cos \varphi_P \cdot \cos \alpha_P\big]\Big)$$

5.4.22 - α_L equation

where the range of α_L is defined as:

$$-\pi \leq \alpha_L \leq \pi$$

5.4.23

5.4.3 Derivation of Expression for the Probe Orientation Relative to the Lever (θ_P, φ_P) as a Function of the Probe (α_P, β_P) and Lever (α_L, β_L) Orientations Relative to Actin

We wish to find an expression for the orientation of the probe relative to the lever-arm in terms of the lever and probe orientations in the actin frame of reference (x_A, y_A, z_A). We derive the probe angles (θ_P, φ_P) by finding the inverse functions for equations 5.4.10 and 5.4.12.

We start by rearranging equation 5.4.10:

$$-\sin\beta_L \cdot \sin\theta_P \cdot \sin\varphi_P = \cos\beta_L \cdot \cos\theta_P - \cos\beta_P$$

5.4.24

$$\sin\varphi_P = \frac{\cos\beta_P - \cos\beta_L \cdot \cos\theta_P}{\sin\beta_L \cdot \sin\theta_P}$$

5.4.25

resulting in an expression for φ_P as a function of α_P, β_P, and β_L :

$$\varphi_P(\theta_P, \beta_P, \beta_L) = \operatorname{asin}\left(\frac{\cos\beta_P - \cos\beta_L \cdot \cos\theta_P}{\sin\beta_L \cdot \sin\theta_P}\right)$$

5.4.26 - φ_P Equation

where the range of φ_P is defined as:

$$-\pi \leq \varphi_P \leq \pi$$

5.4.27

To solve for θ_P, we start by rearranging equation 5.4.12:

$$\tan \alpha_P = \frac{(-\cos \varphi_P + \tan \alpha_L \cdot \cos \beta_L \cdot \sin \varphi_P) \cdot \tan \theta_P \ + \tan \alpha_L \cdot \sin \beta_L}{(\tan \alpha_L \cdot \cos \varphi_P + \cos \beta_L \cdot \sin \varphi_P) \cdot \tan \theta_P \ + \sin \beta_L}$$

5.4.28

$$\tan \alpha_P \cdot \big((\tan \alpha_L \cdot \cos \varphi_P + \cos \beta_L \cdot \sin \varphi_P) \cdot \tan \theta_P \ + \sin \beta_L\big)$$
$$= (-\cos \varphi_P + \tan \alpha_L \cdot \cos \beta_L \cdot \sin \varphi_P) \cdot \tan \theta_P \ + \tan \alpha_L \cdot \sin \beta_L$$

5.4.29

$$\tan \theta_P \ \cdot \big(\tan \alpha_P \cdot (\tan \alpha_L \cdot \cos \varphi_P + \cos \beta_L \cdot \sin \varphi_P)$$
$$+ (\cos \varphi_P - \tan \alpha_L \cdot \cos \beta_L \cdot \sin \varphi_P)\big) = \tan \alpha_L \cdot \sin \beta_L - \tan \alpha_P \cdot \sin \beta_L$$

5.4.30

$$\tan \theta_P$$
$$= \frac{\tan \alpha_L \cdot \sin \beta_L - \tan \alpha_P \cdot \sin \beta_L}{\big(\tan \alpha_P \cdot (\tan \alpha_L \cdot \cos \varphi_P + \cos \beta_L \cdot \sin \varphi_P) + (\cos \varphi_P - \tan \alpha_L \cdot \cos \beta_L \cdot \sin \varphi_P)\big)}$$

5.4.31

Rearranging this yields an expression for θ_P as a function of α_P, β_P, α_L, and β_L:

$$\theta_P(\varphi_P, \alpha_P, \alpha_L, \beta_L)$$

$$= \text{atan2}([\cos\varphi_P \cdot (1 + \tan\alpha_L \cdot \tan\alpha_P) - (\tan\alpha_L - \tan\alpha_P) \cdot \cos\beta_L$$

$$\cdot \sin\varphi_P], [\sin\beta_L \cdot (\tan\alpha_L - \tan\alpha_P)])$$

5.4.32 - θ_P Equation

where the range of θ_P is defined as:

$$0 \leq \theta_P \leq \pi$$

5.4.33

5.4.4 Relationship establishing equality between $^2\Delta\alpha_P$ and $^2\Delta\alpha_L$

We consider the probe at the two angular states *n* and *n* + *m*:

$$n = 0, 1, 2 \ldots N - m$$

5.4.34

$$m = 0, 1, 2 \ldots N - n$$

5.4.35

where N = n + m and is the total number of angular states. If:

$$\beta_{P,n} = \beta_{P,n+m}$$

5.4.36

when *m* is even, then the lever-arm is confined to the same plane as the probe. Since the probe is rigidly attached to a single calmodulin bound to the lever-arm (see Materials and Methods), θ_P and φ_P are constant over all *n* and *m* time points in equations 5.4.10 and 5.4.12 such that:

$$\theta_{P,n} = \theta_{P,n+m}$$

5.4.37

$$\varphi_{P,n} = \varphi_{P,n+m}$$

5.4.38

It therefore follows that when conditions 5.4.36-5.4.38 are satisfied, then:

$$^{m}\Delta\alpha_P = {}^{m}\Delta\alpha_L$$

5.4.39 – $^{2}\Delta\alpha$ Identity

when *m* is even. The superscript *m* denotes the number of intervals in the difference so that:

$$^{m}\Delta\alpha_n = \alpha_n - \alpha_{n+m}$$

5.4.40

and

$$^{1}\Delta_n = \Delta_n$$

5.4.41

$$^{2}\Delta_n = \Delta_n + \Delta_{n+1}$$

5.4.42

$$^{m}\Delta_n = \Delta_n + \Delta_{n+1} + \cdots + \Delta_{n+(m-1)}$$

5.4.43

which can be more simply stated as:

$$^{m}\Delta_n = \sum_{i=0}^{m-1} \Delta_{n+i}$$

5.4.44

over all values of *m* and *n*. The expression given in Identity 5.4.39 can be explicitly derived by applying equation 5.4.10 to the expression given in 5.4.44, under the conditions given in 5.4.36-5.4.38. Using the trigonometric identity:

$$\tan(A - B) = \tan\left(\frac{\tan A - \tan B}{1 + \tan A \cdot \tan B}\right)$$

5.4.45

the expression $\tan(\alpha_{P,n} - \alpha_{P,n+m})$ simplifies to:

$$\tan(\alpha_{P,n} - \alpha_{P,n+m}) = \frac{\cos \alpha_{L,n} \cdot \sin \alpha_{L,n} - \cos \alpha_{L,n+m} \cdot \sin \alpha_{L,n+m}}{\cos^2 \alpha_{L,n} + \cos^2 \alpha_{L,n+m} - 1}$$

5.4.46

Through simple algebraic operations, this can be equivalently expressed as:

$$\tan\left(\alpha_{P,n} - \alpha_{P,n+m}\right) = \frac{\tan\alpha_{L,n} \cdot \sec^2\alpha_{L,n+m} - \tan\alpha_{L,n+m} \cdot \sec^2\alpha_{L,n}}{1 - \tan^2\alpha_{L,n} \cdot \tan^2\alpha_{L,n+m}}$$

5.4.47

Using the trigonometric identity:

$$\sec^2 A = 1 + \tan^2 A$$

5.4.48

the expression simplifies to:

$$\tan\left(\alpha_{P,n} - \alpha_{P,n+m}\right) = \frac{\tan\alpha_{L,n} \cdot \left(1 + \tan^2\alpha_{L,n+m}\right) - \tan\alpha_{L,n+m} \cdot \left(1 + \tan^2\alpha_{L,n}\right)}{1 - \tan^2\alpha_{L,n} \cdot \tan^2\alpha_{L,n+m}}$$

5.4.49

which can be equivalently expressed as:

$$\tan\left(\alpha_{P,n} - \alpha_{P,n+m}\right) = \frac{\tan\alpha_{L,n} - \tan\alpha_{L,n+m}}{1 + \tan\alpha_{L,n} \cdot \tan\alpha_{L,n+m}}$$

5.4.50

Using the trigonometric identity given in equation 5.4.45, we find that:

$$\tan\left(\alpha_{P,n} - \alpha_{P,n+m}\right) = \tan\left(\alpha_{L,n} - \alpha_{L,n+m}\right)$$

5.4.51

which is equivalent to:

$$\alpha_{P,n} - \alpha_{P,n+m} = \alpha_{L,n} - \alpha_{L,n+m}$$

5.4.52

when the tan function is single-valued, i.e.:

$$-\frac{\pi}{2} \leq (\alpha_n - \alpha_{n+m}) \leq \frac{\pi}{2}$$

5.4.53

We complete the derivation by noting that equation 5.4.52 can be identically expressed as Identity 5.4.39.

5.4.5 Reconstructing the Relative α_L Path Using the Identity $^2\Delta\alpha_P = {}^2\Delta\alpha_L$

We again consider the probe at two angular states *n* and *n+m* (see equations 5.4.34-5.4.35) in the case where the condition for β_P given in equation 5.4.36 is satisfied. We are therefore able to use Identity 5.4.39, which equates $^m\Delta\alpha_P$ with $^m\Delta\alpha_L$ when *m* is even. For the case when *m* = 2, we arrive at:

$$^2\Delta\alpha_{P,n} = {}^2\Delta\alpha_{L,n}$$

5.4.54

Using equation 5.4.42, this is then expressed as:

$$\Delta\alpha_{P,n} + \Delta\alpha_{P,n+1} = \Delta\alpha_{L,n} + \Delta\alpha_{L,n+1}$$

5.4.55

which is re-arranged to give the definition for R, which is constant over all n = 0, 1,…,n,…N-1:

$$\Delta\alpha_{P,0} - \Delta\alpha_{L,0} = \Delta\alpha_{P,1} - \Delta\alpha_{L,1} = \cdots = \Delta\alpha_{P,n} - \Delta\alpha_{L,n} = \cdots = \Delta\alpha_{L,N-1} - \Delta\alpha_{P,N-1} \equiv R$$

5.4.56

This allows us to express $\Delta\alpha_P$ as the sum of $\Delta\alpha_L$ and *R*:

$$\Delta\alpha_{P,n} = (-1)^n \cdot R + \Delta\alpha_{L,n}$$

5.4.57

where *R* is constant over all *n*. Therefore, calculating $\Delta\alpha_L$ from $\Delta\alpha_P$ depends on finding a reliable value for *R*. We start by taking the average of our measured values of $\Delta\alpha_P$'s over all *n*:

$$\overline{\Delta\alpha_P} = \frac{1}{N-1} \cdot \left(\sum_{n=0}^{N-1} (-1)^n \cdot \Delta\alpha_{P,n} \right)$$

5.4.58

Using Identity 5.4.57, this is then expressed as:

$$\overline{\Delta\alpha_P} = \frac{1}{N-1} \cdot \left(\sum_n \left(R + (-1)^n \cdot \Delta\alpha_{L,n} \right) \right) = R + \frac{1}{N-1} \cdot \left(\sum_n \left((-1)^n \cdot \Delta\alpha_{L,n} \right) \right)$$

5.4.59

We find then that:

$$\overline{\Delta\alpha_P} = R$$

5.4.60

is true for all values of *n* and *m* when:

$$\Delta\alpha_{L,n} = \Delta\alpha_{L,n+m}$$

5.4.61

and the maximum value for n = N – 1 is even, where N is the total number of angular states.

We then extend this to the general case in which equation 5.4.61 does not hold. Because of this, the mean of these $\Delta\alpha_P$'s does not necessarily equate to R as in the simple case detailed above. If we assume for a given run of myoV that equation 5.4.61 is true for a *some* of the $\Delta\alpha_{L,n}$'s, then we can calculate R by taking a weighted average of all of the $\Delta\alpha_{P,n}$'s. A weighted average allows us to exclude values of $\Delta\alpha_{P,n}$'s that significantly deviate from the average $\Delta\alpha_P$. Our weighting function, W, is defined by:

$$W_n = \frac{1}{\left(\left| \Delta\alpha_{P,n} - \overline{\Delta\alpha_P} \right| + \epsilon \right)^r}$$

5.4.62

where $\Delta\alpha_{P,n}$ is defined in equation 5.4.57, $\overline{\Delta\alpha_P}$ is the unweighted average; and ϵ and r are user-defined values where ϵ is chosen near zero to prevent division by 0, and r is any even value greater than 0. The weighting function is then applied by combining equation 5.4.58 with equation 5.4.62 to give:

$$\overline{\Delta\alpha_P}_{weighted} = \frac{1}{N-1} \cdot \left(\sum_{n=0}^{N-1} (-1)^n \cdot W_n \cdot \Delta\alpha_{P,n} \right)$$

5.4.63

Since the weighting function excludes values of $\Delta\alpha_{P,n}$ that significantly deviate from the mean $\overline{\Delta\alpha_P}$, and hence values of $\Delta\alpha_{L,n}$ that are significantly different from the mean $\overline{\Delta\alpha_L}$, then equation 5.4.61 is largely satisfied, therefore:

$$\overline{\Delta\alpha_P}_{weighted} \cong R$$

5.4.64

Equation 5.4.63 therefore allows us to calculate a reasonable value for R even in the more general case where equation 5.4.61 does not hold for all n, as long as there are a significant number of $\Delta\alpha_{L,n}$'s for which it is true.

5.4.6 Rationale for the Routine that Calculates the Orientation of the Probe Relative to the Lever-arm (θ_P, φ_P) for Individual Processive Runs

We again consider the probe at two angular states *n* and *n+m* (see equations 5.4.34 - 5.4.35) in the case where the condition for β_P given in equation 5.4.36 is satisfied. Solutions for α_L and β_L are defined over all θ_P - φ_P space as:

$$\alpha_{L,n} = \alpha_L(\theta_P, \varphi_P, \alpha_{P,n}, \beta_{P,n})$$

5.4.65

$$\beta_{L,n} = \beta_L(\theta_P, \varphi_P, \beta_{P,n})$$

5.4.66

We first consider the general case where:

$$\alpha_{L,n} - \alpha_{L,n+m} = \Delta\alpha_{L,n}$$

5.4.67

$$\alpha_L(\theta_P, \varphi_P, \alpha_{P,n}, \beta_{P,n}) - \alpha_L(\theta_P, \varphi_P, \alpha_{P,n+m}, \beta_{P,n+m}) = \Delta\alpha_{L,n}$$

5.4.68

$$\beta_{L,n} + \beta_{L,n+m} = \Sigma\beta_{L,n}$$

5.4.69

$$\beta_L(\theta_P, \varphi_P, \beta_{P,n}) + \beta_L(\theta_P, \varphi_P, \beta_{P,n+m}) = \Sigma\beta_{L,n}$$

5.4.70

where *m* is non-zero and odd.

We then look at the specific case where $m = 1$, $\Sigma\beta_L = \pi$ and $\Delta\alpha_L = 0$:

$$\alpha_L(\theta_P, \varphi_P, \alpha_{P,n}, \beta_{P,n}) - \alpha_L(\theta_P, \varphi_P, \alpha_{P,n+1}, \beta_{P,n+1}) = 0$$

5.4.71

$$\beta_L(\theta_P, \varphi_P, \beta_{P,n}) + \beta_L(\theta_P, \varphi_P, \beta_{P,n+1}) = \pi$$

5.4.72

Equations 5.4.71 and 5.4.72 represent a system of two equations that share the six parameters θ_P, φ_P, $\beta_{P,n}$, $\beta_{P,n+1}$, α_{Pn}, and α_{Pn+1}. Given our measured values for $\beta_{P,n}$, $\beta_{P,n+1}$, α_{Pn}, and α_{Pn+1}, the values for the parameters θ_P and φ_P can be solved exactly, assuming a real solution exists.

Since the conditions for Identity 5.4.57 to be true also must be fulfilled for calculating θ_P and φ_P, we can also substitute $\Delta\alpha_{Ln}$ with the values estimated using Identity 5.4.57.

Because we do not have any way to directly estimate $\Sigma\beta_{Ln}$, for this modified general case we make the assumption that $\Sigma\beta_{Ln} = 180°$. This is assuming that the trailing and lever arms are both rigid with respect to the actin filament, so their respective beta angles must add up to 180°. This expression is already represented in equation 5.4.72.

6 References

1. Wells AL, Lin AW, Chen LQ, et al. Myosin VI is an Actin-Based Motor that Moves Backwards. *Nature*. 1999;401:505-508.

2. Berg JS, Powell BC, Cheyney RE. A Millenial Myosin Census. *Molecular Biology Cell*. 2001;12:780-794.

3. Gillespie PG, Wagner MC, Hudspeth AJ. Identification of a 120 KDa Hair-Bundle Myosin Located Near Stereociliary Tips. *Neuron*. 1993;11:581-594.

4. Holt JR, Gillespie SK, Provance DW, et al. A chemical-genetic strategy implicates myosin-1c in adaptation by hair cells. *Cell*. 2002;108:371-381.

5. Batters C, Arthur CP, Lin A, et al. Myo1c is designed for the adaptation response in the inner ear. *Embo Journal*. 2004;23:1433-1440.

6. Garcia JA, Yee AG, Gillespie PG, Corey DP. Localization of myosin-I beta near both ends of tip links in frog saccular hair cells. *Journal Neuroscience*. 1998;18:8637-8647.

7. Bose A, Guilherme A, Robida SL, et al. Glucose Transporter Recycling in Response to Insulin is Facilitated by Myosin Myo1c. *Nature*. 2002;420:821-824.

8. Wu X, Bowers B, Rao K, Wei Q, Hammer JA3. Visualization of melanosome dynamics within wild-type and dilute melanocytes suggests a paradigm for myosin V function in vivo.

9. Gross SP, Tuma MC, Deacon SW, Serpinskaya AS, Reilein AR, Gelfand VI. Interactions and regulation of molecular motors in Xenopus melanophores. *Journal of Cell Biology*. 2002;156:855-865.

10. Geeves MA, Holmes KC. Structural Mechanism of Muscle Contraction. *Annual Review Biochemistry*. 1999;68:687-728.

11. Sweeney HL, Houdusse A. Structural and Functional Insights into the Myosin Motor Mechanism. *Anuual Reviews in Biophysics*. 2010;39:539-557.

12. Hokanson DE, Ostap EM. Myo1c binds tightly and specifically to phosphatidylinositol 4,5-bisphosphate and inositol 1,4,5-trisphosphate. *Proceedings of th National Academy of Sciences*. 2006;103:3118-3123.

13. Lymn RW, Taylor EW. Mechanism of adenosine triphosphate hydrolysis by actomyosin. *Biochemsitry*. 1971;10:4617-4624.

14. Warshaw DM, Guilford WH, Freyzon Y, et al. The light chain binding domain of expressed smooth muscle heavy meromyosin acts as a mechanical lever. *Journal of Biological Chemistry*. 2000;275:37167-37172.

15. Uyeda TQ, Abramson PD, Spudich JA. The neck region of the myosin motor domain acts a lever arm to generate movement. *Proceedings of the National Academy of Sciences*. 1996;93:4459-4464.

16. De La Cruz EM, Ostap EM. Relating biochemistry and function in the myosin

superfamily. *Current Opinion Cell Biology*. 2004;16:61-67.

17. Cooke R. The mechanism of muscle contraction. *CRC Critical Review of Biochemistry*. 1986;21:53-118.

18. Batters C, Wallace MI, Coluccio LM, Molloy JE. A model of stereocilia adaptation based on single molecule mechanical studies of myosin I. *Philosophical transactions of the Royal Society B.* 2004;359:1895-1905.

19. Laakso JM, Lewis JH, Shuman H, Ostap EM. Myosin I can act as a molecular force sensor. *Science*. 2008;321(5885):133-136.

20. Ruppert C, Kroschewski R, Bahler M. Identification, characterization and cloning of myr 1, a mammalian myosin-I. *Journal of Cell Biology*. 1993;120:1393-1403.

21. Tang N, Ostap EM. Motor domain-dependent localization of myo1b (myr-1). *Current Biology*. 2001;11:1131-1135.

22. Bose A, Robida S, Furcinitti PS, et al. Uncoventional myosin Myo1c promotes membrane fusion in a regulated exocytic pathway. *Molecular Cell Biology*. 2004;24:5447-5458.

23. Tyska MJ, Mackey AT, Huang JD, Copeland NG, Jenkins NA, Mooseker MS. Myosin-1a is critical for normal brush border structure and composition. *Molecular Cell Biology*. 2005;16:2443-2457.

24. Speder P, Adam G, Noselli S. Type Id unconventional myosin controls left-right

asymmetry in Drosophila. *Nature*. 2006;440:803-807.

25. Hozumi S, Maeda R, Taniguchi K, et al. An unconventiional myosin in Drosophila reverses the default handedness in vesceral organs. *Nature*. 2006;440:798-802.

26. Laakso JM, Lewis JH, Shuman H, Ostap EM. Control of myosin-I force sensing by alternative splicing. *Proceedings of the National Academy of Sciences*. 2010;107(2):698-702.

27. Reck-Peterson SL, Provance DW, Mooseker MS, Mercer JA. Class V Myosins. *Biochimica Biophysica Acta*. 2000;1496(1):36-51.

28. Mehta AD, Rock RS, Rief M, Spudich JA, Mooseker MS, Cheyney RE. Myosin-V is a processive actin-based motor. *Nature*. 1999;400:590-593.

29. Sakamoto T, Amitani I, Yokota E, Ando T. Direct observation of processive movement by individual myosin V molecules. *Biochemical and Biophysical Research Communications*. 2000;272(2):586-590.

30. Walker ML, Burgess SA, Sellers JR, et al. Two-headed binding of a processive myosin to F-actin. *Nature*. 2000;405:804-807.

31. Veigel C, Wang F, Bartoo ML, Sellers JR, Molloy JE. The gated gait of the processive molecular motor, myosin V. *Nature Cell Biology*. 2002;4(1):59-65.

32. Yildiz A, Forkey JN, McKinney SA, Ha T, Goldman Y, Selvin PR. Myosin V walks hand-over-hand: single fluorophore imaging with 1.5-nm localization. *Science*.

2003;300(5628):2061-2065.

33. Forkey JN, Quinlan ME, Shaw MA, Corrie JE, Goldman YE. Three-dimensional structural dynamics of Myosin-V by single-molecule fluorscence polarization. *Nature*. 2003;422\:399-404.

34. Beausang JF, Schroeder HW3, Nelson PC, Goldman YE. Twirling of actin by myosins II and V observed via polarized TIRF in a modified gliding assay. *Biophysics Journal*. 2008;95:5820-5831.

35. Ali MY, Uemura S, Adachi K, Itoh H, Kinosita KJ, Ishiwata S. Myosin V is a left-handed motor on the right-handed actin helix. *Nature Structural Biology*. 2002;9:464-467.

36. Lewis JH, Lin T, Hokanson DE, Ostap EM. Temperature dependence of nucleotide association and kinetic characterization of myo1b. *Biochemistry*. 2006;45:11589-11597.

37. Ostap EM, Pollard TD. Biochemical kinetic characterization of the Acanthamoeba Myosin-I ATPase. *Journal of Cell Biology*. 1996;132:1053-1060.

38. Jontes JD, Milligan RA, Pollard TD, Ostap EM. Kinetic characterization of brush border myosin-I ATPase. *Proceedings of the National Academey of Sciences USA*. 1997;94:14332-14337.

39. El Mezgueldi M, Tang N, Rosenfeld SS, Ostap EM. The kinetic mechanism of

Myo1e (human myosin-Ic). *Journal of biological chemistry*. 2002;277:21514-21521.

40. Durrwang U, Fujita-Becker S, Erent M, et al. Dictyostelium myosin-IE is a fast molecular motor involved in phagocytosis. *Journal of Cell Science*. 2006;119:550-558.

41. Coluccio LM, Geeves MA. Transient kinetic analysis of the 130-kDa myosin I (MYR-1 gene product) from rat liver. A myosin I designed for maintenance of tension? *Journal of Biological Chemistry*. 1999;274:21575-21580.

42. Geeves MA, Perreault-Micale C, Coluccio LM. Kinetic analyses of a truncated mammalian myosin I suggest a novel isomerization event preceding nucleotide binding. *Journal of Biological Chemistry*. 2000;275:21624-21630.

43. Clark R, Ansari MA, Dash S, Geeves MA, Coluccio LM. Loop 1 of transducer region in mammalian class I myosin, Myo1b, modulates actin affinity, ATPase activity, and nucleotide access. *Journal of Biological Chemistry*. 2005;280:30935-30942.

44. Veigel C, Coluccio LM, Jontes JD, Sparrow JC, Milligan RA, Molloy JE. The motor protein myosin-I produces its working stroke in two steps. *Nature*. 1999;398:530-533.

45. Siemankowski RF, Wiseman MO, White HD. ADP dissociation from actomyosin subfragment 1 is sufficiently slow to limit the unloaded shortening velocity in vertebrate muscle. *Proceedings of the National Academy of Sciences, USA*.

1985;82(3):658-662.

46. Jontes JD, Wilson-Kubalek EM, Milligan RA. A 32 degree tail swing in brush border myosin I on ADP release. *Nature*. 1995;378:751-753.

47. Takagi Y, Homsher EE, Goldman YE, Shuman H. Force generation in single conventional actomyosin complexes under high dynamic load. *Biophysics Journal*. 2006;90:1295-1307.

48. Rayment I, Rypniewski WR, Schmidt-Base K, et al. Three-dimensional structure of myosin subfragment-1: a molecular motor. *Science*. 1993;261:50-58.

49. Purcell TJ, Morris C, Spudich JA, Sweeney HL. Role of the lever arm in the processive stepping of myosin V. *Proceedings of the National Academy of Science, USA*. 2002;99(22):14159-14164.

50. Sakamoto T, Yildez A, Selvin PR, Sellers JR. Step-size is determined by neck length in myosin V. *Biochemistry*. 2005;44:16203-16210.

51. Lin T, Tang N, Ostap EM. Biochemical and motile properties of Myo1b splice isoforms. *Journal of Biological Chemistry*. 2005;280:41562-41567.

52. Mooseker MS, Coleman TR. The 110-kD protein-calmodulin complex of the intestinal microvillus (brush border myosin I) is a mechanoenzyme. *Journal of Cell Biology*. 1989;108:2395-2400.

53. Conzelman KA, Mooseker MS. The 110-kD protein-calmodulin complex of the

intestinal microvillus is an actin-activated MgATPase. *Journal of Cell Biology*. 1987;105:313-324.

54. Collins K, Sellers JR, Matsudaira P. Calmodulin dissociation regulates brush border myosin I (110-kD-calmodulin) mechanochemical activity in vitro. *Journal of Cell Biology*. 1990;110:1137-1147.

55. Lu H, Krementsova EB, Trybus KM. Regulation of myosin V processivity by calcium at the single molecule level. *Journal of Biological Chemsitry*. 2006;42:1987-1994.

56. Hiratsuka T. New ribose-modified fluorescent analogs of adenine and guanine nucleotides available as substrates for various enzymes. *Biochimica Biophysica Acta*. 1983;742:496-508.

57. Spudich JA, Watt S. The regulation of rabbit skeletal muscle contraction. I.Biochemical studies of the interaction of the tropomyosin-troponin complex with actin and the proteolytic fragments of myosin. *Journal of Biological Chemistry*. 1971;246:4866-4871.

58. Pollard TD. Purification of a high molecular weight actin filament gelation protein from Acanthamoeba that shares antigenic determinants with verterbrate spectrins. *Journal of Cell Biology*. 1984;99:1970-1980.

59. Putkey JA, Slaughter GR, Means AR. Bacterial expression and characterization of proteins derived from the chicken calmodulin cDNA and a calmodulin processed

gene. *Journal Biological Chemistry*. 1985;260:4704-4712.

60. De La Cruz EM, Wells AL, Rosenfeld SS, Ostap EM, Sweeney HL. The kinetic mechanism of Myosin V. *Proceedings of the National Academy of Sciences*. 1999;96:13726-13731.

61. De La Cruz EM, Ostap EM, Sweeney HL. Kinetic mechanism and regulation of myosin VI. *Journal of Biological Chemistry*. 2001;276:32373-32381.

62. Schatz PJ. Use of peptide libraries to map the substrate specificity of a peptid-modifying enzyme: a 13 residue consensus peptide specifies biotinylation in Escherichia coli. *Biotechnology*. 1993;11(10):1138-1143.

63. Kron SJ, Spudich JA. Fluorescent actin filaments move on myosin fixed to a glass surface. *Proceeding of the National Academy of Sciences USA*. 1986;83(17):6272-6276.

64. White HD, Belknap B, Webb MR. Kinetics of nucleoside triphosphate cleavage and phosphate release steps by associated rabbit skeletal actomyosin. *Biochemistry*. 1997;36:11828-11836.

65. Brune M, Hunter JL, Corrie JE, Webb MR. Direct, real-time measurement of rapid inorganic phosphate release using a novel fluorescent probe and its application to actomyosin subfragment 1 ATPase. *Biochemistry*. 1994;33:8262-8271.

66. Veigel C, Bartoo ML, White DC, Sparrow JC, Molloy JE. The stiffness of rabbit skeletal actomyosin cross-bridges determined with an optical tweezers transducer.

Biophysics Journal. 1998;75(3):1424-1438.

67. Press WH, Teukolsky SA, Vetterling WT, Flannery BR. *Numerical Recipes in C: The Art of Scientific Computing*. 3rd Edition ed. Cambridge: Cambridge University Press; 2007.

68. Ostap EM, Lin T, Rosenfeld SS, Tang N. Mechanism of regulation of Acanthamoeba myosin-Ic by heavy-chain phosphorylation. *Biochemistry*. 2002;41:12450-12456.

69. De La Cruz EM, Wells AL, Sweeney HL, Ostap EM. Actin and light chain isoform dependence of myosin V kinetics. *Biochemistry*. 2000;39:14196-14202.

70. Finer JT, Simmons RM, Spudich JA. Single myosin molecule mechanics: piconewton forces and nanometre steps. *Nature*. 1994;368:113-119.

71. Veigel C, Molloy JE, Schmitz S, Kendrick-Jones J. Load-dependent kinetics of force production by smooth muscle myosin measured with optical tweezers. *Nature Cell Biology*. 2003;5:980-986.

72. Veigel C, Schmitz S, Wang F, Sellers JR. Load-dependent kinetics of Myosin-V can explain its high processivity. *Nature Cell Biology*. 2005;7:1-9.

73. Hill AV. The combinations of haemoglobin with oxygen with carbon monoxide. *Journal Physiology*. 1910;40:iv-vii.

74. Millar NC, Geeves MA. The limiting rate of the ATP-mediated dissociation of actin

from rabbit skeletal muscle myosin subfragment 1. *FEBS Letters*. 1983;160:141-148.

75. Fujita-Becker S, Durrwang U, Erent M, Clark RJ, Geeves MA, Manstein DJ. Changes in Mg2+ ion concentration and heavy chain phosphorylation regulate the motor activity of a class I myosin. *Journal of Biological Chemistry*. 2005;280:6064-6071.

76. Robblee JP, Cao W, Henn A, Hannemann DE, De La Cruz EM. Thermodynamics of nucleotide binding to actomyosin V and VI: a positive heat capacity change accompanies strong ADP binding. *Biochemistry*. 2005;44:10238-10249.

77. Yengo CM, Chrin LR, Rovner AS, Berger CL. Tryptophan 512 is sensitive to conformational changes in the rigid relay loop of smooth muscle myosin during the MgATPase cycle. *Journal of Biological Chemistry*. 2000;275:25481-25487.

78. Malnasi-Csizmadia A, Woolley RJ, Bagshaw CR. Resolution of conformational states of Dictyostelium myosin II motor domain using tryptophan (W501) mutants: implication for the open-closed transition identified by crystallography. *Biochemistry*. 2000;39:16135-16146.

79. Yengo CM, Sweeney HL. Functional role of loop 2 in myosin V. *Biochemistry*. 2004;43:2605-2612.

80. Cremo CR, Geeves MA. Interaction of actin and ADP with the head domain of smooth muscle myosin: implication for strain-dependent ADP release in smooth

muscle. *Biochemistry*. 1998;37:1969-1978.

81. Altman D, Sweeney HL, Spudich JA. The mechanism of myosin VI translocation and its load-induced anchoring. *Cell*. 2004;116:737-749.

82. Zhu T, Beckingham K, Ikebe M. High affinity Ca2+ binding sites of calmodulin are critical for the regulation of myosin I-beta function. *The Journal of Biological Chemistry*. 1998;273:20481-20486.

83. Dominguez R, Freyzon Y, Trybus KM, Cohen C. Crystal structure of a vertebrate smooth muscle myosin motor domain and its complex with the essential light chain: visualization of the pre-power stroke state. *Cell*. 1998;94:559-571.

84. Adamek N, Coluccio LM, Geeves MA. Calcium sensitivity of the cross-bridge cycle of Myo1c, the adaptation motor in the inner ear. *Proceedings of the National Academy of Sciences*. 2008;105:5710-5715.

85. Clapham DE. Calcium Signaling. *Cell*. 2007;131:1047-1058.

86. Vivian JT, Callis PR. Mechanisms of tryptophan fluorescence shifts in proteins. *Biophysics Journal*. 2001;80:2093-2109.

87. Kodera N, Yamamoto D, Ishikawa R, Ando T. Video imaging of walking myosin V by high-speed atomic force microscopy. *Nature*. 2010;468:72-76.

88. Toprak E, Enderlein J, Syed S, et al. Defocused orientation and position imaging (DOPI) of myosin V. *Proceeding National Academy of Sciences USA*.

2006;103:6495-6499.

89. Corrie JE, Brandmeier BD, Ferguson RE, et al. Dynamic measurement of myosin light-chain-domain tilt and twist in muscle contraction. *Nature*. 1999;400:425-430.

90. Amos LA, Amos WB. *Molecules of the Cytoskeleton*: Guilford Press; 1991.

91. Syed S, Snyder GE, Franzini-Armstrong C, Selvin PR, Goldman YE. Adaptability of myosin V studied by simultaneous detection of position and orientation. *EMBO Journal*. 2006;25:1795-1803.

92. Pardee JD, Spudich JA. Purification of muscle actin. *Methods Cell Biology*. 1982;24:271-289.

93. Corrie JE, Craik JS. Synthesis and characterization of iodoacetamidotetramethylrhodamine. *Journal Chemical Society, Perkin Transactions*. 1994;1:2967-2973.

94. Corrie JE, Craik JS, Munasinghe VR. A homobifunctional rhodamine for labeling proteins with defined orientations of a fluorophore. *Bioconjugate Chemistry*. 1998;9:160-167.

95. Putkey JA, Slaughter GR, Means AR. Bacterial expression and characterization of proteins derived from the chicken calmodulin cDNA and a calmodulin processed gene. *Journal Biological Chemistry*. 1985;260:4704-4712.

96. Forkey JN, Quinlan ME, Goldman YE. Measurement of single macromolecule

orientation by total internal reflection fluorescent polarization microscopy. *Biophysics Journal*. 2005;89:1261-1271.

97. Beausang JF, Sun Y, Quinlan ME, Forkey JN, Goldman YE. Single molecule fluorescence polarization via polarized total internal reflection fluorescent microscopy. In: Selvin PR, H T, eds. *Laboratory Manual for Single Molecule Studies*. Cold Spring Harbor: Cold Spring Harbor Laboratory Press; 2007.

98. Coureaux PD, Sweeney HL, Houdusse A. Three myosin V structures delineate essential features of chemo-mechanical transduction. *EMBO Journal*. 2004;23(23):4527-4537.

99. Houdusse A, Gaucher JF, Krementsova E, Mui S, Trybus KM, Cohen C. Crystal structure of apo-calmodulin bound to the first two IQ motifs of myosin V reveals essential recognition features. *Proceedings of the National Academey of Sciences, USA*. 2006;103(51):19326-19331.

100. Parker D, Bryant Z, Delp SL. Coarse-grained structural modeling of molecular motors using multibody dynamics. *Cell Molecular Bioengineering*. 2010;2(3):366-374.

101. Terrak M, Rebowski G, Lu RC, Grabarek Z, Dominguez R. Structure of the lightchain-binding domain of myosin V. *Proceedings of the National Academy of Sciences, USA*. 2005;102(36).

102. Forkey JN, Quinlan ME, Goldman YE. Protein structural dynamics by single-

molecule fluorescence polarization. *Progress in Biophysics and Molecular Biology*. 2000;74:1-35.

103. Cheyney RE, O'Shea MK, Heuser JE, et al. Brain myosin-V is a two-headed uncoventional myosin with motor activity. *Cell*. 1993;75:13-23.

104. Sun Y, Schroeder HW, Beausang JF, Homma K, Ikebe M, Goldman YE. Myosin VI walks "wiggly" on actin with large and variable tilting. *Molecular Cell*. 2007;28(6):954-964.

105. Komori T, Nishikawa S, Ariga T, Iwane AH, Yanagida T. Simultaneous measurement of nucleotide occupancy and mechanical displacement in myosin-V, a processive molecular motor. *Biophysics Journal*. 2009;96:L04-L06.

106. Bevington PR, Robinsion DK. *Data Reduction and Error Analysis for the Physical Sciences*. 3rd Edition ed: McGraw Hill; 2003.

107. Bell GI. Models for the specific adhesion of cells to cells. *Science*. 1978;200:618-627.

108. Howard J. *Mechanics of Motor Proteins and the Cytoskeleton*. Sunderland: Sinauer Associates, Inc.; 2001.